

EFFECT OF CILIA MOVEMENT TO MUCUS FLOW IN HUMAN  
LUNGS IN TWO DIMENSIONS



A THESIS SUBMITTED IN PARTIAL FULFILLMENT OF THE REQUIREMENT  
FOR THE DEGREE OF DOCTOR OF PHILOSOPHY IN APPLIED MATHEMATICS  
DEPARTMENT OF MATHEMATICS SCHOOL OF SCIENCE  
KING MONGKUT'S INSTITUTE OF TECHNOLOGY LADKRABANG  
2025

This material is reserved for educational use only. Not to be used for commercial use.  
KMITL-2025-SC-D-001-017

Forbidden to modify the content, and cite the document when use.



COPYRIGHT 2025

SCHOOL OF SCIENCE

THE KING MONGKUT'S INSTITUTE OF TECHNOLOGY LADKRABANG commercial use.

Forbidden to modify the content, and cite the document when use.

<b>Thesis Title</b>	Effect of Cilia Movement to Mucus Flow in Human Lungs in Two Dimensions
<b>Student Name</b>	Mr. Surachai Phaenchat
<b>Student ID</b>	62605007
<b>Degree</b>	Doctor of Philosophy (Applied Mathematics)
<b>Department</b>	Mathematics
<b>Year</b>	2025
<b>Thesis Advisor</b>	Assoc.Prof.Dr. Nachayadar Kamolmitisom

### Abstract

Mucociliary clearance (MCC) is a protective process in the human respiratory system that expels inhaled foreign particles such as dust, dirt, and smoke out of the body. When a human inhales strange particles along with air, they are trapped by mucus in the respiratory tract. This mucus is secreted by goblet cells within the epithelial cells. After catching, the mucus forms a mucus layer (ML) and lies above the periciliary layer (PCL). The PCL resides above the epithelial cells and consists of Newtonian fluid known as PCL fluid and hair-like structures known as cilia. Once the mucus traps the particles. Cilia in the PCL move forward and backward to remove the mucus out of the human body. In this work, we apply the two-dimensional nonlinear Brinkman and steady-state Navier-Stokes equations to determine the velocity of the PCL fluid when the cilia make angles with the horizontal plane. Next, we use the two-dimensional Stokes equation to calculate the velocity of the mucus when cilia make various angles with the horizontal plane. The numerical results are approximated using a mixed finite element method. The Newton's method is employed to calculate the nonlinear term. Furthermore, the models developed in this study can be applied to similar problems in other biological systems and engineering applications, such as the study of fluid flow in porous media or biofluid dynamics.

**Keywords :** Cilia, Mixed finite element method, Nonlinear Brinkman equations, Steady-state Navier-Stokes equations, Stokes equation, Periciliary layer.

## Acknowledgements

I am profoundly grateful to my advisor, Assoc.Prof.Dr. Nachayadar Kamolmitisom, for her support, suggestions, imparting a wealth of knowledge and providing me with the skills necessary to conduct research and write this thesis. Although she shared extensive knowledge, she also encouraged me to face real-life problems and learn how to solve them. Her expertise and encouragement have been pivotal in the completion of this work.

I would like to extend my heartfelt appreciation to the chairperson, Asst. Prof. Dr. Jiraphan Suntornchost from Chulalongkorn University, and my committee members: Asst. Prof. Dr. Sukrawan Mavecha, Asst. Prof. Dr. Puttha Sakkaplangkul, and Asst. Prof. Dr. Nattaporn Chuenjarern. Their valuable suggestions and thoughtful feedback have significantly improved the quality of my thesis.

Special thanks to my family and friends for their support, attentive listening, understanding, and encouragement. Their constant presences have helped me throughout my studies. This accomplishment would not have been possible without them.

Surachai Phaenchat



# Table of Contents

	Page
Abstract .....	i
Acknowledgements .....	ii
Table of Contents .....	iii
List of Tables.....	v
List of Figures.....	vi
<b>Chapter 1. Introduction</b> .....	<b>1</b>
1.1 Research Motivation .....	1
1.2 Objectives of the Study.....	4
1.3 Scope of the Study.....	4
1.4 Benefits of the Study.....	4
1.5 Research Methodology.....	5
<b>Chapter 2. Basic Knowledge and Literature Review</b> .....	<b>6</b>
2.1 Hybrid Mixture Theory (HMT).....	6
2.2 Nonlinear Brinkman Equation.....	7
2.3 Steady-State Navier-Stokes Equation .....	8
2.4 Derivation of Stokes Equation.....	8
2.5 Finite Element Method.....	10
2.6 Newton's Method.....	16
2.6.1 One-Dimensional Newton's Method.....	16
2.6.2 $N$ -Dimensional Newton's Method.....	18
2.7 Permeability.....	20
2.8 Porosity.....	21
2.9 Literature Review .....	22
<b>Chapter 3. Mathematical Models</b> .....	<b>24</b>
3.1 Model Discretization.....	24
3.1.1 The Nonlinear Brinkman Equation.....	24
3.1.2 The Steady-State Navier-Stokes Equation .....	29
3.1.3 The Stokes Equation.....	31
3.2 Boundary Conditions .....	33
3.2.1 Boundary Condition for the PCL.....	33
3.2.2 Boundary Condition for the Free-Fluid Region and the Mu- cus Layer .....	36
<b>Chapter 4. Numerical Results</b> .....	<b>40</b>
4.1 Exact Solution .....	40
4.2 Validation of Numerical Results .....	41

This material is reserved for educational use only, not allowed for commercial use.

Forbidden to modify the content, and cite the document when use.

4.3 Numerical Solutions.....	42
4.3.1 The Numerical Solutions of the Nonlinear Brinkman and the Steady-State Navier-Stokes Equations.....	43
4.3.2 The Numerical Solutions of the Stokes Equation .....	51
<b>Chapter 5. Conclusions.....</b>	<b>60</b>
Appendices.....	66
Appendix A .....	67
Appendix B.....	79
Author Biography.....	96



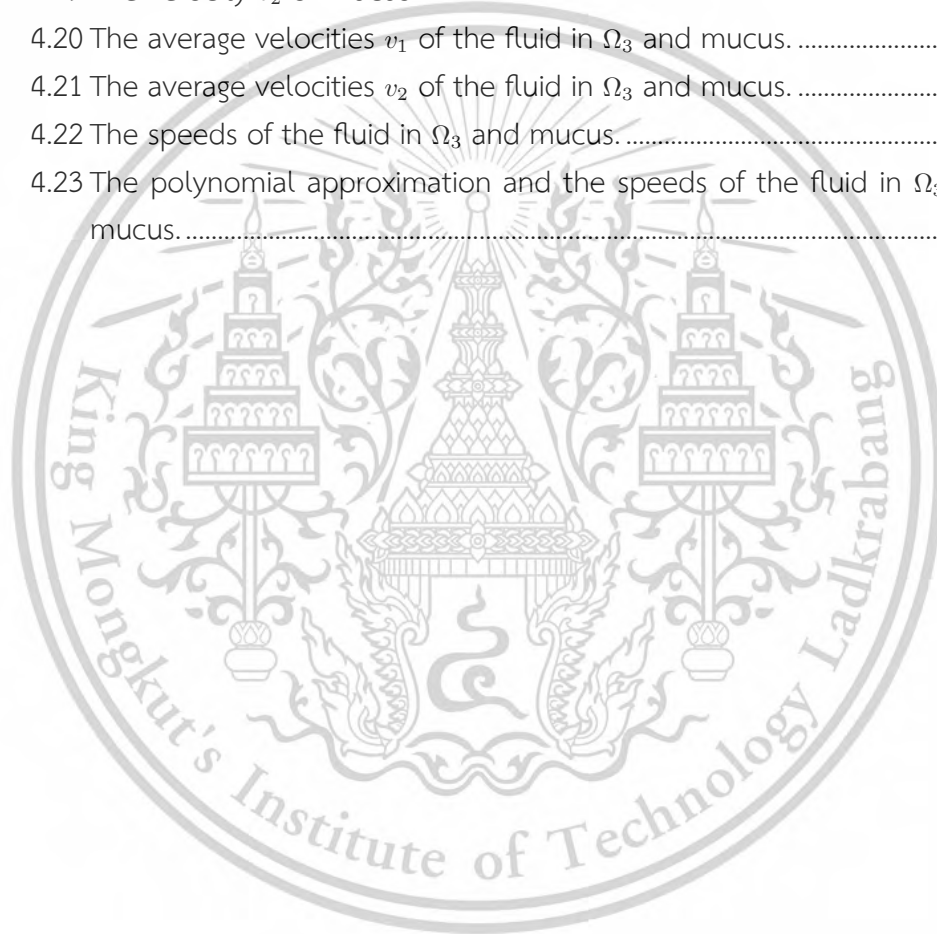
## List of Tables

Table	Page
1.1 The research schedule.....	5
2.1 Characteristic parameters.....	9
2.2 Iterative results of the one-dimensional nonlinear equation (2.66).....	18
2.3 Iterative results of the two-dimensional nonlinear system of equations (2.85). .....	20
4.1 The eighth-order polynomial functions: $a_1\lambda^8 + a_2\lambda^7 + a_3\lambda^6 + a_4\lambda^5 + a_5\lambda^4 + a_6\lambda^3 + a_7\lambda^2 + a_8\lambda$ is used to approximate the speed along a cilium for the angles $\theta = 90^\circ$ to $50^\circ$ . .....	43
4.2 The inverse of the permeability tensor $\mathbf{k}^{-1}$ for the angles $\theta = 50^\circ$ to $90^\circ$ ...	44
4.3 The number of iterations of Newton's method, computation time and number of degrees of freedom for each angle.....	46
4.4 The fifteenth-order polynomial functions: $p(h_p) = \varphi_{15}h_p^{15} + \varphi_{14}h_p^{14} + \varphi_{13}h_p^{13} + \varphi_{12}h_p^{12} + \varphi_{11}h_p^{11} + \varphi_{10}h_p^{10} + \varphi_9h_p^9 + \varphi_8h_p^8 + \varphi_7h_p^7 + \varphi_6h_p^6 + \varphi_5h_p^5 + \varphi_4h_p^4 + \varphi_3h_p^3 + \varphi_2h_p^2 + \varphi_1h_p + \varphi_0$ for the average speed of the PCL fluid for all angles. ....	51
4.5 The ninth-order polynomial functions: $p(h) = b_9h^9 + b_8h^8 + b_7h^7 + b_6h^6 + b_5h^5 + b_4h^4 + b_3h^3 + b_2h^2 + b_1h + b_0$ for the speeds of the fluid in $\Omega_3$ and mucus. ....	58

## List of Figures

Figure	Page
1.1 (a) Human respiratory system. (b) a cross-section of the trachea. ....	1
1.2 A portion of the cross-section of the trachea. ....	2
1.3 The cartoon picture of the PCL domain: (a) the cilia are perpendicular to the horizontal plane. (b) the cilia make an angle $\theta$ with the horizontal plane. ....	2
1.4 The cartoon picture of the PCL and the ML. ....	3
2.1 Linear triangular element. ....	11
2.2 The triangular coordinate system: (a) the physical coordinate system (b) the natural coordinate system. ....	12
2.3 (a) Three-node triangular element in the natural coordinate (b) Six-node triangular element in the natural coordinate. ....	13
2.4 The domain of fluid flow through the solid phase (a) rock and (b) sand. ....	21
2.5 The porosity. ....	21
3.1 Numerical domains and boundaries of the problem. (a) The cilia are perpendicular to the horizontal plane. (b) The cilia make angle $\theta$ less than $90^\circ$ to the horizontal plane. ....	33
3.2 Numerical domains and boundaries of the domains $\Omega_3$ and $\Omega_4$ . ....	37
4.1 The average velocity $v_1$ profile of two-dimensional numerical solution for 7, 17, 31 and 61 nodes and the exact solution when $\theta = 90^\circ$ along $x_2$ -axis. ....	42
4.2 The cilia speed for the angle $50^\circ, 60^\circ, 70^\circ, 80^\circ$ and $90^\circ$ . ....	44
4.3 The porosity for the angles $50^\circ, 60^\circ, 70^\circ, 80^\circ$ and $90^\circ$ . ....	45
4.4 The generated mesh of the PCL domain for various angles by using the open-source software Netgen [31]. ....	46
4.5 The velocity of the PCL fluid $v_1$ in $x_1$ -direction when the angles $\theta = 50^\circ, 60^\circ, 70^\circ, 80^\circ$ , and $90^\circ$ . ....	47
4.6 The velocity of the PCL fluid $v_2$ in $x_2$ -direction when the angles $\theta = 50^\circ, 60^\circ, 70^\circ, 80^\circ$ , and $90^\circ$ . ....	47
4.7 The average velocity $v_1$ of the PCL fluid for 5 different angles. ....	48
4.8 The average velocity $v_2$ of the PCL fluid for 5 different angles. ....	48
4.9 The speeds of the PCL fluid for 5 different angles. ....	49
4.10 Comparison between the speeds of the PCL fluid and cilia for each angle. ....	49
4.11 The average speed for all angles. ....	50
4.12 The polynomial approximation and the average speed of the PCL fluid. ....	50

4.13 The velocities $v_1$ of the PCL fluid at the tips of cilia at the angles $\theta = 50^\circ, 60^\circ, 70^\circ, 80^\circ$ and $90^\circ$ .	52
4.14 The velocities $v_2$ of the PCL fluid at the tips of cilia at the angles $\theta = 50^\circ, 60^\circ, 70^\circ, 80^\circ$ and $90^\circ$ .	53
4.15 Generated mesh for the free-fluid and ML domains using the open-source software Netgen software [31].	53
4.16 The velocity $v_1$ of the fluid in $\Omega_3$	54
4.17 The velocity $v_2$ of the fluid in $\Omega_3$	55
4.18 The velocity $v_1$ of mucus.	55
4.19 The velocity $v_2$ of mucus.	56
4.20 The average velocities $v_1$ of the fluid in $\Omega_3$ and mucus.	56
4.21 The average velocities $v_2$ of the fluid in $\Omega_3$ and mucus.	57
4.22 The speeds of the fluid in $\Omega_3$ and mucus.	58
4.23 The polynomial approximation and the speeds of the fluid in $\Omega_3$ and mucus.	59



# Chapter 1

## Introduction

In this chapter, we provide the research motivation, research methodology, objectives and benefits of the study.

### 1.1 Research Motivation

Respiratory diseases are one of our health problems that affect the lungs and airways, including chronic obstructive pulmonary disease (COPD), asthma, lung cancer, and other illnesses. Some of these diseases arise from breathing in polluted air, such as environmental contaminants, airborne toxins, and smoke, triggering the respiratory system to produce excess mucus. Figure 1.1(a) shows the respiratory system, which consists of mouth, nasal cavity, nose, pharynx, larynx, trachea, bronchus, and lungs. Figure 1.1(b) illustrates a cross-section of the trachea, which consists of two portions: the anterior and posterior. The anterior portion contains the trachealis muscle, mucosa, cilia, and hyaline cartilage, while the posterior portion consists of the esophagus.

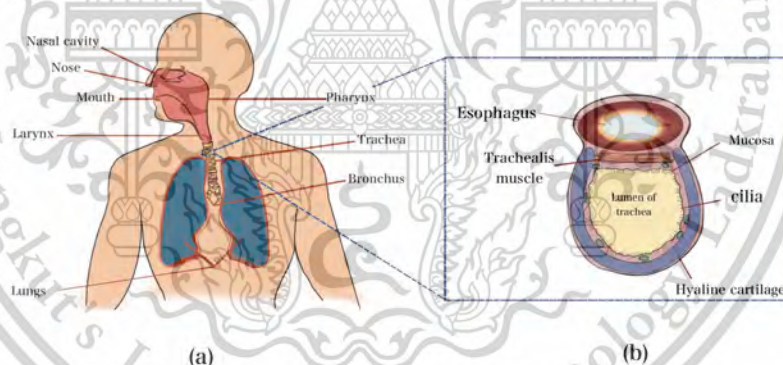
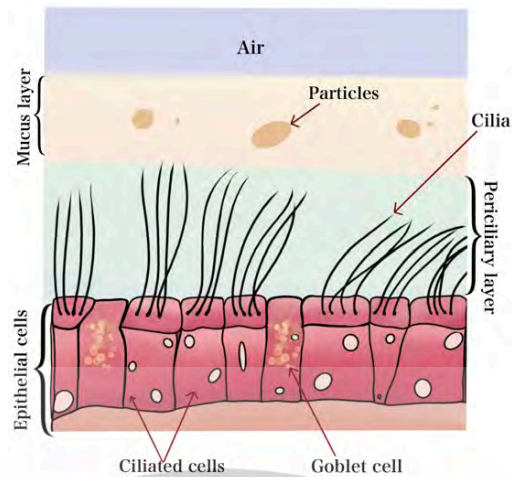


Figure 1.1: (a) Human respiratory system. (b) a cross-section of the trachea.

Figure 1.2 shows a portion of the cross-section of the trachea in the human respiratory system, which consists of the air, inhaling particles, the mucus layer (ML), the periciliary layer (PCL), the cilia, ciliated cells, goblet cells, and epithelial cells. The PCL consists of two phases, the liquid phase, Newtonian fluid, and the solid phase, known as cilia. When humans inhale strange particles into their bodies, the goblet cells scattering in the epithelial cells secrete mucus to trap those strange particles and form a mucus layer (ML) on the top of PCL. The cilia in the PCL beneath the ML beat forward and backward to move mucus out of the human body. This mechanism is called mucociliary clearance (MCC), which is the immunity protection of the body.

This material is reserved for educational use only, not allowed for commercial use.

Forbidden to modify the content, and cite the document when use.



**Figure 1.2:** A portion of the cross-section of the trachea.

In this work, we focus on the fluid flow in the PCL and the ML. The fluid flow in both layers is affected by the movement of the cilia in the PCL. Figure 1.3(a) shows the cartoon picture of the cilia in the PCL perpendicular to the horizontal plane. Figure 1.3(b) illustrates cilia making the angle  $\theta < 90^\circ$  to the horizontal plane, where  $\theta$  represents the angle between the cilia and the horizontal plane. The movement of cilia has divided the PCL into two layers: one layer consisting of both solid and liquid phases, known as a porous medium, and another layer consisting of only the liquid phase, called a free-fluid region. We define the porous medium to be  $\Omega_1$  and the free-fluid region to be  $\Omega_2$ . In this work, we first find the velocity of the PCL fluid for the forward stroke of cilia, where  $40^\circ \leq \theta \leq 90^\circ$ . Because this study focuses on steady-state flow conditions, the equations used to find the velocity of the PCL fluid are the nonlinear Brinkman equations for the porous medium ( $\Omega_1$ ) and the steady-state Navier-Stokes equations for the free-fluid region ( $\Omega_2$ ). Since this work focuses on the behavior of a group of cilia rather than a single cilium, the equations employed are macroscale equations.

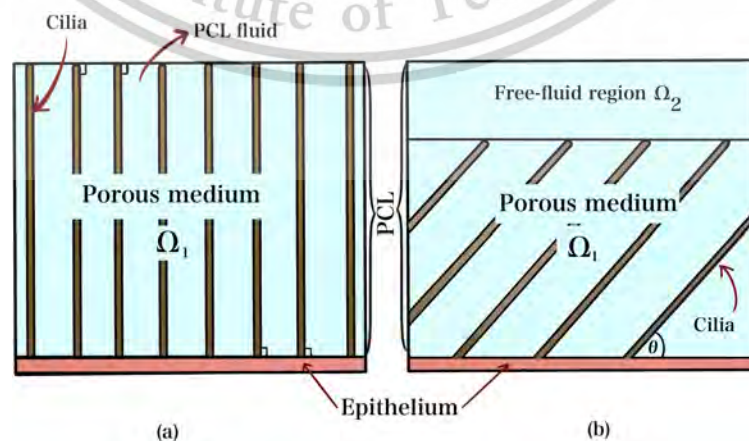


**Figure 1.3:** The cartoon picture of the PCL domain: (a) the cilia are perpendicular to the horizontal plane, (b) the cilia make an angle  $\theta$  with the horizontal plane.

This material is intended for educational use only, not allowed for commercial use.

Forbidden to modify the content, and cite the document when use.

Because the velocity of the fluid in the free-fluid region  $\Omega_2$  is obtained from a single angle per one fixed domain, next we find the velocity of the fluid in the free-fluid region when cilia make several angles to the horizontal plane for one fixed domain as shown in Figure 1.4. Figure 1.4 displays the ML and the PCL when cilia make angles with the horizontal plane for one fixed domain, where the porous medium is divided into equal intervals ranging from  $90^\circ$  to  $50^\circ$ . So, the permeability and porosity vary over the porous domain. Since the fluid in the free-fluid region in Figure 1.4 is affected by many angles that the cilia make with the horizontal plane, rather than a single angle, to find the velocity of fluids, we define the free-fluid region and the ML in Figure 1.4 to be  $\Omega_3$  and  $\Omega_4$ , respectively.

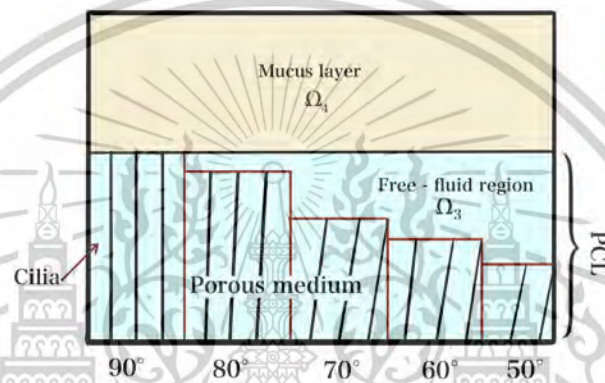


Figure 1.4: The cartoon picture of the PCL and the ML.

To find the velocities of the fluids in  $\Omega_3$  and  $\Omega_4$ , we use the velocity of the PCL fluid at the tips of cilia as the bottom boundary condition of the domain  $\Omega_3$ . The velocity of the fluid obtained at the top of  $\Omega_3$  is used as the boundary condition at the bottom of  $\Omega_4$  to determine the velocity of the mucus. For the fluid flow in  $\Omega_3$  and  $\Omega_4$ , we apply the Stokes equation to determine the velocities of the fluid in these domains. We calculate our work as follows.

First, we find the velocity of the fluids in  $\Omega_1$  and  $\Omega_2$  when cilia make only one angle  $\theta$  to the horizontal plane in one fixed domain as shown in Figure 1.3 by using the nonlinear Brinkman equations in  $\Omega_1$  and the steady-state Navier-Stokes equations in  $\Omega_2$  to determine the velocity of the PCL fluid.

Second, we find the velocities of the fluid in  $\Omega_3$  and the mucus in  $\Omega_4$  when cilia make several angles to the horizontal plane in one fixed domain as shown in Figure 1.4. For these domains, we apply the Stokes equation to find the fluid velocities.

The numerical solutions of this study are calculated by using a mixed finite element method and the Newton's method, presented in Chapter 4. These two models provide a more comprehensive understanding of the behavior of fluid flow in the PCL and the ML.

## 1.2 Objectives of the Study

- 1) To study the nonlinear Brinkman and the steady-state Navier-Stokes equations.
- 2) To study the Stokes equation.
- 3) To study a mixed finite element method and Newton's method.
- 4) To study the movement of the solid phase and its effect on the fluid phase.
- 5) To find the velocity of the PCL fluid when cilia make different angles to the horizontal plane.
- 6) To determine the velocity of the mucus affected by the movement of cilia during the forward stroke.
- 7) To extend and enhance the previous research conducted by applying a more physiologically realistic approach to a better model of the ML.

## 1.3 Scope of the Study

- 1) The forward stroke of a bundle of cilia is considered from the angle  $\theta = 90^\circ$  to  $40^\circ$ .
- 2) The cilia are assumed to stop beating at  $\theta = 40^\circ$ .
- 3) The maximum velocity of the cilia is assumed to occur at the tips of the cilia.
- 4) The interface between the porous medium and the free-fluid region is assumed to be continuous.
- 5) The density of the PCL fluid and mucus is assumed to be the same, while their viscosities are different.
- 6) This work is considered in a two-dimensional domain.

## 1.4 Benefits of the Study

- 1) This study provides valuable knowledge of fluid flow models in both porous media and free-fluid regions.
- 2) This study can apply to other research areas such as groundwater flow, the transport of oil through pipes, airflow through porous materials, nutrient transport in plant roots.
- 3) This study enhances the understanding of respiratory systems, particularly in the context of mucus transport.
- 4) The results from this study can aid physicians in developing more effective treatment strategies for patients about mucus in human lungs.

This material is reserved for educational use only, not allowed for commercial use.

Forbidden to modify the content, and cite the document when use.

## 1.5 Research Methodology

- 1) Study the researches about the human respiratory tracts, focusing on the PCL and the ML.
- 2) Study the nonlinear Brinkman, the Navier-Stokes, and the Stokes equations.
- 3) Study a mixed finite element method and Newton's method.
- 4) Solve the mathematical models by using a mixed finite element method and Newton's method.
- 5) Write programs to find the numerical solutions.
- 6) Verify the results and write a conclusion.
- 7) Write the thesis book.

Table 1.1: The research schedule

Activity	Time frame										
	2019	2020		2021		2022	2023		2024		2025
	Sep. - Dec.	Jan. - Jul.	Aug. - Dec.	Jan. - May	Jun. - Dec.	Jan. - Dec.	Jan. - May	Jun. - Dec.	Jan. - Feb.	Mar. - Dec.	Jan. - May
Step 1											
Step 2											
Step 3											
Step 4											
Step 5											
Step 6											
Step 7											

This material is reserved for educational use only, not allowed for commercial use.

Forbidden to modify the content, and cite the document when use.

## Chapter 2

### Basic Knowledge and Literature Review

In this chapter, we provide foundational knowledge of the methods and equations used in this work. We begin by introducing the Hybrid Mixture Theory (HMT), an averaging theorem that help to upscale equations from the microscale to the macroscale, discussed in Section 2.1. The nonlinear Brinkman and steady-state Navier-Stokes equations are presented in Sections 2.2 and 2.3, respectively. The derivation of Stokes equations is provided in Section 2.4. The finite element method (FEM) is drawn in Section 2.5. The method employed to handle the nonlinear terms, the Newton method, is presented in Section 2.6. The permeability and porosity used in this work are presented in Sections 2.7 and 2.8, respectively. Finally, Section 2.9 provides a literature review relevant to the methodologies and topics addressed in this work.

#### 2.1 Hybrid Mixture Theory (HMT)

In this section, we briefly provide the upscaling process of the Hybrid Mixture Theory (HMT) [3, 12] used to upscale the microscale equation to macroscale equation. The HMT employs the averaging theorem to derive the macroscopic equation via the intrinsic phase average, which is the mass average of microscopic quantity over a representative elementary volume (REV). To support the transition to macroscopic modeling, the indicator function is defined as follows

$$\gamma_{\alpha}(\mathbf{r}, t) = \begin{cases} 1 & \text{if } \mathbf{r} \in \delta V_{\alpha} \\ 0 & \text{if } \mathbf{r} \in \delta V_{\beta}, \beta \neq \alpha. \end{cases} \quad (2.1)$$

Here,  $\delta V_{\alpha}$  denotes the portion of  $\delta V$  within the  $\alpha$ -phase and  $\delta V_{\beta}$  refers to the portion of  $\delta V$  within the  $\beta$ -phase where  $\delta V$  is the representative elementary volume (REV). The REV is the smallest volume over which measurements or simulations can be performed to yield results that are statistically representative of the macroscopic properties of a system. The averaging theorem provides the interchanging between the partial derivatives and the integral as follows

$$\frac{1}{|\delta V|} \int_{\delta V} \frac{\partial f}{\partial t} \gamma_{\alpha} d\nu(\xi) = \frac{\partial}{\partial t} \left[ \frac{1}{|\delta V|} \int_{\delta V} f \gamma_{\alpha} d\nu(\xi) \right] - \sum_{\beta \neq \alpha} \frac{1}{|\delta V|} \int_{\delta A_{\alpha\beta}} f \mathbf{w}_{\alpha\beta} \cdot \mathbf{n}_{\alpha} da(\xi) \quad (2.2)$$

$$\frac{1}{|\delta V|} \int_{\delta V} \nabla_x f \gamma_{\alpha} d\nu(\xi) = \nabla_x \left[ \frac{1}{|\delta V|} \int_{\delta V} f \gamma_{\alpha} d\nu(\xi) \right] + \sum_{\beta \neq \alpha} \frac{1}{|\delta V|} \int_{\delta A_{\alpha\beta}} f \mathbf{n}_{\alpha} da(\xi), \quad (2.3)$$

where  $f$  is the quantities in the field equations, and  $\delta A_{\alpha\beta}$  is the portion of  $\alpha\beta$  interface within  $\delta V$ ,  $\mathbf{w}_{\alpha\beta}$  denotes the microscopic velocity of interface  $\alpha\beta$  and  $\mathbf{n}_{\alpha}$  is the outward

Forbidden to modify the content, and cite the document when use.

unit normal vector to  $\delta V_\alpha$ . For better understanding about the HMT and averaging theorem, we adopt an example from [43] provided below.

**Example :** Consider the conservation of mass at the microscale, expressed as

$$\frac{\partial \rho}{\partial t} + \nabla \cdot (\rho \mathbf{v}) = 0, \quad (2.4)$$

where  $\rho$  is the density,  $t$  is time, and  $\mathbf{v}$  is the velocity. We multiply Eq. (2.4) by  $\gamma_\alpha$ , integrate it over  $\delta V$  and divide by the total volume  $|\delta V|$ , we obtain

$$\frac{1}{|\delta V|} \int_{\delta V} \frac{\partial \rho}{\partial t} \gamma_\alpha dV + \frac{1}{|\delta V|} \int_{\delta V} \nabla \cdot (\rho \mathbf{v}) \gamma_\alpha dV = 0. \quad (2.5)$$

Applying the averaging theorem ((2.2) and (2.3)) to each term in Eq. (2.5) yields

$$\begin{aligned} & \frac{\partial}{\partial t} \left[ \frac{1}{|\delta V|} \int_{\delta V} \rho \gamma_\alpha dV \right] - \sum_{\beta \neq \alpha} \frac{1}{|\delta V|} \int_{\delta A_{\alpha\beta}} \rho \mathbf{w}_{\alpha\beta} \cdot \mathbf{n}_\alpha da + \nabla \cdot \left[ \frac{1}{|\delta V|} \int_{\delta V} \rho \mathbf{v} \gamma_\alpha dV \right] \\ & + \sum_{\beta \neq \alpha} \frac{1}{|\delta V|} \int_{\delta A_{\alpha\beta}} \rho \mathbf{v} \cdot \mathbf{n}_\alpha da = 0, \end{aligned} \quad (2.6)$$

where

$$\epsilon^\alpha = \frac{|\delta V_\alpha|}{|\delta V|} \quad \text{and} \quad \sum_\alpha \epsilon^\alpha = 1, \quad (2.7)$$

$$\rho^\alpha = \frac{1}{|\delta V_\alpha|} \int_{\delta V_\alpha} \rho \gamma_\alpha dV, \quad (2.8)$$

$$\mathbf{v}^\alpha = \frac{1}{\rho^\alpha |\delta V_\alpha|} \int_{\delta V_\alpha} \rho \mathbf{v} \gamma_\alpha dV, \quad (2.9)$$

$$\hat{e}_\beta^\alpha = \frac{1}{\rho^\alpha |\delta V_\alpha|} \int_{\delta A_{\alpha\beta}} [\rho (\mathbf{w}_{\alpha\beta} - \mathbf{v})] \cdot \mathbf{n}_\alpha da. \quad (2.10)$$

Here,  $\epsilon^\alpha$  is called the volume fraction of phase  $\alpha$ ,  $\rho^\alpha$  is the macroscale density,  $\mathbf{v}^\alpha$  is the velocity of phase  $\alpha$  and  $\hat{e}_\beta^\alpha$  is the rate of exchange of mass from phase  $\beta$  to phase  $\alpha$ . Then Eq. (2.6) becomes

$$\frac{\partial(\epsilon^\alpha \rho^\alpha)}{\partial t} + \nabla \cdot (\epsilon^\alpha \rho^\alpha \mathbf{v}^\alpha) = \sum_{\beta \neq \alpha} \epsilon^\alpha \rho^\alpha \hat{e}_\beta^\alpha, \quad (2.11)$$

which is the macroscale continuity equation.

## 2.2 Nonlinear Brinkman Equation

In this section, we present the nonlinear Brinkman equation, which describes the fluid flow in a porous medium. We start from the multiphase equation upscaled from the conservation of momentum [7]

$$\rho \frac{D^l \mathbf{v}^l}{Dt} + \nabla p - \frac{\mu}{k} \nabla \cdot (2\epsilon^l \mathbf{d}^l) - \rho \mathbf{g}^l = -\mu \epsilon^l \mathbf{k}^{-1} (\mathbf{v}^l - \mathbf{v}^s), \quad (2.12)$$

This material is reserved for educational use only, not allowed for commercial use.

Forbidden to modify the content, and cite the document when use.

where the variable  $\varepsilon^l$  is the porosity,  $p$  is the pressure,  $\mu$  is the viscosity,  $\mathbf{v}^l$  is the fluid velocity,  $\rho$  is the density,  $\mathbf{v}^s$  is the velocity of solid phase,  $\mathbf{g}^l$  is the gravity,  $\mathbf{d}^l$  is  $0.5(\nabla\mathbf{v}^l + (\nabla\mathbf{v}^l)^T)$  and the superscript  $T$  is transpose,  $\frac{D^l}{Dt} = \frac{\partial}{\partial t} + \mathbf{v}^l \cdot \nabla$  is the material time derivative and  $\mathbf{k}^{-1}$  is the inverse of permeability. Rearranging the Eq. (2.12), we obtain

$$\rho \left( \frac{\partial \mathbf{v}^l}{\partial t} + \mathbf{v}^l \cdot \nabla \mathbf{v}^l \right) + \mu \mathbf{k}^{-1} \cdot (\varepsilon^l \mathbf{v}^l - \varepsilon^l \mathbf{v}^s) + \nabla p - \frac{\mu}{\varepsilon^l} \nabla \cdot (2\varepsilon^l \mathbf{d}^l) = \rho \mathbf{g}^l. \quad (2.13)$$

In this work, we concentrate on the steady-state flow problem. Therefore, neglecting the time-dependent term, we obtain

$$\rho \mathbf{v}^l \cdot \nabla \mathbf{v}^l + \mu \mathbf{k}^{-1} \cdot (\varepsilon^l \mathbf{v}^l - \varepsilon^l \mathbf{v}^s) + \nabla p - \frac{\mu}{\varepsilon^l} \nabla \cdot (2\varepsilon^l \mathbf{d}^l) = \rho \mathbf{g}^l, \quad (2.14)$$

which is the nonlinear Brinkman equation.

## 2.3 Steady-State Navier-Stokes Equation

The Navier-Stokes equation is a fundamental mathematical model for fluid flow problem. It helps to understand how fluids behave in many situations, such as airflow and water flows. This equation is given by

$$\rho \left( \frac{\partial \mathbf{v}}{\partial t} + \mathbf{v} \cdot \nabla \mathbf{v} \right) = -\nabla p + \rho \mathbf{g} + \mu \Delta \mathbf{v}, \quad (2.15)$$

where  $\mathbf{v}$  is the velocity. In this study, we focus on steady-state problem, where we are interested in the fluid flow when enough time has passed so that the velocity  $\mathbf{v}$  no longer evolves in time. This means that the time-derivative term  $\frac{\partial \mathbf{v}}{\partial t}$  is not considered in this study. Then Eq. (2.15) becomes

$$\rho(\mathbf{v} \cdot \nabla \mathbf{v}) = -\nabla p + \rho \mathbf{g} + \mu \Delta \mathbf{v}. \quad (2.16)$$

The steady-state Navier-Stokes equation is widely used in fluid dynamics to model flow conditions. This simplified form is particularly useful for analyzing fluid flow in various applications, including engineering, environmental modeling, and aerodynamics.

## 2.4 Derivation of Stokes Equation

In this section, we derive the Stokes equation used to find the mucus velocity starting from the Navier-Stokes equation. The derivation involves nondimensionalizing the Navier-Stokes equation to demonstrate that certain terms can be neglected in order to find the solution. For incompressible flow, the Navier-Stokes equation is

$$\rho \left( \frac{\partial \mathbf{v}}{\partial t} + \mathbf{v} \cdot \nabla \mathbf{v} \right) = -\nabla p + \rho \mathbf{g} + \mu \Delta \mathbf{v}. \quad (2.17)$$

To normalize Eq. (2.17), we introduce appropriate scaling parameters, as detailed in Table 2.1.

Forbidden to modify the content, and cite the document when use.

**Table 2.1:** Characteristic parameters

Scaling Parameter	Description	Primary Dimensions
$L$	characteristic length	$[L]$
$f$	characteristic frequency	$[1/t]$
$v_0$	characteristic velocity	$[L/t]$
$p_0$	reference pressure	$[M/(Lt^2)]$
$g_0$	gravitational acceleration	$[L/t^2]$

Using these scaling parameters, we define the following dimensionless variables:

$$\begin{aligned}\tilde{\mathbf{v}} &= \frac{\mathbf{v}}{v_0}, \quad \tilde{\mathbf{g}} = \frac{\mathbf{g}}{g_0}, \quad \tilde{p} = \frac{p}{p_0}, \\ \tilde{\nabla} &= L\nabla, \quad \tilde{t} = ft, \quad \tilde{\Delta} = L^2\Delta.\end{aligned}\quad (2.18)$$

Substituting Eq. (2.18) into (2.17), we have

$$\rho f v_0 \left( \frac{\partial \tilde{\mathbf{v}}}{\partial \tilde{t}} \right) + \frac{\rho v_0^2}{L} (\tilde{\mathbf{v}} \cdot \tilde{\nabla} \tilde{\mathbf{v}}) = -\frac{p_0}{L} \tilde{\nabla} \tilde{p} + \rho g_0 \tilde{\mathbf{g}} + \frac{\mu v_0}{L^2} \tilde{\Delta} \tilde{\mathbf{v}}. \quad (2.19)$$

We multiply both sides of Eq. (2.19) by  $\frac{L^2}{\mu v_0}$ , yielding

$$\frac{\rho f L^2}{\mu} \left( \frac{\partial \tilde{\mathbf{v}}}{\partial \tilde{t}} \right) + \frac{\rho v_0 L}{\mu} (\tilde{\mathbf{v}} \cdot \tilde{\nabla} \tilde{\mathbf{v}}) = -\frac{p_0 L}{\mu v_0} \tilde{\nabla} \tilde{p} + \frac{\rho g_0 L^2}{\mu v_0} \tilde{\mathbf{g}} + \tilde{\Delta} \tilde{\mathbf{v}}. \quad (2.20)$$

For the slow flow problem, we choose the reference time  $t$  as the duration for the cilia beating in one cycle, and the characteristic length  $L$  corresponds to the height of the cilia. The variables  $\rho$  and  $\mu$  represent the density and dynamic viscosity of water at 40°, respectively, and the gravitational acceleration  $g_0$  is taken as the Earth's gravity. The values of these variables, expressed in SI units, are as follows:

$$\begin{aligned}t &\approx 1.029 \text{ s}, \quad L \approx 7 \times 10^{-6} \text{ m}, \quad \mu \approx 0.653 \times 10^{-3} \text{ kg}/(\text{m} \cdot \text{s}), \\ g_0 &= 9.81 \text{ m}/\text{s}^2, \quad p_0 = 10^{-1} \text{ kg}/(\text{m} \cdot \text{s}^2), \quad \rho \approx 992.2 \text{ kg}/\text{m}^3.\end{aligned}\quad (2.21)$$

The values of time  $t$  and length  $L$  are obtained from [13] and [4], respectively, while the values of  $\rho$  and  $\mu$  are taken from [36]. The characteristic speed at the tip of the cilia is calculated as

$$v_0 = \frac{L\theta}{t} = \frac{(7 \times 10^{-6})(\pi/4)}{1.029} \approx 5.34 \times 10^{-6} \text{ m}/\text{s}, \quad (2.22)$$

where  $\theta$  is the angle between the cilia and the horizontal plane. Using the values in Eqs. (2.21) - (2.22), we calculate the coefficients in Eq. (2.20) as follows

$$\begin{aligned}\frac{\rho f L^2}{\mu} &= 7.23 \times 10^{-5}, \\ \frac{\rho v_0 L}{\mu} &= 5.67 \times 10^{-5}, \\ \frac{p_0 L}{\mu v_0} &= 2.00 \times 10^2, \\ \frac{\rho g_0 L^2}{\mu v_0} &= 1.36 \times 10^2.\end{aligned}\quad (2.23)$$

This material is reserved for educational use only, not allowed for commercial use.

Forbidden to modify the content, and cite the document when use.

Based on the coefficient values from Eq. (2.23), the time-dependent and nonlinear terms can be neglected. As a result, Eq. (2.17) simplifies to

$$\nabla p - \rho \mathbf{g} = \mu \Delta \mathbf{v}, \quad (2.24)$$

which is called the Stokes equation.

## 2.5 Finite Element Method

We first show the weak formulation of an equation. The weak formulation is a mathematical technique commonly used to solve partial differential equations (PDEs), especially in finite element analysis. To illustrate the weak formulation, we consider the following example equation,

$$\frac{\partial^2 u}{\partial x^2} + \frac{\partial^2 u}{\partial y^2} = f(x, y), \text{ in } \Omega, \quad (2.25)$$

where  $\Omega$  is domain, the variable  $u$  is unknown and  $f$  is the source term. We multiply both sides of the Eq. (2.25) by a weight function  $w$  and integration over domain  $\Omega$ ,

$$\int_{\Omega} w \left( \frac{\partial^2 u}{\partial x^2} + \frac{\partial^2 u}{\partial y^2} \right) d\Omega = \int_{\Omega} w f(x, y) d\Omega. \quad (2.26)$$

To derive the weak formulation, we first present Green's first identity, which helps to transform the integral of a second-order derivative into an equation involving the first-order derivatives and boundary terms. That is

$$\int_{\Omega} \nabla w \cdot \nabla u d\Omega + \int_{\Omega} w \nabla^2 u d\Omega = \int_{\Gamma} w \nabla u \cdot \mathbf{n} d\Gamma, \quad (2.27)$$

where  $\mathbf{n}$  is unit normal vector, the symbol  $\nabla$  represents the gradient (the first-order derivative) and  $\Gamma$  is the boundary. Applying the Green's first identity (2.27) to Eq. (2.26), we have

$$- \int_{\Omega} \left( \frac{\partial w}{\partial x} \frac{\partial u}{\partial x} + \frac{\partial w}{\partial y} \frac{\partial u}{\partial y} \right) d\Omega = \int_{\Omega} w f(x, y) d\Omega - \int_{\Gamma} w \left( \frac{\partial u}{\partial x} n_x + \frac{\partial u}{\partial y} n_y \right) d\Gamma, \quad (2.28)$$

where  $\mathbf{n} = (n_x, n_y)$  for a two-dimensional domain. The Eq. (2.28) is called the weak formulation of Eq. (2.25).

We next present the triangular element used in the finite element method and also in this work. The triangular element is a fundamental shape function used in the finite element method. So we present two types of triangular elements: linear triangular elements and isoparametric triangular elements. We first introduce the linear triangular element, one of the types used for a two-dimensional domain. Figure 2.1 shows the linear triangular element, with three nodes in each element. Each node is associated with the coordinates  $(x_i, y_i), i = 1, 2, 3$ , and the nodal variable  $u_i, i = 1, 2, 3$ . The interpolation of the nodal variable within an element is given by

This material is reserved for educational use only, not allowed for commercial use.

$$u_i = a_1 + a_2 x_i + a_3 y_i, \quad (2.29)$$

Forbidden to modify the content, and cite the document when use.

or

$$u_i = \begin{bmatrix} 1 & x_i & y_i \end{bmatrix} \begin{Bmatrix} a_1 \\ a_2 \\ a_3 \end{Bmatrix}, \quad (2.30)$$

where  $a_j$  represents the coefficient that needs to be determined with  $j = 1, 2, 3$ .

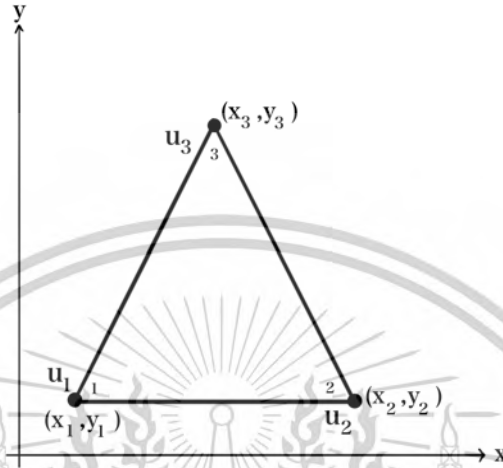


Figure 2.1: Linear triangular element.

For each node, the interpolation in Eq. (2.29) can be expressed in terms of the nodal variables. By substituting the  $x$  and  $y$  coordinates of each node into the equation, we obtain the following matrix form

$$\begin{Bmatrix} u_1 \\ u_2 \\ u_3 \end{Bmatrix} = \begin{bmatrix} 1 & x_1 & y_1 \\ 1 & x_2 & y_2 \\ 1 & x_3 & y_3 \end{bmatrix} \begin{Bmatrix} a_1 \\ a_2 \\ a_3 \end{Bmatrix}, \quad (2.31)$$

where  $x_i$  and  $y_i$  represent the coordinates of the  $i^{th}$  node and  $u_i$  is nodal variable. Inverting the  $3 \times 3$  matrix in Eq. (2.31), we have

$$\begin{Bmatrix} a_1 \\ a_2 \\ a_3 \end{Bmatrix} = \frac{1}{2A} \begin{bmatrix} x_2y_3 - x_3y_2 & x_3y_1 - x_1y_3 & x_1y_2 - x_2y_1 \\ y_2 - y_3 & y_3 - y_1 & y_1 - y_2 \\ x_3 - x_2 & x_1 - x_3 & x_2 - x_1 \end{bmatrix} \begin{Bmatrix} u_1 \\ u_2 \\ u_3 \end{Bmatrix}, \quad (2.32)$$

where

$$A = \frac{1}{2} \det \begin{pmatrix} 1 & x_1 & y_1 \\ 1 & x_2 & y_2 \\ 1 & x_3 & y_3 \end{pmatrix}. \quad (2.33)$$

Substituting Eq. (2.32) into (2.31) yields

$$u = \psi_1(x, y)u_1 + \psi_2(x, y)u_2 + \psi_3(x, y)u_3, \quad (2.34)$$

where  $\psi_i(x, y)$  is the shape function, which is the linear triangular element. The shape

This material is reserved for educational use only, not allowed for commercial use.

Forbidden to modify the content, and cite the document when use.

functions are defined as follows

$$\begin{aligned}\psi_1(x, y) &= \frac{(x_2y_3 - x_3y_2) + (y_2 - y_3)x + (x_3 - x_2)y}{2A}, \\ \psi_2(x, y) &= \frac{(x_3y_1 - x_1y_3) + (y_3 - y_1)x + (x_1 - x_3)y}{2A}, \\ \psi_3(x, y) &= \frac{(x_1y_2 - x_2y_1) + (y_1 - y_2)x + (x_2 - x_1)y}{2A}.\end{aligned}\quad (2.35)$$

The shape functions have the property that

$$\sum_{i=1}^3 \psi_i(x, y) = 1, \quad (2.36)$$

and the shape functions satisfy the property that the function  $\psi_i$  at the node  $(x_i, y_i)$ ,  $i = 1, 2, 3$ , is equal to 1, while the functions  $\psi_j$ ,  $j \neq i$  at the node  $(x_i, y_i)$ ,  $j = 1, 2, 3$ , are zero. That is

$$\begin{aligned}\psi_1(x_1, y_1) &= 1, & \psi_2(x_1, y_1) &= 0, & \psi_3(x_1, y_1) &= 0, \\ \psi_1(x_2, y_2) &= 0, & \psi_2(x_2, y_2) &= 1, & \psi_3(x_2, y_2) &= 0, \\ \psi_1(x_3, y_3) &= 0, & \psi_2(x_3, y_3) &= 0, & \psi_3(x_3, y_3) &= 1.\end{aligned}\quad (2.37)$$

Next, we introduce the isoparametric element. The concept of the isoparametric element is to use the mapping, which maps from one coordinate system into the other coordinate system. Figure 2.2 shows the coordinate system mapping three nodes from the physical coordinate to the natural coordinate systems and vice versa.

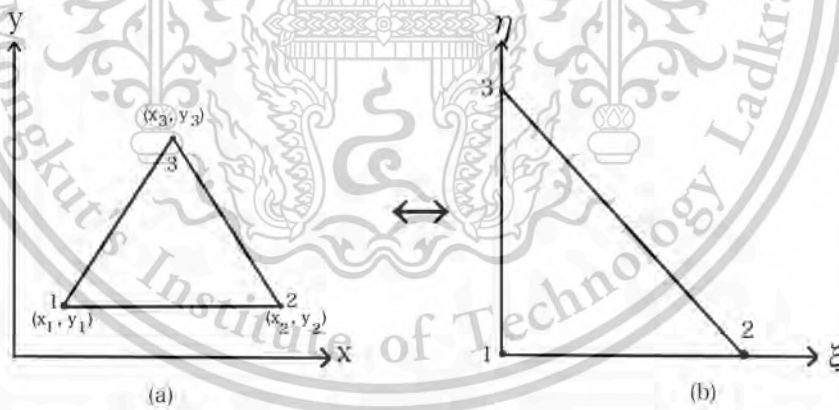


**Figure 2.2:** The triangular coordinate system: (a) the physical coordinate system (b) the natural coordinate system.

Figure 2.3 displays both the three-node and six-node configurations of the triangular isoparametric element in a natural coordinate system. The three-node triangular element is used for linear elements, while the six-node triangular element is used for quadratic elements.

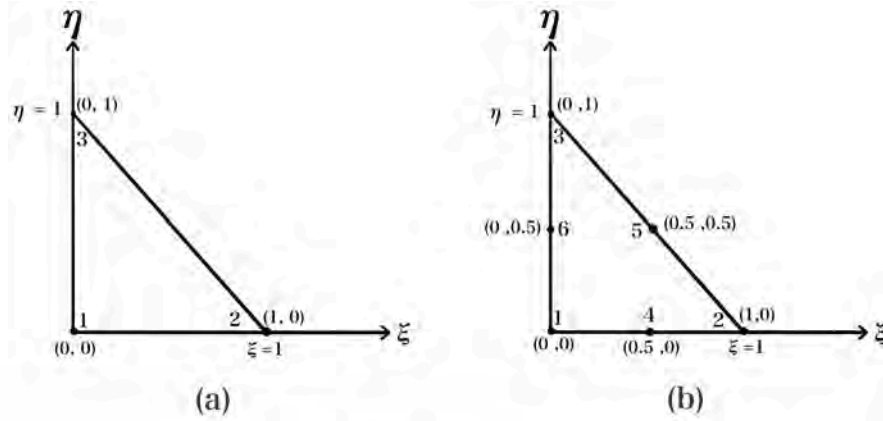


Figure 2.3: (a) Three-node triangular element in the natural coordinate (b) Six-node triangular element in the natural coordinate.

The shape functions of the linear elements are as follows:

$$\begin{aligned}\psi_1(\xi, \eta) &= 1 - \xi - \eta, \\ \psi_2(\xi, \eta) &= \xi, \\ \psi_3(\xi, \eta) &= \eta,\end{aligned}\tag{2.38}$$

and the shape functions of the quadratic elements are given below

$$\begin{aligned}\psi_1(\xi, \eta) &= (1 - \xi - \eta)(1 - 2\xi - 2\eta), \\ \psi_2(\xi, \eta) &= \xi(2\xi - 1), \\ \psi_3(\xi, \eta) &= \eta(2\eta - 1), \\ \psi_4(\xi, \eta) &= 4\xi(1 - \xi - \eta), \\ \psi_5(\xi, \eta) &= 4\xi\eta, \\ \psi_6(\xi, \eta) &= 4\eta(1 - \xi - \eta).\end{aligned}\tag{2.39}$$

Here,  $\xi$  and  $\eta$  are the natural coordinates.

The point  $(\xi, \eta)$  in the natural coordinate system are mapped to the physical coordinate  $(x, y)$  as follows:

$$x(\xi, \eta) = \sum_{i=1}^n \psi_i(\xi, \eta)x_i,\tag{2.40}$$

$$y(\xi, \eta) = \sum_{i=1}^n \psi_i(\xi, \eta)y_i,\tag{2.41}$$

where  $x_i$  and  $y_i$  represent the  $i^{th}$  node in physical coordinates system,  $\psi_i(\xi, \eta)$  is the shape function associated with the  $i^{th}$  node and  $n$  is the total number of nodes in the element. Any field variable can be interpolated using the shape functions,

$$u(\xi, \eta) = \sum_{i=1}^n \psi_i(\xi, \eta)u_i,\tag{2.42}$$

This material is reserved for educational use only, not allowed for commercial use.

Forbidden to modify the content, and cite the document when use.

To compute the derivatives of the shape functions  $\psi_i(\xi, \eta)$  with respect to the physical coordinate, we use the chain rule

$$\begin{aligned}\frac{\partial}{\partial \xi} &= \frac{\partial x}{\partial \xi} \frac{\partial}{\partial x} + \frac{\partial y}{\partial \xi} \frac{\partial}{\partial y}, \\ \frac{\partial}{\partial \eta} &= \frac{\partial x}{\partial \eta} \frac{\partial}{\partial x} + \frac{\partial y}{\partial \eta} \frac{\partial}{\partial y}.\end{aligned}\quad (2.43)$$

Rewriting Eq. (2.43) in matrix form yields

$$\begin{Bmatrix} \frac{\partial}{\partial \xi} \\ \frac{\partial}{\partial \eta} \end{Bmatrix} = \begin{bmatrix} \frac{\partial x}{\partial \xi} & \frac{\partial y}{\partial \xi} \\ \frac{\partial x}{\partial \eta} & \frac{\partial y}{\partial \eta} \end{bmatrix} \begin{Bmatrix} \frac{\partial}{\partial x} \\ \frac{\partial}{\partial y} \end{Bmatrix}.\quad (2.44)$$

The  $2 \times 2$  matrix on the right-hand side is known as the Jacobian matrix

$$[J] = \begin{bmatrix} J_{11} & J_{12} \\ J_{21} & J_{22} \end{bmatrix} = \begin{bmatrix} \frac{\partial x}{\partial \xi} & \frac{\partial y}{\partial \xi} \\ \frac{\partial x}{\partial \eta} & \frac{\partial y}{\partial \eta} \end{bmatrix},\quad (2.45)$$

where

$$\begin{aligned}J_{11} &= \frac{\partial x}{\partial \xi} = \sum_{i=1}^n \frac{\partial \psi_i(\xi, \eta)}{\partial \xi} x_i, \\ J_{12} &= \frac{\partial y}{\partial \xi} = \sum_{i=1}^n \frac{\partial \psi_i(\xi, \eta)}{\partial \xi} y_i, \\ J_{21} &= \frac{\partial x}{\partial \eta} = \sum_{i=1}^n \frac{\partial \psi_i(\xi, \eta)}{\partial \eta} x_i, \\ J_{22} &= \frac{\partial y}{\partial \eta} = \sum_{i=1}^n \frac{\partial \psi_i(\xi, \eta)}{\partial \eta} y_i.\end{aligned}\quad (2.46)$$

Rewriting Eq. (2.44), we have

$$\begin{Bmatrix} \frac{\partial}{\partial x} \\ \frac{\partial}{\partial y} \end{Bmatrix} = \begin{bmatrix} J_{11} & J_{12} \\ J_{21} & J_{22} \end{bmatrix}^{-1} \begin{Bmatrix} \frac{\partial}{\partial \xi} \\ \frac{\partial}{\partial \eta} \end{Bmatrix}.\quad (2.47)$$

For example, the derivatives of the shape functions  $\psi_i(\xi, \eta)$  with respect to  $x$  and  $y$  using the chain rule are

$$\begin{Bmatrix} \frac{\partial \psi_i(\xi, \eta)}{\partial x} \\ \frac{\partial \psi_i(\xi, \eta)}{\partial y} \end{Bmatrix} = \begin{bmatrix} J_{11} & J_{12} \\ J_{21} & J_{22} \end{bmatrix}^{-1} \begin{Bmatrix} \frac{\partial \psi_i(\xi, \eta)}{\partial \xi} \\ \frac{\partial \psi_i(\xi, \eta)}{\partial \eta} \end{Bmatrix}.\quad (2.48)$$

Next, we present the Finite Element Method (FEM). The basic idea of FEM is to divide a problem domain into finite subdomains, called finite elements. These finite elements are connected at specific points, called nodes, to create a mesh that covers the entire domain. The FEM starts from the weak formulation Eq. (2.28) and then we divide the domain  $\Omega$  into  $N_e$  elements. Therefore Eq. (2.28) becomes

$$\sum_{e=1}^{N_e} \int_{\Omega^e} - \left( \frac{\partial w}{\partial x} \frac{\partial u}{\partial x} + \frac{\partial w}{\partial y} \frac{\partial u}{\partial y} \right) d\Omega^e = \sum_{e=1}^{N_e} \int_{\Omega^e} w f(x, y) d\Omega^e - \sum_{e=1}^{N_e} \int_{\Gamma^e} w \left( \frac{\partial u}{\partial x} n_x + \frac{\partial u}{\partial y} n_y \right) d\Gamma^e.\quad (2.49)$$

The weight function  $w$  in Eq. (2.49) can be chosen based on approaches. Here we present some schemes.

Forbidden to modify the content, and cite the document when use.

1) Collocation Method: The weight function is chosen as a Dirac delta function. That is

$$w = \delta(x-x_i), \quad (2.50)$$

where  $x_i$  is the sampling point within the domain.

2) Least-Squares Method: The weight function is determined from the residual such that

$$w = \frac{dR}{da}, \quad (2.51)$$

where  $R$  is the residual and  $a$  represents the unknowns.

3) Galerkin Method: The weight functions are chosen to be the same as the shape functions. That is

$$w = \psi(x), \quad (2.52)$$

where  $\psi(x)$  is the shape function.

To apply FEM to solve the PDE, the unknown  $u(x)$  is approximated by using the form

$$u(x) \approx \sum_{i=1}^n \psi_i(x) u_i = \psi^T \mathbf{u}, \quad (2.53)$$

where  $n$  is the number of node in each element,  $\psi$  is the shape function and the superscript  $T$  is transpose. For the Galerkin method, the weight function is chosen to be the same as the shape function. That is

$$w = \psi(x). \quad (2.54)$$

Substituting Eqs. (2.54) and (2.53) into (2.49), we have

$$\sum_{e=1}^{N_e} \int_{\Omega^e} - \left( \frac{\partial \psi}{\partial x} \frac{\partial \psi^T}{\partial x} + \frac{\partial \psi}{\partial y} \frac{\partial \psi^T}{\partial y} \right) d\Omega^e \mathbf{u} = \sum_{e=1}^{N_e} \int_{\Omega^e} \psi f(x, y) d\Omega^e - \sum_{e=1}^{N_e} \int_{\Gamma^e} \psi \left( \frac{\partial \psi^T}{\partial x} n_x + \frac{\partial \psi^T}{\partial y} n_y \right) d\Gamma^e \mathbf{u}. \quad (2.55)$$

Next, we consider the integration over each element

$$\int_{\Omega^e} - \left( \frac{\partial \psi}{\partial x} \frac{\partial \psi^T}{\partial x} + \frac{\partial \psi}{\partial y} \frac{\partial \psi^T}{\partial y} \right) d\Omega^e \mathbf{u} = \int_{\Omega^e} \psi f(x, y) d\Omega^e - \int_{\Gamma^e} \psi \left( \frac{\partial \psi^T}{\partial x} n_x + \frac{\partial \psi^T}{\partial y} n_y \right) d\Gamma^e \mathbf{u}. \quad (2.56)$$

For the linear triangular element, we can choose the shape functions defined in Eq. (2.35). By substituting these shape functions into Eq. (2.56), we can rewrite the equation in matrix form as

$$\begin{bmatrix} k_{11} & k_{12} & k_{13} \\ k_{21} & k_{22} & k_{23} \\ k_{31} & k_{32} & k_{33} \end{bmatrix} \begin{Bmatrix} u_1 \\ u_2 \\ u_3 \end{Bmatrix} = \begin{Bmatrix} f_1 \\ f_2 \\ f_3 \end{Bmatrix}, \quad (2.57)$$

where

$$k_{ij} = \int_{\Omega^e} - \left( \frac{\partial \psi_i}{\partial x} \frac{\partial \psi_j}{\partial x} + \frac{\partial \psi_i}{\partial y} \frac{\partial \psi_j}{\partial y} \right) d\Omega^e, \quad (2.58)$$

This material is reserved for educational use only, not allowed for commercial use.  
 $f_i = \int_{\Omega^e} f(x, y) \psi_i d\Omega^e - \int_{\Gamma^e} \psi_i \left( \frac{\partial \psi_j}{\partial x} n_x + \frac{\partial \psi_j}{\partial y} n_y \right) d\Gamma^e u_i, i, j = 1, 2, 3.$   
 Forbidden to modify the content, and cite the document when use.

Once the local matrices for all elements are computed, they are assembled into the global stiffness matrix. Thus, the global stiffness matrix of Eq. (2.57) is

$$\begin{bmatrix} K_{11} & K_{12} & \cdots & K_{1n_{\text{dof}}} \\ K_{21} & K_{22} & \cdots & K_{2n_{\text{dof}}} \\ \vdots & \vdots & \ddots & \vdots \\ K_{n_{\text{dof}}1} & K_{n_{\text{dof}}2} & \cdots & K_{n_{\text{dof}}n_{\text{dof}}} \end{bmatrix} \begin{Bmatrix} u_1 \\ u_2 \\ \vdots \\ u_{n_{\text{dof}}} \end{Bmatrix} = \begin{Bmatrix} f_1 \\ f_2 \\ \vdots \\ f_{n_{\text{dof}}} \end{Bmatrix}, \quad (2.59)$$

or

$$[\mathbf{K}]\{\mathbf{U}\} = \{\mathbf{F}\}, \quad (2.60)$$

where  $n_{\text{dof}}$  is the total number of node in the domain.

## 2.6 Newton's Method

Newton's method is commonly used to solve nonlinear equations iteratively by using an initial guess and then updating the solution until the convergence is reached. Note that the initial guess for Newton's method can be determined using various techniques, such as the Bisection method, grid search, or other approaches, depending on the problem's requirements and available information. In this section, we present the formulations of the Newton's method in both one dimension and in higher dimensions.

### 2.6.1 One-Dimensional Newton's Method

Consider the one-dimensional case of the nonlinear equation,

$$u \frac{du}{dx} = f(x) \quad (2.61)$$

where  $u$  is the unknown solution and  $f$  is source term. Define the residual function  $R(u)$  as

$$R(u) = u \frac{du}{dx} - f(x) = 0. \quad (2.62)$$

To approximate the residual function  $R(u)$  around the current guess  $u^{(I)}$  at iteration  $I$ , we apply a Taylor expansion and neglecting higher-order terms yields

$$R(u) \approx R(u^{(I)}) + \Delta u \left. \frac{dR}{du} \right|_{u^{(I)}}, \quad (2.63)$$

where  $\Delta u = u - u^{(I)}$  and  $u^{(I)}$  is known. Substituting Eq. (2.63) into (2.62) and updating  $u$  to be  $u^{(I+1)}$ , we have

$$R(u^{(I)}) + (u^{(I+1)} - u^{(I)}) \left. \frac{dR}{du} \right|_{u^{(I)}} = 0. \quad (2.64)$$

Rearranging Eq. (2.64), we obtain

$$u^{(I+1)} = u^{(I)} - \frac{R(u^{(I)})}{\left. \frac{dR}{du} \right|_{u^{(I)}}}. \quad (2.65)$$

This material is reserved for educational use only.  $\left. \frac{dR}{du} \right|_{u^{(I)}}$  not allowed for commercial use.

Forbidden to modify the content, and cite the document when use.

It is important to ensure that the derivative  $\frac{dR}{du}$  is nonzero to ensure the Newton iteration is well-defined. The iterations stop when  $|u^{(I+1)} - u^{(I)}| < \text{tolerance}$ , where tolerance is the threshold of acceptable error for an application, typically the tolerance is chosen to be  $10^{-4}$ ,  $10^{-6}$  or  $10^{-8}$ , depending on the desired accuracy.

**Example:** Consider the nonlinear equation

$$2u^2 + \frac{8}{3}u = \frac{2}{3}. \quad (2.66)$$

Rewriting it into the standard form

$$R(u) = 2u^2 + \frac{8}{3}u - \frac{2}{3} = 0. \quad (2.67)$$

The derivative of the residual function is

$$\frac{dR}{du} = 4u + \frac{8}{3}. \quad (2.68)$$

The initial guess  $u^{(0)}$  is chosen using the Bisection method, with  $u^{(0)} = 0.5$ . The tolerance is set to  $10^{-6}$ . For  $I = 0$ , we compute the first iteration using the formula (2.65). That is

$$u^{(1)} = u^{(0)} - \frac{R(u^{(0)})}{\left.\frac{dR}{du}\right|_{u^{(0)}}}, \quad (2.69)$$

where the residual  $R(u^{(0)})$  and its derivative  $\left.\frac{dR}{du}\right|_{u^{(0)}}$  are

$$R(u^{(0)}) = 2(0.5)^2 + \frac{8}{3}(0.5) - \frac{2}{3} \approx 1.1667 \quad (2.70)$$

and

$$\left.\frac{dR}{du}\right|_{u^{(0)}} = 4(0.5) + \frac{8}{3} \approx 4.6667. \quad (2.71)$$

Substituting Eqs. (2.70) and (2.71) into (2.69), we have

$$u^{(1)} = 0.5 - \frac{1.1667}{4.6667} \approx 0.25. \quad (2.72)$$

The error is

$$|u^{(1)} - u^{(0)}| = |0.25 - 0.5| = 0.25 > 10^{-6}, \quad (2.73)$$

which is greater than the tolerance  $10^{-6}$ . Then we proceed to the next iteration using  $u^{(1)} = 0.25$ . Therefore, the the residual  $R(u^{(1)})$  and its derivative  $\left.\frac{dR}{du}\right|_{u^{(1)}}$  are

$$R(u^{(1)}) = 2(0.25)^2 + \frac{8}{3}(0.25) - \frac{2}{3} \approx 0.125 \quad (2.74)$$

and

$$\left.\frac{dR}{du}\right|_{u^{(1)}} = 4(0.25) + \frac{8}{3} \approx 3.6667. \quad (2.75)$$

Next, we update  $u^{(2)}$

$$u^{(2)} = u^{(1)} - \frac{R(u^{(1)})}{\left.\frac{dR}{du}\right|_{u^{(1)}}} = 0.25 - \frac{0.125}{3.6667} \approx 0.2159091. \quad (2.76)$$

The error is

$$|u^{(2)} - u^{(1)}| = |0.2159091 - 0.25| = 0.0340909 > 10^{-6}. \quad (2.77)$$

Forbidden to modify the content, and cite the document when use.

So, the process continues iteratively until reaching the condition  $|u^{(I+1)} - u^{(I)}| < \text{tolerance}$ . The computed values of  $u$  and the corresponding number of iterations are summarized in Table 2.2. This table shows the iterative results of solving the one-dimensional nonlinear equation using the Newton's method. In each iteration, the value of  $u$  is updated, while the error decreases until it becomes less than the tolerance,  $10^{-6}$ . At the fourth iteration, we obtain the solution  $u = 0.2152504$  and the error is  $2.4577 \times 10^{-7}$ .

**Table 2.2:** Iterative results of the one-dimensional nonlinear equation (2.66).

Iteration $I$	$u$	Error
0 (initial guess)	0.5	
1	0.25	0.25
2	0.2159091	0.0340909
3	0.2152507	$6.5840 \times 10^{-4}$
4	0.2152504	$2.4577 \times 10^{-7}$

### 2.6.2 $N$ -Dimensional Newton's Method

Newton's method can be extended to solve a system of  $N$ -dimensional nonlinear equations. Consider

$$\mathbf{R}(\mathbf{u}) = \mathbf{0}, \quad (2.78)$$

where  $\mathbf{R}(\mathbf{u})$  is the residual vector and  $\mathbf{u}$  is the unknown vector

$$\mathbf{R}(\mathbf{u}) = \begin{bmatrix} R_1(\mathbf{u}) \\ R_2(\mathbf{u}) \\ \vdots \\ R_n(\mathbf{u}) \end{bmatrix}, \quad \text{and} \quad \mathbf{u} = \begin{bmatrix} u_1 \\ u_2 \\ \vdots \\ u_n \end{bmatrix}. \quad (2.79)$$

The term of  $\mathbf{R}(\mathbf{u})$  can be expanded around the current guess  $\mathbf{u}^{(I)}$  at iteration  $I$  using the Taylor expansion and dropping higher-order terms:

$$\mathbf{R}(\mathbf{u}) \approx \mathbf{R}(\mathbf{u}^{(I)}) + \left. \frac{\partial \mathbf{R}}{\partial \mathbf{u}} \right|_{\mathbf{u}^{(I)}} \Delta \mathbf{u}, \quad (2.80)$$

where  $\Delta \mathbf{u} = \mathbf{u} - \mathbf{u}^{(I)}$ , and  $\mathbf{u}^{(I)}$  is the known vector. Substituting Eq. (2.80) into Eq. (2.78), we have

$$\mathbf{R}(\mathbf{u}^{(I)}) + \left. \frac{\partial \mathbf{R}}{\partial \mathbf{u}} \right|_{\mathbf{u}^{(I)}} \Delta \mathbf{u} = \mathbf{0}. \quad (2.81)$$

Updating  $\mathbf{u}$  to be  $\mathbf{u}^{(I+1)}$ , we obtain

$$\mathbf{R}(\mathbf{u}^{(I)}) = - \left. \frac{\partial \mathbf{R}}{\partial \mathbf{u}} \right|_{\mathbf{u}^{(I)}} (\mathbf{u}^{(I+1)} - \mathbf{u}^{(I)}) \equiv -J(\mathbf{u}^{(I)})(\mathbf{u}^{(I+1)} - \mathbf{u}^{(I)}), \quad (2.82)$$

where  $J$  is the Jacobian matrix and

$$J = \frac{\partial \mathbf{R}}{\partial \mathbf{u}} \Big|_{\mathbf{u}^{(I)}} = \begin{bmatrix} \frac{\partial R_1}{\partial u_1} & \frac{\partial R_1}{\partial u_2} & \dots & \frac{\partial R_1}{\partial u_n} \\ \frac{\partial R_2}{\partial u_1} & \frac{\partial R_2}{\partial u_2} & \dots & \frac{\partial R_2}{\partial u_n} \\ \vdots & \vdots & \ddots & \vdots \\ \frac{\partial R_n}{\partial u_1} & \frac{\partial R_n}{\partial u_2} & \dots & \frac{\partial R_n}{\partial u_n} \end{bmatrix} \Big|_{\mathbf{u}^{(I)}}. \quad (2.83)$$

To find the unknown  $\mathbf{u}^{(I+1)}$  in Eq. (2.82), we rearrange Eq. (2.82) to be

$$\mathbf{u}^{(I+1)} = \mathbf{u}^{(I)} - J^{-1}(\mathbf{u}^{(I)})\mathbf{R}(\mathbf{u}^{(I)}). \quad (2.84)$$

It is important to ensure that  $\det(J(\mathbf{u}^{(I)})) \neq 0$  to avoid singularities in the Newton iteration. The iterations stop when  $\|\mathbf{u}^{(I+1)} - \mathbf{u}^{(I)}\|_2 < \text{tolerance}$ , where  $\|\cdot\|_2$  is the  $l_2$ -norm.

**Example:** Consider the nonlinear system of equations

$$\begin{aligned} 2u_1^2 - 2u_2^2 + 3u_1u_2 &= \frac{5}{4}, \\ \frac{3}{8}u_1^2 + 2u_2 + 2u_1u_2 &= 1. \end{aligned} \quad (2.85)$$

The residual vector is

$$\mathbf{R}(\mathbf{u}^{(I)}) = \begin{bmatrix} R_1(u_1, u_2) \\ R_2(u_1, u_2) \end{bmatrix} \Big|_{\mathbf{u}^{(I)}} = \begin{bmatrix} 2u_1^2 - 2u_2^2 + 3u_1u_2 - \frac{5}{4} \\ \frac{3}{8}u_1^2 + 2u_2 + 2u_1u_2 - 1 \end{bmatrix} \Big|_{\mathbf{u}^{(I)}}. \quad (2.86)$$

The Jacobian matrix  $J$  can be written as

$$J = \frac{\partial \mathbf{R}}{\partial \mathbf{u}} \Big|_{\mathbf{u}^{(I)}} = \begin{bmatrix} \frac{\partial R_1}{\partial u_1} & \frac{\partial R_1}{\partial u_2} \\ \frac{\partial R_2}{\partial u_1} & \frac{\partial R_2}{\partial u_2} \end{bmatrix} \Big|_{\mathbf{u}^{(I)}} = \begin{bmatrix} 4u_1 + 3u_2 & -4u_2 + 3u_1 \\ \frac{3}{4}u_1 + 2u_2 & 2 + 2u_1 \end{bmatrix} \Big|_{\mathbf{u}^{(I)}}. \quad (2.87)$$

The tolerance is chosen to be  $10^{-6}$ . The initial guess  $\mathbf{u}^{(0)}$  is determined using a grid search technique, with

$$\begin{bmatrix} u_1^{(0)} \\ u_2^{(0)} \end{bmatrix} = \begin{bmatrix} 0.6 \\ 0.4 \end{bmatrix}. \quad (2.88)$$

For the first iteration, we need to calculate the residual and Jacobian matrix by substituting the initial guess Eq. (2.88) into Eqs. (2.86) and (2.87), we have

$$\mathbf{R}(\mathbf{u}^{(0)}) = \begin{bmatrix} R_1(u_1^{(0)}, u_2^{(0)}) \\ R_2(u_1^{(0)}, u_2^{(0)}) \end{bmatrix} = \begin{bmatrix} 2(0.6)^2 - 2(0.4)^2 + 3(0.6)(0.4) - \frac{5}{4} \\ \frac{3}{8}(0.6)^2 + 2(0.4) + 2(0.6)(0.4) - 1 \end{bmatrix} = \begin{bmatrix} -0.130 \\ 0.415 \end{bmatrix} \quad (2.89)$$

and

$$J = \frac{\partial \mathbf{R}}{\partial \mathbf{u}} \Big|_{\mathbf{u}^{(0)}} = \begin{bmatrix} 4(0.6) + 3(0.4) & -4(0.4) + 3(0.6) \\ \frac{3}{4}(0.6) + 2(0.4) & 2 + 2(0.6) \end{bmatrix} = \begin{bmatrix} 3.60 & 0.20 \\ 1.25 & 3.20 \end{bmatrix}. \quad (2.90)$$

To update  $\mathbf{u}^{(1)}$ , we use the formula (2.84). That is

$$\mathbf{u}^{(1)} = \mathbf{u}^{(0)} - J^{-1}(\mathbf{u}^{(0)})\mathbf{R}(\mathbf{u}^{(0)}). \quad (2.91)$$

Substituting Eqs. (2.89) and (2.90) into Eq. (2.91), we have

$$\begin{bmatrix} u_1^{(1)} \\ u_2^{(1)} \end{bmatrix} = \begin{bmatrix} 0.6 \\ 0.4 \end{bmatrix} - \begin{bmatrix} 3.60 & 0.20 \\ 1.25 & 3.20 \end{bmatrix}^{-1} \begin{bmatrix} -0.130 \\ 0.415 \end{bmatrix} = \begin{bmatrix} 0.6442768 \\ 0.2530169 \end{bmatrix} \quad (2.92)$$

This material is reserved for educational use only, not allowed for commercial use. Forbidden to modify the content, and cite the document when use.

Checking the error:

$$\|\mathbf{u}^{(1)} - \mathbf{u}^{(0)}\|_2 = \sqrt{(0.6442768 - 0.6)^2 + (0.2530169 - 0.4)^2} \approx 0.1535073 > 10^{-6}. \quad (2.93)$$

The process continues iteratively until the condition  $\|u^{(I+1)} - u^{(I)}\|_2 < \text{tolerance}$  is satisfied. The computed values of  $\mathbf{u}$  and the corresponding number of iterations are summarized in Table 2.3. Table 2.3 presents the results of applying the Newton's method to the two-dimensional nonlinear system of equations. The process begins with initial guesses of  $u_1 = 0.6$  and  $u_2 = 0.4$  and the values of  $u_1$  and  $u_2$  are updated in each iteration to improve the solution. As the iterations progress, the error decreases, and by the fourth iteration, the values of  $u_1$  and  $u_2$  are 0.6622040 and 0.2513401, respectively. At this point, the error is  $1.3593 \times 10^{-8}$ , which is less than the tolerance  $10^{-6}$ .

**Table 2.3:** Iterative results of the two-dimensional nonlinear system of equations (2.85).

Iteration $I$	$u_1$	$u_2$	Error
0 (initial guess)	0.6	0.4	
1	0.6442768	0.2530169	0.1535073
2	0.6623773	0.2513064	0.0181811
3	0.6622040	0.2513401	$1.7651 \times 10^{-4}$
4	0.6622040	0.2513401	$1.3593 \times 10^{-8}$

Next, we introduce the parameters used in this study, the permeability and the porosity.

## 2.7 Permeability

Permeability is the parameter indicating the ability of a material that fluid can pass through a material or its pores. This property is crucial in fluid dynamics and porous media studies, as it directly influences how liquids flow through structures. For instance, Figures 2.4(a) and (b) illustrate the domains of fluid flow through rock and sand, respectively. It can be observed that the fluid flows more easily through the rock than through the sand, indicating that the rock domain has a higher permeability than the sand domain. This means that the rock domain has more void space, allowing the fluid to pass through it more easily, whereas the sand domain offers more resistance to fluid flow.

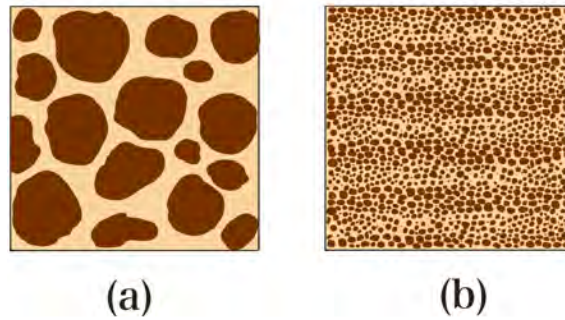


Figure 2.4: The domain of fluid flow through the solid phase (a) rock and (b) sand.

## 2.8 Porosity

The porosity ( $\varepsilon^l$ ) is defined by the volume of the fluid divided by the total volume over the domain. Figure 2.5 shows the domain consisting of fluid and solid phases. In this system, the solid phase is a part of the total volume, while the remaining space is filled by the fluid phase.

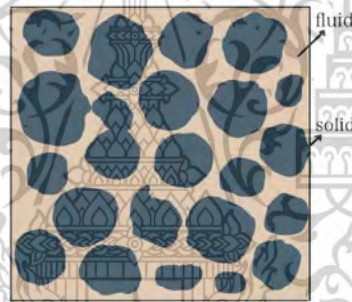


Figure 2.5: The porosity.

The porosity

$$\varepsilon^l = \frac{\nu_{\text{fluid}}}{\nu_{\text{total}}}, \quad (2.94)$$

where  $\varepsilon^l$  is the porosity,  $\nu_{\text{fluid}}$  is the volume of the fluid within the domain and  $\nu_{\text{total}}$  is the total volume of the domain, including both solid and fluid phases.

### Remarks

#### 1. Fully fluid domain

If the domain contains only fluid (no solid), the fluid volume is equal to the total volume ( $\nu_{\text{fluid}} = \nu_{\text{total}}$ ). It implies that

$$\varepsilon^l = 1. \quad (2.95)$$

#### 2. Fully solid domain

If the domain is completely filled with solid (no fluid), the fluid volume is zero ( $\nu_{\text{fluid}} = 0$ ). It implies that

$$\varepsilon^l = 0. \quad (2.96)$$

This material is reserved for educational use only, not allowed for commercial use.

Forbidden to modify the content, and cite the document when use.

That is  $\varepsilon^l = 1 - \varepsilon^s$ , where  $\varepsilon^s$  is the volume of solid divided by total volume.

**Example:** Consider a domain with a total volume ( $\nu_{\text{total}}$ ) of  $3 \mu\text{m}^3$ , where the fluid volume ( $\nu_{\text{fluid}}$ ) is  $1.2 \mu\text{m}^3$ .

Substituting these values into Eq. (2.94), we have

$$\varepsilon^l = \frac{\nu_{\text{fluid}}}{\nu_{\text{total}}} = \frac{1.2}{3} = 0.4. \quad (2.97)$$

Thus, the porosity  $\varepsilon^l$  is 0.4 or 40%, meaning that 40% of the total volume is occupied by the fluid.

## 2.9 Literature Review

Mucus is a vital component in the human respiratory system, playing a crucial role in maintaining respiratory health by protecting the airways from harmful substances. It is primarily composed of 95% water, 2–3% glycoproteins and proteins, 1% minerals, 1% lipids, and 0.02% DNA [22, 29]. However, excessive mucus production can result in some illness. The mucus forms a protective layer above the periciliary layer (PCL) in the respiratory tract, acting as a barrier to trap harmful substances. It is then expelled from the body through a natural mechanism called mucociliary clearance (MCC) [11]. The MCC has been extensively investigated and well documented in scientific literature [2, 5, 6, 15, 19, 20, 24, 34, 37]. For instance, R. Bansil and B.S. Turner [1] reviewed the fundamental aspects of mucus including its structure, synthesis, composition, and secretion. M. Jory et al. [16] studied mucus in human bronchial epithelial (HBE) cultures and measured the viscoelastic properties of HBE mucus from patients with chronic obstructive pulmonary disease (COPD), and smokers. S.J. Kelly et al. [18] investigated water sorption properties of human airway mucus and analyzed the available mucus samples from COPD, cystic fibrosis (CF) patients and healthy individuals. S. Ren et al. [30] used the Eulerian wall film model to simulate four coughing strategies for patients with COPD and neuromuscular disorders, highlighting the impact of mucus thickness and viscosity on cough efficiency. W.L. Lee et al. [20] studied a two-layer Newtonian fluid model, which consists of an upper mucus layer and a lower periciliary layer. Based on the projection method combined with the Immersed Boundary Method, he simulated the mucociliary transport process with the prescribed velocity of the beating cilia. Since mucus is expelled from the body by the movement of cilia, the investigation of ciliary motion has become a key component in understanding the MCC. For example, M.H. Sedaghat et al. [33] studied the effect of cilia abnormalities on the MCC in bronchial airways. L. Xu and Y. Jiang [44] investigated the motion of five rods (cilia) using a rod-propel-fluid model. They observed that the differences in cilium height significantly enhanced driven transport efficiency, while an increase in cilia density and beating frequency enhanced the transport capacity of the MCC. P.R. Sear et al. [32] studied

ciliary motion by using video microscopy to record planar ciliary motions that could be used to validate mathematical models or investigate ciliary function such as in primary ciliary dyskinesia (PCD).

Several studies have employed mathematical models to describe the behavior of fluid flow in the periciliary layer (PCL) and mucus layer (ML). For example, K. Fujisawa and A. Murakami [14] investigated flows in porous medium and free-fluid domains in the PCL using Darcy-Brinkman equations. S. Poopra and K. Wuttanachamsri [27, 28], and S. Suankasem et al. [35], employed the asymptotic expansion method to one-dimensional macroscale Stokes-Brinkman equations to determine the velocities of PCL fluid using different approaches. S. Phaenchat and K. Wuttanachamsri [26], T. Kasamwan and K. Wuttanachamsri [17], and N. Oangwatcharaprajan and K. Wuttanachamsri [25] have previously determined the velocities of PCL fluid using a finite element method for one-dimensional nonlinear Stokes-Brinkman, unsteady-state Stokes-Brinkman, and Navier-Stokes-Brinkman equations, respectively. In their approaches, the transient and nonlinear terms are solved by a finite difference method and classical linearization method, respectively. K. Chamsri [8] discretized n-dimensional macroscale Stokes-Brinkman equations by using a mixed finite element method which was employed to find the velocity of the PCL fluid in [42]. K. Wuttanachamsri [40] studied the free interfaces at the tips of cilia using a macroscale Brinkman equation. V.S. Verma and V. Rana [38] employed steady-state mathematical modeling to examine mucus transport in the human lung airways across two layers: the free-fluid region and the mucus layer (ML). M. A. Modaresi and E. Shirani [23] investigated the velocities of both the periciliary layer (PCL) and ML using three-dimensional mathematical models. These velocities were influenced by various in mucus viscosity and exhibited distinct behaviors at the PCL/ML interface during coughing and sneezing.

# Chapter 3

## Mathematical Models

In this chapter, in the beginning, we present the discretization of the governing equations using a mixed finite element method of the Taylor-Hood type. The boundary conditions applied in this work for the domains  $\Omega_1$  to  $\Omega_4$  are presented in Section 3.2.

### 3.1 Model Discretization

In this section, we present the discretization of the equations, provided in Chapter 2. These equations include the nonlinear Brinkman equation, the steady-state Navier-Stokes equation, and the Stokes equation. They are discretized using the mixed finite element method of Taylor-Hood type, and the nonlinear term is handled by the Newton's method.

#### 3.1.1 The Nonlinear Brinkman Equation

In this section, we present the discretization of the nonlinear Brinkman equation and the continuity equation, which describes the fluid flow in the domain  $\Omega_1$ . The equations are given by [39, 43]

$$\rho(\mathbf{v}^l \cdot \nabla \mathbf{v}^l) + \nabla p - \frac{\mu}{\varepsilon^l} (\Delta \varepsilon^l \mathbf{v}^l + \nabla \cdot (\nabla \cdot \varepsilon^l \mathbf{v}^l)) - \rho \mathbf{g} = -\mu \mathbf{k}^{-1} \cdot (\varepsilon^l \mathbf{v}^l - \varepsilon^l \mathbf{v}^s), \quad (3.1)$$

$$\varepsilon^l \nabla \cdot \mathbf{v}^l = f, \quad (3.2)$$

where the variable  $\mathbf{v}^l$  is the velocity of the liquid phase,  $\rho$  is the fluid density,  $\varepsilon^l$  is the porosity,  $\mu$  is a dynamic viscosity,  $\mathbf{g}$  is gravity,  $\mathbf{k}^{-1}$  is the inverse of the permeability tensor,  $p$  is pressure,  $\mathbf{v}^s$  is the velocities of the solid phase. The function  $f$  is given by

$$f = -\frac{\dot{\varepsilon}^l}{(1 - \varepsilon^l)} + \nabla \cdot \varepsilon^l \mathbf{v}^s, \quad (3.3)$$

where

$$\dot{\varepsilon}^l = \frac{\partial \varepsilon^l}{\partial t} + \mathbf{v}^s \cdot \nabla \varepsilon^l \quad (3.4)$$

represents the material time derivative of the porosity with respect to the solid phase. Define  $\mathbf{v} = \varepsilon^l \mathbf{v}^l$ . Since the porosity  $\varepsilon^l$  is a constant, substituting Eq. (3.2) into the fourth term of Eq. (3.1), we have that Eqs.(3.1) - (3.2) become

$$\frac{\rho}{(\varepsilon^l)^2} (\mathbf{v} \cdot \nabla \mathbf{v}) + \nabla p - \frac{\mu}{\varepsilon^l} (\Delta \mathbf{v} + \nabla f) - \rho \mathbf{g} = -\mu \mathbf{k}^{-1} \cdot (\mathbf{v} - \varepsilon^l \mathbf{v}^s), \quad (3.5)$$

$$\nabla \cdot \mathbf{v} = f. \quad (3.6)$$

In the two-dimensional domain, the velocity vector  $\mathbf{v}$  is defined as

$$\mathbf{v} = \begin{pmatrix} v_1 \\ v_2 \end{pmatrix}, \quad (3.7)$$

This material is reserved for educational use only, not allowed for commercial use.

Forbidden to modify the content, and cite the document when use.

where  $v_1$  and  $v_2$  are the horizontal and vertical velocities, respectively. The gravity vector  $\mathbf{g}$  is given by

$$\mathbf{g} = \begin{pmatrix} g_1 \\ g_2 \end{pmatrix}, \quad (3.8)$$

where  $g_1$  and  $g_2$  represent the gravity in the horizontal and vertical directions, respectively. The inverse permeability matrix  $\mathbf{k}^{-1}$  is given by

$$\mathbf{k}^{-1} = \begin{pmatrix} k_{11}^{-1} & k_{12}^{-1} \\ k_{21}^{-1} & k_{22}^{-1} \end{pmatrix}. \quad (3.9)$$

The vector differential operator  $\nabla$  is defined as

$$\nabla = \frac{\partial}{\partial x_i} = \begin{pmatrix} \frac{\partial}{\partial x_1} \\ \frac{\partial}{\partial x_2} \end{pmatrix}, \quad (3.10)$$

where  $x_1$  and  $x_2$  specify the coordinates in the Cartesian coordinate system, indicating the horizontal and vertical axes, respectively. This operator is used to express as follows.

- Gradient of a scalar field  $f$ :

$$\nabla f = \frac{\partial f}{\partial x_i} = \begin{pmatrix} \frac{\partial f}{\partial x_1} \\ \frac{\partial f}{\partial x_2} \end{pmatrix}. \quad (3.11)$$

- Gradient of a vector field  $\mathbf{v}$ :

$$\nabla \mathbf{v} = \frac{\partial v_i}{\partial x_j} = \begin{pmatrix} \frac{\partial v_1}{\partial x_1} & \frac{\partial v_1}{\partial x_2} \\ \frac{\partial v_2}{\partial x_1} & \frac{\partial v_2}{\partial x_2} \end{pmatrix}. \quad (3.12)$$

- Divergence of a vector field  $\mathbf{v}$ :

$$\nabla \cdot \mathbf{v} = \frac{\partial v_j}{\partial x_j} = \frac{\partial v_1}{\partial x_1} + \frac{\partial v_2}{\partial x_2}. \quad (3.13)$$

- Laplacian of a vector field  $\mathbf{v}$ :

$$\Delta \mathbf{v} = \frac{\partial^2 v_i}{\partial x_j^2} = \begin{pmatrix} \frac{\partial^2 v_1}{\partial x_1^2} + \frac{\partial^2 v_1}{\partial x_2^2} \\ \frac{\partial^2 v_2}{\partial x_1^2} + \frac{\partial^2 v_2}{\partial x_2^2} \end{pmatrix}. \quad (3.14)$$

The equations (3.5) and (3.6) can be expressed in indicial notation as follows

$$\frac{\rho}{(\varepsilon^l)^2} \left( v_j \frac{\partial v_i}{\partial x_j} \right) + \frac{\partial p}{\partial x_i} - \frac{\mu}{\varepsilon^l} \left( \frac{\partial^2 v_i}{\partial x_j^2} + \frac{\partial f}{\partial x_i} \right) - \rho g_i = -\mu k_{ij}^{-1} (v_j - \varepsilon^l v_j^s), \quad (3.15)$$

$$\frac{\partial v_j}{\partial x_j} = f, \quad (3.16)$$

where  $i, j = 1, 2$ .

Before discretizing the two-dimensional nonlinear Brinkman equation used in the domain  $\Omega_1$ , we first derive the weak formulation of these equations. That is multiplying Eq. (3.15) by a weight function  $w$  and multiplying Eq. (3.16) by a weight function

$Q$ , and then integrating over the domain  $\Omega_1$ . We obtain

$$\int_{\Omega_1} \left[ \frac{\rho}{(\varepsilon^l)^2} \left( wv_j \frac{\partial v_i}{\partial x_j} \right) - \frac{\mu}{\varepsilon^l} \left( w \frac{\partial^2 v_i}{\partial x_j^2} \right) + \mu k_{ij}^{-1} wv_j + w \frac{\partial p}{\partial x_i} \right] d\Omega_1 \quad (3.17)$$

$$= \int_{\Omega_1} \left[ \rho g_i w + \frac{\mu}{\varepsilon^l} \left( w \frac{\partial f}{\partial x_i} \right) + \mu \varepsilon^l k_{ij}^{-1} wv_j^s \right] d\Omega_1,$$

$$\int_{\Omega_1} Q \frac{\partial v_j}{\partial x_j} d\Omega_1 = \int_{\Omega_1} Qf d\Omega_1. \quad (3.18)$$

Subsequently, we apply the Green's first identity to the second and fourth terms in Eq. (3.17), as well as the source term  $\frac{\mu}{\varepsilon^l} \left( w \frac{\partial f}{\partial x_i} \right)$ . Then, Eq. (3.17) becomes

$$\begin{aligned} & \int_{\Omega_1} \left[ \frac{\rho}{(\varepsilon^l)^2} \left( wv_j \frac{\partial v_i}{\partial x_j} \right) + \frac{\mu}{\varepsilon^l} \frac{\partial w}{\partial x_j} \frac{\partial v_i}{\partial x_j} + \mu k_{ij}^{-1} wv_j - \frac{\partial w}{\partial x_i} p \right] d\Omega_1 \\ &= \int_{\Omega_1} \left[ \rho g_i w - \frac{\mu}{\varepsilon^l} \frac{\partial w}{\partial x_i} f + \mu \varepsilon^l k_{ij}^{-1} wv_j^s \right] d\Omega_1 \\ &+ \int_{\Gamma_p} \left[ \frac{\mu}{\varepsilon^l} \left( w \frac{\partial v_i}{\partial x_j} n_j \right) - w p n_i + \frac{\mu}{\varepsilon^l} w f n_i \right] d\Gamma_p. \end{aligned} \quad (3.19)$$

Here,  $\Gamma_p$  represents the boundary of the domain  $\Omega_1$  and  $n_i$  (for  $i = 1, 2$ ), denotes an outward unit normal vector. Therefore, Eqs. (3.18) and (3.19) represent the weak formulation of the system of equations (3.15) - (3.16). Let  $\Omega_1 = \bigcup_e \Omega_1^e$ , where  $\Omega_1^e$  denotes the element domain. Then the integration over the domain  $\Omega_1$  can be represented as the summation of the integration over the element domain. That is

$$\begin{aligned} & \sum_{e=1}^{N_e} \int_{\Omega_1^e} \left[ \frac{\rho}{(\varepsilon^l)^2} \left( wv_j \frac{\partial v_i}{\partial x_j} \right) + \frac{\mu}{\varepsilon^l} \frac{\partial w}{\partial x_j} \frac{\partial v_i}{\partial x_j} + \mu k_{ij}^{-1} wv_j - \frac{\partial w}{\partial x_i} p \right] d\Omega_1^e \\ &= \sum_{e=1}^{N_e} \int_{\Omega_1^e} \left[ \rho g_i w - \frac{\mu}{\varepsilon^l} \frac{\partial w}{\partial x_i} f + \mu \varepsilon^l k_{ij}^{-1} wv_j^s \right] d\Omega_1^e \\ &+ \sum_{e=1}^{N_e} \int_{\Gamma_p^e} \left[ \frac{\mu}{\varepsilon^l} \left( w \frac{\partial v_i}{\partial x_j} n_j \right) - w p n_i + \frac{\mu}{\varepsilon^l} w f n_i \right] d\Gamma_p^e, \end{aligned} \quad (3.20)$$

$$\sum_{e=1}^{N_e} \int_{\Omega_1^e} Q \frac{\partial v_j}{\partial x_j} d\Omega_1^e = \sum_{e=1}^{N_e} \int_{\Omega_1^e} Qf d\Omega_1^e, \quad (3.21)$$

where  $N_e$  is the number of elements.

Define the space  $L_0^2(\Omega)$  as

$$L_0^2(\Omega) = \{p \in L^2(\Omega) : \int_{\Omega} p d\Omega = 0\}. \quad (3.22)$$

Let  $V_h$  and  $P_h$  be finite-dimensional subspaces of  $H^1(\Omega)$  and  $L_0^2(\Omega)$ . To find the dependent variables  $(v_i, p) \in V_h \times P_h$ , we approximate them by

$$v_i(\mathbf{x}) = \sum_{k=1}^{K_n} \psi_k(\mathbf{x}) v_i^k = \Psi^T \mathbf{V}_i, \quad i = 1, 2, \quad (3.23)$$

$$p(\mathbf{x}) = \sum_{l=1}^{L_n} \phi_l(\mathbf{x}) p_l = \Phi^T \mathbf{P}, \quad (3.24)$$

where  $\mathbf{V}_i$  and  $\mathbf{P}$  are vectors of the velocities and pressure, respectively. The superscript  $T$  denotes the transpose operation, and  $\psi_k$  and  $\phi_l$  are shape functions used for velocity  
 This material is reserved for educational use only, not allowed for commercial use.  
 Forbidden to modify the content, and cite the document when use.

and pressure approximations, respectively. The vectors  $\Psi$  and  $\Phi$  are the vector forms of the shape functions  $\psi_k$  and  $\phi_l$ , respectively. In this work, we adopt the Taylor–Hood mixed finite element method, where the velocity is approximated using quadratic shape functions and the pressure is approximated using linear shape functions. For triangular isoparametric elements, we use six nodes per element for the velocity approximation and three nodes per element for the pressure approximation; that is,  $K_n = 6$  and  $L_n = 3$ . Using the shape function  $\psi_k$ , we approximate the velocity of cilia as

$$v_j^s(\mathbf{x}) = \sum_{k=1}^{K_n} \psi_k(\mathbf{x})(v_j^s)^k = \Psi^T \mathbf{V}_j^s, \quad j = 1, 2. \quad (3.25)$$

The weight functions  $w$  and  $Q$  are chosen based on the Galerkin method and are therefore approximated by the shape functions as follows.

$$w \approx \psi_k, \quad Q \approx \phi_l. \quad (3.26)$$

Therefore, by substituting Eqs. (3.23) - (3.26) into Eqs. (3.20) and (3.21), the integration over each element is as follows

$$\begin{aligned} & \frac{\rho}{(\varepsilon^l)^2} \int_{\Omega_1^e} \Psi(\Psi^T \mathbf{V}_j) \frac{\partial \Psi^T}{\partial x_j} d\Omega_1^e \mathbf{V}_i + \frac{\mu}{\varepsilon^l} \int_{\Omega_1^e} \frac{\partial \Psi}{\partial x_j} \frac{\partial \Psi^T}{\partial x_j} d\Omega_1^e \mathbf{V}_i + \mu k_{ij}^{-1} \int_{\Omega_1^e} \Psi \Psi^T d\Omega_1^e \mathbf{V}_j \\ & - \int_{\Omega_1^e} \frac{\partial \Psi}{\partial x_i} \Phi^T d\Omega_1^e \mathbf{P} = \rho g_i \int_{\Omega_1^e} \Psi d\Omega_1^e - \frac{\mu}{\varepsilon^l} \int_{\Omega_1^e} \frac{\partial \Psi}{\partial x_i} f d\Omega_1^e + \mu \varepsilon^l k_{ij}^{-1} \int_{\Omega_1^e} \Psi \Psi^T \mathbf{V}_j^s d\Omega_1^e \\ & + \frac{\mu}{\varepsilon^l} \int_{\Gamma_p^e} \Psi \frac{\partial \Psi^T}{\partial x_j} n_j d\Gamma_p^e \mathbf{V}_i - \int_{\Gamma_p^e} \Psi \Phi^T n_i d\Gamma_p^e \mathbf{P} + \frac{\mu}{\varepsilon^l} \int_{\Gamma_p^e} \Psi f n_i d\Gamma_p^e, \end{aligned} \quad (3.27)$$

and

$$\int_{\Omega_1^e} \Phi \frac{\partial \Psi^T}{\partial x_j} d\Omega_1^e \mathbf{V}_j = \int_{\Omega_1^e} \Phi f d\Omega_1^e. \quad (3.28)$$

Thus, Eqs. (3.27) and (3.28) can be expressed in a matrix form as follows

$$\begin{bmatrix} N + A + B_{11} & B_{12} & -Z_1^T \\ B_{21} & N + A + B_{22} & -Z_2^T \\ Z_1 & Z_2 & \mathbf{0} \end{bmatrix} \begin{Bmatrix} \mathbf{V}_1 \\ \mathbf{V}_2 \\ \mathbf{P} \end{Bmatrix} = \begin{Bmatrix} F_1 \\ F_2 \\ E \end{Bmatrix}, \quad (3.29)$$

where the variables in the coefficients matrix are defined as

$$\begin{aligned}
N &= \frac{\rho}{(\varepsilon^l)^2} C_j(\mathbf{V}_j), \\
A &= \frac{\mu}{\varepsilon^l} K_{jj}, \\
C_j(\mathbf{V}_j) &= \int_{\Omega_1^e} \Psi(\Psi^T \mathbf{V}_j) \frac{\partial \Psi^T}{\partial x_j} d\Omega_1^e, \\
K_{jj} &= \int_{\Omega_1^e} \frac{\partial \Psi}{\partial x_j} \frac{\partial \Psi^T}{\partial x_j} d\Omega_1^e, \\
B_{ij} &= \mu k_{ij}^{-1} \int_{\Omega_1^e} \Psi \Psi^T d\Omega_1^e, \\
Z_i &= \int_{\Omega_1^e} \Phi \frac{\partial \Psi^T}{\partial x_j} d\Omega_1^e, \\
F_i &= \rho g_i \int_{\Omega_1^e} \Psi d\Omega_1^e - \frac{\mu}{\varepsilon^l} \int_{\Omega_1^e} \frac{\partial \Psi}{\partial x_i} f d\Omega_1^e + \mu \varepsilon^l k_{ij}^{-1} \int_{\Omega_1^e} \Psi \Psi^T \mathbf{V}_j^s d\Omega_1^e \\
&\quad + \frac{\mu}{\varepsilon^l} \int_{\Gamma_p^e} \Psi \frac{\partial \Psi^T}{\partial x_j} n_j d\Gamma_p^e \mathbf{V}_i - \int_{\Gamma_p^e} \Psi \Phi^T n_i d\Gamma_p^e \mathbf{P} + \frac{\mu}{\varepsilon^l} \int_{\Gamma_p^e} \Psi f n_i d\Gamma_p^e, \\
E &= \int_{\Omega_1^e} \Phi f d\Omega_1^e,
\end{aligned} \tag{3.30}$$

where  $i, j = 1, 2$ . The repeated index  $j$  indicates the summation over  $j, j = 1, 2$ . In Eq. (3.29), the term  $N$  is the nonlinear term. To handle this nonlinearity, an iterative approach such as the Newton's method is required.

To apply the Newton's method to the nonlinear term  $N$  in Eq. (3.29), we first rewrite the stiffness matrix, Eq. (3.29), into one equation. That is

$$\bar{K}(\bar{\mathbf{V}}) \bar{\mathbf{V}} = \bar{F}, \tag{3.31}$$

where  $\bar{K}(\bar{\mathbf{V}})$  represents the matrix in Eq. (3.29),  $\bar{\mathbf{V}}$  denotes the unknown vector and  $\bar{F}$  stands for the right-hand side vector in Eq. (3.29). Define

$$\mathbf{R}(\bar{\mathbf{V}}) = \bar{K}(\bar{\mathbf{V}}) \bar{\mathbf{V}} - \bar{F} = \mathbf{0}. \tag{3.32}$$

From Section 2.6, the approximation of  $\mathbf{R}$  can be expanded around the  $\bar{\mathbf{V}}^{(I)}$ . That is

$$\mathbf{R}(\bar{\mathbf{V}}) \approx \mathbf{R}(\bar{\mathbf{V}}^{(I)}) + \left. \frac{\partial \mathbf{R}}{\partial \bar{\mathbf{V}}} \right|_{\bar{\mathbf{V}}^{(I)}} \Delta \bar{\mathbf{V}}, \tag{3.33}$$

where  $\Delta \bar{\mathbf{V}} = \bar{\mathbf{V}} - \bar{\mathbf{V}}^{(I)}$  and  $\bar{\mathbf{V}}^{(I)}$  is the known vector. Substituting Eq. (3.33) into Eq. (3.32), we obtain

$$\mathbf{R}(\bar{\mathbf{V}}^{(I)}) + \left. \frac{\partial \mathbf{R}}{\partial \bar{\mathbf{V}}} \right|_{\bar{\mathbf{V}}^{(I)}} \Delta \bar{\mathbf{V}} = \mathbf{0}. \tag{3.34}$$

Updating  $\bar{\mathbf{V}}$  to be  $\bar{\mathbf{V}}^{(I+1)}$  and rearranging the Eq. (3.34), we have

$$\mathbf{R}(\bar{\mathbf{V}}^{(I)}) = - \left. \frac{\partial \mathbf{R}}{\partial \bar{\mathbf{V}}} \right|_{\bar{\mathbf{V}}^{(I)}} (\bar{\mathbf{V}}^{(I+1)} - \bar{\mathbf{V}}^{(I)}) \equiv -J(\bar{\mathbf{V}}^{(I)}) (\bar{\mathbf{V}}^{(I+1)} - \bar{\mathbf{V}}^{(I)}), \tag{3.35}$$

where

$$J = \left. \frac{\partial \mathbf{R}}{\partial \bar{\mathbf{V}}} \right|_{\bar{\mathbf{V}}^{(I)}} = \begin{bmatrix} \frac{\partial R_1}{\partial V_1} & \frac{\partial R_1}{\partial V_2} & \frac{\partial R_1}{\partial P} \\ \frac{\partial R_2}{\partial V_1} & \frac{\partial R_2}{\partial V_2} & \frac{\partial R_2}{\partial P} \\ \frac{\partial R_3}{\partial V_1} & \frac{\partial R_3}{\partial V_2} & \frac{\partial R_3}{\partial P} \end{bmatrix} \Bigg|_{\bar{\mathbf{V}}^{(I)}} \tag{3.36}$$

is the Jacobian matrix. To solve the unknown  $\bar{\mathbf{V}}^{(I+1)}$ , we rearrange Eq. (3.35). We have

$$\bar{\mathbf{V}}^{(I+1)} = \bar{\mathbf{V}}^{(I)} - J^{-1}(\bar{\mathbf{V}}^{(I)})\mathbf{R}(\bar{\mathbf{V}}^{(I)}). \quad (3.37)$$

In order to solve the unknown  $\bar{\mathbf{V}}^{(I+1)}$ , we provide the components of the vector  $\mathbf{R}$  as follows

$$\begin{aligned} R_1 &= \left( \frac{\rho}{(\varepsilon^l)^2} (C_1(\mathbf{V}_1) + C_2(\mathbf{V}_2)) + \frac{\mu}{\varepsilon^l} (K_{11} + K_{22}) + B_{11} \right) \mathbf{V}_1 + B_{12} \mathbf{V}_2 - Z_1^T \mathbf{P} - F_1, \\ R_2 &= B_{21} \mathbf{V}_1 + \left( \frac{\rho}{(\varepsilon^l)^2} (C_1(\mathbf{V}_1) + C_2(\mathbf{V}_2)) + \frac{\mu}{\varepsilon^l} (K_{11} + K_{22}) + B_{22} \right) \mathbf{V}_2 - Z_2^T \mathbf{P} - F_2, \\ R_3 &= Z_1 \mathbf{V}_1 + Z_2 \mathbf{V}_2 - E, \end{aligned} \quad (3.38)$$

and the components of the Jacobian matrix  $J$  are given by

$$\begin{aligned} \frac{\partial R_1}{\partial \mathbf{V}_1} &= \frac{\rho}{(\varepsilon^l)^2} (C_1(\mathbf{V}_1) + C_1(\mathbf{1})\mathbf{V}_1 + C_2(\mathbf{V}_2)) + \frac{\mu}{\varepsilon^l} (K_{11} + K_{22}) + B_{11}, \\ \frac{\partial R_1}{\partial \mathbf{V}_2} &= B_{12}, \\ \frac{\partial R_1}{\partial \mathbf{P}} &= -Z_1^T, \\ \frac{\partial R_2}{\partial \mathbf{V}_1} &= B_{21}, \\ \frac{\partial R_2}{\partial \mathbf{V}_2} &= \frac{\rho}{(\varepsilon^l)^2} (C_1(\mathbf{V}_1) + C_2(\mathbf{V}_2) + C_2(\mathbf{1})\mathbf{V}_2) + \frac{\mu}{\varepsilon^l} (K_{11} + K_{22}) + B_{22}, \\ \frac{\partial R_2}{\partial \mathbf{P}} &= -Z_2^T, \\ \frac{\partial R_3}{\partial \mathbf{V}_1} &= Z_1, \\ \frac{\partial R_3}{\partial \mathbf{V}_2} &= Z_2, \\ \frac{\partial R_3}{\partial \mathbf{P}} &= \mathbf{0}. \end{aligned} \quad (3.39)$$

Substituting Eqs. (3.38) - (3.39) into Eq. (3.37), we can compute the numerical results for the unknown  $\mathbf{V}^{(I+1)}$  defined in Eq. (3.37) within the domain  $\Omega_1$ . This iteration is repeated until  $\|\Delta \bar{\mathbf{V}}\|_2 < \text{tolerance}$ . So we obtain the final solution of the numerical approximation of the velocity and pressure within the domain  $\Omega_1$ .

### 3.1.2 The Steady-State Navier-Stokes Equation

In this section, we present the discretization of the steady-state Navier-Stokes equation applied in the domain  $\Omega_2$ . The governing equations for an incompressible Newtonian fluid are given by

$$\rho(\mathbf{v} \cdot \nabla \mathbf{v}) - \mu \Delta \mathbf{v} + \nabla p = \rho \mathbf{g}, \quad (3.40)$$

$$\nabla \cdot \mathbf{v} = 0. \quad (3.41)$$

For a two-dimensional domain, the equations can be expressed in indicial notation as

$$\rho v_j \frac{\partial v_i}{\partial x_j} - \mu \frac{\partial^2 v_i}{\partial x_j^2} + \frac{\partial p}{\partial x_i} = \rho g_i, \quad (3.42)$$

$$\text{This material is reserved for educational use only. } \frac{\partial v_i}{\partial x_j} = 0. \quad (3.43)$$

Forbidden to modify the content, and cite the document when use.

To derive the weak formulation, we multiply Eq. (3.42) by a weight function  $w$  and Eq. (3.43) by a weight function  $Q$ , and integrate over the domain  $\Omega_2$ . We have

$$\int_{\Omega_2} \left( \rho w v_j \frac{\partial v_i}{\partial x_j} - \mu w \frac{\partial^2 v_i}{\partial x_j^2} + w \frac{\partial p}{\partial x_i} \right) d\Omega_2 = \int_{\Omega_2} \rho g_i w d\Omega_2, \quad (3.44)$$

$$\int_{\Omega_2} Q \frac{\partial v_j}{\partial x_j} d\Omega_2 = 0. \quad (3.45)$$

Applying the Green's first identity to the second term of Eq. (3.44), we have

$$\begin{aligned} & \int_{\Omega_2} \left( \rho w v_j \frac{\partial v_i}{\partial x_j} + \mu \frac{\partial w}{\partial x_j} \frac{\partial v_i}{\partial x_j} - \frac{\partial w}{\partial x_i} p \right) d\Omega_2 \\ &= \int_{\Omega_2} \rho g_i w d\Omega_2 + \int_{\Gamma_f} \left( \mu w \frac{\partial v_i}{\partial x_j} n_j - w p n_i \right) d\Gamma_f, \end{aligned} \quad (3.46)$$

where  $\Gamma_f$  is the boundary of domain  $\Omega_2$ . Here, Eqs. (3.45) and (3.46) are referred to as the weak formulation of the steady-state Navier-Stokes equation. Let  $\Omega_2 = \bigcup \Omega_2^e$ , where  $\Omega_2^e$  indicates the element domain in  $\Omega_2$ . The integration over the domain  $\Omega_2$  can be written as summation of the integration over the element domain. Then, Eqs. (3.45) and (3.46) becomes

$$\sum_{e=1}^{N_e} \int_{\Omega_2^e} \left( \rho w v_j \frac{\partial v_i}{\partial x_j} + \mu \frac{\partial w}{\partial x_j} \frac{\partial v_i}{\partial x_j} - \frac{\partial w}{\partial x_i} p \right) d\Omega_2^e \quad (3.47)$$

$$= \sum_{e=1}^{N_e} \int_{\Omega_2^e} \rho g_i w d\Omega_2^e + \sum_{e=1}^{N_e} \int_{\Gamma_f^e} \left( \mu w \frac{\partial v_i}{\partial x_j} n_j - w p n_i \right) d\Gamma_f^e,$$

$$\sum_{e=1}^{N_e} \int_{\Omega_2^e} Q \frac{\partial v_j}{\partial x_j} d\Omega_2^e = 0. \quad (3.48)$$

To approximate the variables  $(v_i, p) \in V_h \times P_h$ , we substitute the approximations given in Eqs. (3.23) - (3.24) and (3.26) into Eqs. (3.47) and (3.48). The integration over each element is then expressed as follows

$$\rho \int_{\Omega_2^e} \Psi (\Psi^T \mathbf{V}_j) \frac{\partial \Psi^T}{\partial x_j} d\Omega_2^e \mathbf{V}_i + \mu \int_{\Omega_2^e} \frac{\partial \Psi}{\partial x_j} \frac{\partial \Psi^T}{\partial x_j} d\Omega_2^e \mathbf{V}_i - \int_{\Omega_2^e} \frac{\partial \Psi}{\partial x_i} \Phi^T d\Omega_2^e \mathbf{P} \quad (3.49)$$

$$= \rho g_i \int_{\Omega_2^e} \Psi d\Omega_2^e + \mu \int_{\Gamma_f^e} \Psi \frac{\partial \Psi^T}{\partial x_j} n_j d\Gamma_f^e \mathbf{V}_i - \int_{\Gamma_f^e} \Psi \Phi^T n_i d\Gamma_f^e \mathbf{P},$$

$$\int_{\Omega_2^e} \Phi \frac{\partial \Psi^T}{\partial x_j} d\Omega_2^e \mathbf{V}_j = 0. \quad (3.50)$$

Consequently, the matrix form of Eqs. (3.49) and (3.50) is

$$\begin{bmatrix} \tilde{N} + \tilde{A} & \mathbf{0} & -Z_1^T \\ \mathbf{0} & \tilde{N} + \tilde{A} & -Z_2^T \\ Z_1 & Z_2 & \mathbf{0} \end{bmatrix} \begin{Bmatrix} \mathbf{V}_1 \\ \mathbf{V}_2 \\ \mathbf{P} \end{Bmatrix} = \begin{Bmatrix} D_1 \\ D_2 \\ \mathbf{0} \end{Bmatrix}, \quad (3.51)$$

where the variable in the coefficient matrix are defined as

$$\begin{aligned} \tilde{N} &= \rho C_j(\mathbf{V}_j), \\ \tilde{A} &= \mu K_{jj}, \end{aligned} \quad (3.52)$$

$$D_i = \rho g_i \int_{\Omega_2^e} \Psi d\Omega_2^e + \mu \int_{\Gamma_f^e} \Psi \frac{\partial \Psi^T}{\partial x_j} n_j d\Gamma_f^e \mathbf{V}_i - \int_{\Gamma_f^e} \Psi \Phi^T n_i d\Gamma_f^e \mathbf{P}, i = 1, 2.$$

The nonlinear term in Eq. (3.51) is  $\tilde{N} = \rho C_j(\mathbf{V}_j)$ , which can be solved using the Newton's method.

To apply the Newton's method to Eq. (3.51), we first define the residual vector as

$$\mathbf{R}(\bar{\mathbf{V}}) = \tilde{K}(\bar{\mathbf{V}})\bar{\mathbf{V}} - \bar{D} = \mathbf{0}. \quad (3.53)$$

where  $\tilde{K}(\bar{\mathbf{V}})$  is the matrix in Eq. (3.51) and  $\bar{D}$  is the right-hand side vector. Then, we have the following iteration process to solve the nonlinear system

$$\bar{\mathbf{V}}^{(I+1)} = \bar{\mathbf{V}}^{(I)} - J^{-1}(\bar{\mathbf{V}}^{(I)})\mathbf{R}(\bar{\mathbf{V}}^{(I)}). \quad (3.54)$$

To solve the unknown  $\bar{\mathbf{V}}^{(I+1)}$ , we provide the components of the vector  $\mathbf{R}$  and the Jacobian matrix  $J$  as follows

$$\begin{aligned} R_1 &= (\rho(C_1(\mathbf{V}_1) + C_2(\mathbf{V}_2)) + \mu(K_{11} + K_{22}))\mathbf{V}_1 - Z_1^T \mathbf{P} - D_1, \\ R_2 &= (\rho(C_1(\mathbf{V}_1) + C_2(\mathbf{V}_2)) + \mu(K_{11} + K_{22}))\mathbf{V}_2 - Z_2^T \mathbf{P} - D_2, \\ R_3 &= Z_1 \mathbf{V}_1 + Z_2 \mathbf{V}_2, \end{aligned} \quad (3.55)$$

and

$$\begin{aligned} \frac{\partial R_1}{\partial \mathbf{V}_1} &= \rho(C_1(\mathbf{V}_1) + C_1(\mathbf{1})\mathbf{V}_1 + C_2(\mathbf{V}_2)) + \mu(K_{11} + K_{22}), \\ \frac{\partial R_1}{\partial \mathbf{V}_2} &= \mathbf{0}, \\ \frac{\partial R_1}{\partial \mathbf{P}} &= -Z_1^T, \\ \frac{\partial R_2}{\partial \mathbf{V}_1} &= \mathbf{0}, \\ \frac{\partial R_2}{\partial \mathbf{V}_2} &= \rho(C_1(\mathbf{V}_1) + C_2(\mathbf{V}_2) + C_2(\mathbf{1})\mathbf{V}_2) + \mu(K_{11} + K_{22}), \\ \frac{\partial R_2}{\partial \mathbf{P}} &= -Z_2^T, \\ \frac{\partial R_3}{\partial \mathbf{V}_1} &= Z_1, \\ \frac{\partial R_3}{\partial \mathbf{V}_2} &= Z_2, \\ \frac{\partial R_3}{\partial \mathbf{P}} &= \mathbf{0}. \end{aligned} \quad (3.56)$$

Substituting Eqs. (3.55) - (3.56) into Eq. (3.54), we can compute the numerical results for the unknown  $\bar{\mathbf{V}}^{(I+1)}$  in Eq. (3.54). This iterative process is repeated until  $\|\Delta \bar{\mathbf{V}}\|_2 <$  tolerance. Then we obtain the numerical approximation of the velocity and pressure within the domain  $\Omega_2$ .

### 3.1.3 The Stokes Equation

In this section, we present the discretization of the Stokes equations applied within domains  $\Omega_3$  and  $\Omega_4$ . We follow the same process as described in the previous section. However, the Newton's method is not applied here since the Stokes equation does not contain nonlinear terms. Therefore, the Stokes equations are as follows [43]

$$\nabla p - \mu \Delta \mathbf{v} = \rho \mathbf{g} \quad (3.57)$$

Forbidden to modify the content, and cite the document when use.

$$\nabla \mathbf{v} = \mathbf{0}. \quad (3.58)$$

For a two-dimensional domain, the equations can be expressed in index notation as

$$\frac{\partial p}{\partial x_i} - \mu \frac{\partial^2 v_i}{\partial x_j^2} = \rho g_i, \quad (3.59)$$

$$\frac{\partial v_j}{\partial x_j} = 0. \quad (3.60)$$

Let  $\Omega_a$  be  $\Omega_3$  or  $\Omega_4$ . To discretize the two-dimensional Stokes equation, we derive the weak formulation of the equation by multiplying Eq. (3.59) by the weight function  $w$  and Eq. (3.60) by the weight function  $Q$ , then integrate over domain  $\Omega_a$ , we have

$$\int_{\Omega_a} \left( w \frac{\partial p}{\partial x_i} - \mu w \frac{\partial^2 v_i}{\partial x_j^2} \right) d\Omega_a = \int_{\Omega_a} w \rho g_i d\Omega_a \quad (3.61)$$

$$\int_{\Omega_a} Q \frac{\partial v_j}{\partial x_j} d\Omega_a = 0, \quad (3.62)$$

Next, applying Green's first identity to the left-hand side of Eq. (3.61), we have

$$\int_{\Omega_a} \left( \mu \frac{\partial w}{\partial x_j} \frac{\partial v_i}{\partial x_j} - \frac{\partial w}{\partial x_i} p \right) d\Omega_a = \int_{\Omega_a} \rho g_i w d\Omega_a + \int_{\Gamma_a} \left( \mu w \frac{\partial v_i}{\partial x_j} n_j - w p n_i \right) d\Gamma_a, \quad (3.63)$$

where  $\Gamma_a$  is the boundary of the domain  $\Omega_a$ . Thus, Eqs. (3.62) and (3.63) represent the weak formulation of the Stokes equation. Let  $\Omega_a = \bigcup_e \Omega_a^e$  where  $\Omega_a^e$  is the element domain. Therefore, Eqs. (3.62) and (3.63) can be written as summation of the integration over the element domain, which gives

$$\sum_{e=1}^{N_e} \int_{\Omega_a^e} \left( \mu \frac{\partial w}{\partial x_j} \frac{\partial v_i}{\partial x_j} - \frac{\partial w}{\partial x_i} p \right) d\Omega_a^e = \sum_{e=1}^{N_e} \int_{\Omega_a^e} \rho g_i w d\Omega_a^e + \sum_{e=1}^{N_e} \int_{\Gamma_a^e} \left( \mu w \frac{\partial v_i}{\partial x_j} n_j - w p n_i \right) d\Gamma_a^e, \quad (3.64)$$

$$\sum_{e=1}^{N_e} \int_{\Omega_a^e} Q \frac{\partial v_j}{\partial x_j} d\Omega_a^e = 0. \quad (3.65)$$

Substituting the approximations (3.23) - (3.24) and (3.26) into Eqs. (3.64) and (3.65), we have the integration over each element is then expressed as follows

$$\mu \int_{\Omega_a^e} \frac{\partial \Psi}{\partial x_j} \frac{\partial \Psi^T}{\partial x_j} d\Omega_a^e \mathbf{V}_i - \int_{\Omega_a^e} \frac{\partial \Psi}{\partial x_i} \Phi^T d\Omega_a^e \mathbf{P} \quad (3.66)$$

$$= \rho g_i \int_{\Omega_a^e} \Psi d\Omega_a^e + \mu \int_{\Gamma_a^e} \Psi \frac{\partial \Psi^T}{\partial x_j} n_j d\Gamma_a^e \mathbf{V}_i - \int_{\Gamma_a^e} \Psi \Phi^T n_i d\Gamma_a^e \mathbf{P},$$

$$\int_{\Omega_a^e} \Phi \frac{\partial \Psi^T}{\partial x_j} d\Omega_a^e \mathbf{V}_j = 0. \quad (3.67)$$

Then, Eqs. (3.66) and (3.67) can be written in the following matrix form

$$\begin{bmatrix} \tilde{A} & \mathbf{0} & -Z_1^T \\ \mathbf{0} & \tilde{A} & -Z_2^T \\ Z_1 & Z_2 & \mathbf{0} \end{bmatrix} \begin{Bmatrix} \mathbf{V}_1 \\ \mathbf{V}_2 \\ \mathbf{P} \end{Bmatrix} = \begin{Bmatrix} \tilde{D}_1 \\ \tilde{D}_2 \\ \mathbf{0} \end{Bmatrix}, \quad (3.68)$$

where

$$\tilde{D}_i = \rho g_i \int_{\Omega_a^e} \Psi d\Omega_a^e + \mu \int_{\Gamma_a^e} \Psi \frac{\partial \Psi^T}{\partial x_j} n_j d\Gamma_a^e \mathbf{V}_i - \int_{\Gamma_a^e} \Psi \Phi^T n_i d\Gamma_a^e \mathbf{P}, \quad i = 1, 2. \quad (3.69)$$

We now have the element matrix for both domains  $\Omega_3$  and  $\Omega_4$ , allowing us to compute the numerical results for fluid flow within these domains.

## 3.2 Boundary Conditions

In this section, we present the boundary conditions applied in this work. The boundary conditions used to compute the velocity of the PCL fluid in  $\Omega_1$  and  $\Omega_2$  are presented in Section 3.2.1. The boundary conditions used to find the fluid velocities in  $\Omega_3$  and  $\Omega_4$  are provided in Section 3.2.2.

### 3.2.1 Boundary Condition for the PCL

Figure 3.1(a) shows the boundaries  $\Gamma_i$ ,  $i = 1, 2, 3, 4$  when the cilia are perpendicular to the horizontal plane, while Figure 3.1(b) illustrates the boundaries  $\Gamma_i$ ,  $i = 1, 2, \dots, 7$  when the cilia make an angle  $\theta$  less than  $90^\circ$  to the horizontal plane. The variable  $y_s$  represents the dimensionless height of the porous medium. For the boundary conditions used in the PCL, we first assume that there is no velocity at the ciliary rootlets in domain  $\Omega_1$ . That is the velocity of the PCL fluid is zero at  $\Gamma_1$  in both Figure 3.1(a) and (b). The rate of change of velocities with respect to  $x_2$  is zero at the top of the domain  $\Omega_2$  and also at  $\Gamma_4$  in Figure 3.1(a). The velocity is continuous at  $\Gamma_4$  in Figure 3.1(b). At  $\Gamma_7$ , the rate of change of velocities with respect to  $x_2$  is zero, meaning the maximum magnitudes of  $v_1$  and  $v_2$  occur at  $\Gamma_7$ . Thus, the boundary conditions are summarized as follows.

$$\begin{aligned}
 v_i &= 0, \quad \text{for } i = 1, 2, \text{ at } \Gamma_1, \\
 \frac{\partial v_i}{\partial x_2} &= 0, \quad \text{for } i = 1, 2, \text{ at } \Gamma_4, \\
 \frac{\partial v_1}{\partial x_2} &= 0, \quad \text{at } \Gamma_4 \text{ in Figure 3.1(a)}, \\
 v_2 &= 0, \quad \text{at } \Gamma_4 \text{ in Figure 3.1(a)}.
 \end{aligned} \tag{3.70}$$

Here, at the boundaries  $\Gamma_2, \Gamma_3, \Gamma_5$  and  $\Gamma_6$ , the velocities are assumed to be unknown.

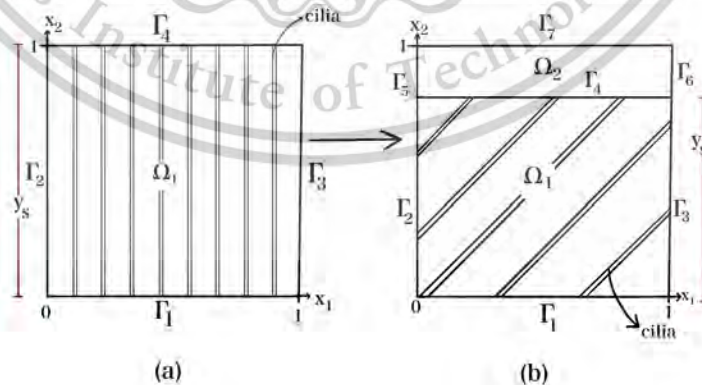


**Figure 3.1:** Numerical domains and boundaries of the problem. (a) The cilia are perpendicular to the horizontal plane. (b) The cilia make angle  $\theta$  less than  $90^\circ$  to the horizontal plane.

To apply these boundaries in the domains  $\Omega_1$  and  $\Omega_2$ , we first focus on the boundaries in domain  $\Omega_1$ , which are located at  $\Gamma_1 - \Gamma_4$ , as shown in Figure 3.1. The

boundary terms in Eq. (3.20) are given by

$$\int_{\Gamma_p^e} \left[ \frac{\mu}{\varepsilon^l} w \left( w \frac{\partial v_i}{\partial x_j} n_j \right) - w p n_i + \frac{\mu}{\varepsilon^l} w f n_i \right] d\Gamma_p^e. \quad (3.71)$$

For  $i = 1$ , we obtain

$$\int_{\Gamma_p^e} \left[ \frac{\mu}{\varepsilon^l} w \left( \frac{\partial v_1}{\partial x_1} n_1 + \frac{\partial v_1}{\partial x_2} n_2 \right) - w p n_1 + \frac{\mu}{\varepsilon^l} w f n_1 \right] d\Gamma_p^e. \quad (3.72)$$

For  $i = 2$ , we obtain

$$\int_{\Gamma_p^e} \left[ \frac{\mu}{\varepsilon^l} w \left( \frac{\partial v_2}{\partial x_1} n_1 + \frac{\partial v_2}{\partial x_2} n_2 \right) - w p n_2 + \frac{\mu}{\varepsilon^l} w f n_2 \right] d\Gamma_p^e. \quad (3.73)$$

Here, we define

$$\Gamma_p = \Gamma_1 \cup \Gamma_2 \cup \Gamma_3 \cup \Gamma_4, \quad (3.74)$$

(see Figure 3.1). The outward unit normal vector  $n_1$  and  $n_2$  at  $\Gamma_1, \Gamma_2, \Gamma_3$  and  $\Gamma_4$  are given by

$$\mathbf{n} = (n_1, n_2) = \begin{cases} (0, -1), & \text{on } \Gamma_1, \\ (-1, 0), & \text{on } \Gamma_2, \\ (1, 0), & \text{on } \Gamma_3, \\ (0, 1), & \text{on } \Gamma_4. \end{cases} \quad (3.75)$$

Therefore, at each boundary, we apply the boundary conditions to Eqs. (3.72) and (3.73). Therefore, at  $\Gamma_1$ :

$$\int_{\Gamma_1^e} \left[ \frac{\mu}{\varepsilon^l} w \left( \frac{\partial v_1}{\partial x_1} n_1 + \frac{\partial v_1}{\partial x_2} n_2 \right) - w p n_1 + \frac{\mu}{\varepsilon^l} w f n_1 \right] d\Gamma_1^e = 0, \quad (3.76)$$

$$\int_{\Gamma_1^e} \left[ \frac{\mu}{\varepsilon^l} w \left( \frac{\partial v_2}{\partial x_1} n_1 + \frac{\partial v_2}{\partial x_2} n_2 \right) - w p n_2 + \frac{\mu}{\varepsilon^l} w f n_2 \right] d\Gamma_1^e = \int_{\Gamma_1^e} \left( w p - \frac{\mu}{\varepsilon^l} w f \right) d\Gamma_1^e. \quad (3.77)$$

At  $\Gamma_2$ :

$$\int_{\Gamma_2^e} \left[ \frac{\mu}{\varepsilon^l} w \left( \frac{\partial v_1}{\partial x_1} n_1 + \frac{\partial v_1}{\partial x_2} n_2 \right) - w p n_1 + \frac{\mu}{\varepsilon^l} w f n_1 \right] d\Gamma_2^e = - \int_{\Gamma_2^e} \left( \frac{\mu}{\varepsilon^l} w \frac{\partial v_1}{\partial x_1} - w p + \frac{\mu}{\varepsilon^l} w f \right) d\Gamma_2^e, \quad (3.78)$$

$$\int_{\Gamma_2^e} \left[ \frac{\mu}{\varepsilon^l} w \left( \frac{\partial v_2}{\partial x_1} n_1 + \frac{\partial v_2}{\partial x_2} n_2 \right) - w p n_2 + \frac{\mu}{\varepsilon^l} w f n_2 \right] d\Gamma_2^e = - \int_{\Gamma_2^e} \left( \frac{\mu}{\varepsilon^l} w \frac{\partial v_2}{\partial x_1} \right) d\Gamma_2^e. \quad (3.79)$$

At  $\Gamma_3$ :

$$\int_{\Gamma_3^e} \left[ \frac{\mu}{\varepsilon^l} w \left( \frac{\partial v_1}{\partial x_1} n_1 + \frac{\partial v_1}{\partial x_2} n_2 \right) - w p n_1 + \frac{\mu}{\varepsilon^l} w f n_1 \right] d\Gamma_3^e = \int_{\Gamma_3^e} \left( \frac{\mu}{\varepsilon^l} w \frac{\partial v_1}{\partial x_1} - w p + \frac{\mu}{\varepsilon^l} w f \right) d\Gamma_3^e, \quad (3.80)$$

$$\int_{\Gamma_3^e} \left[ \frac{\mu}{\varepsilon^l} w \left( \frac{\partial v_2}{\partial x_1} n_1 + \frac{\partial v_2}{\partial x_2} n_2 \right) - w p n_2 + \frac{\mu}{\varepsilon^l} w f n_2 \right] d\Gamma_3^e = \int_{\Gamma_3^e} \frac{\mu}{\varepsilon^l} w \frac{\partial v_2}{\partial x_1} d\Gamma_3^e. \quad (3.81)$$

At  $\Gamma_4$ , for the case where cilia make angle  $\theta = 90^\circ$ :

$$\int_{\Gamma_4^e} \left[ \frac{\mu}{\varepsilon^l} w \left( \frac{\partial v_1}{\partial x_1} n_1 + \frac{\partial v_1}{\partial x_2} n_2 \right) - w p n_1 + \frac{\mu}{\varepsilon^l} w f n_1 \right] d\Gamma_4^e = 0, \quad (3.82)$$

$$\int_{\Gamma_4^e} \left[ \frac{\mu}{\varepsilon^l} w \left( \frac{\partial v_2}{\partial x_1} n_1 + \frac{\partial v_2}{\partial x_2} n_2 \right) - w p n_2 + \frac{\mu}{\varepsilon^l} w f n_2 \right] d\Gamma_4^e = \int_{\Gamma_4^e} \left( w p - \frac{\mu}{\varepsilon^l} w f \right) d\Gamma_4^e. \quad (3.83)$$

Forbidden to modify the content, and cite the document when use.

At  $\Gamma_4$ , for the case where cilia make angle  $\theta < 90^\circ$ :

$$\int_{\Gamma_4^e} \left[ \frac{\mu}{\varepsilon^l} w \left( \frac{\partial v_1}{\partial x_1} n_1 + \frac{\partial v_1}{\partial x_2} n_2 \right) - w p n_1 + \frac{\mu}{\varepsilon^l} w f n_1 \right] d\Gamma_4^e = \int_{\Gamma_4^e} \frac{\mu}{\varepsilon^l} w \frac{\partial v_1}{\partial x_2} d\Gamma_4^e, \quad (3.84)$$

$$\int_{\Gamma_4^e} \left[ \frac{\mu}{\varepsilon^l} w \left( \frac{\partial v_2}{\partial x_1} n_1 + \frac{\partial v_2}{\partial x_2} n_2 \right) - w p n_2 + \frac{\mu}{\varepsilon^l} w f n_2 \right] d\Gamma_4^e = \int_{\Gamma_4^e} \left( \frac{\mu}{\varepsilon^l} w \frac{\partial v_2}{\partial x_2} - w p + \frac{\mu}{\varepsilon^l} w f \right) d\Gamma_4^e. \quad (3.85)$$

Now, we can apply the boundary conditions given in Eqs. (3.76) – (3.85) to Eq. (3.29). Note that the terms involving  $v_1, v_2$  and  $p$  can be moved to the left-hand side to be incorporated into the matrix in Eq. (3.29).

Next, we consider the boundary conditions in domain  $\Omega_2$ , focusing on the boundaries  $\Gamma_4 - \Gamma_7$ . The domain  $\Omega_2$  appears when cilia make the angle  $\theta < 90^\circ$  (see Figure 3.1(b)). For each element, we examine the boundary terms in Eq. (3.47), given by

$$\int_{\Gamma_f^e} \left( \mu w \frac{\partial v_i}{\partial x_j} n_j - w p n_i \right) d\Gamma_f^e \quad (3.86)$$

For  $i = 1$ , we obtain

$$\int_{\Gamma_f^e} \left[ \mu w \left( \frac{\partial v_1}{\partial x_1} n_1 + \frac{\partial v_1}{\partial x_2} n_2 \right) - w p n_1 \right] d\Gamma_f^e. \quad (3.87)$$

For  $i = 2$ , we obtain

$$\int_{\Gamma_f^e} \left[ \mu w \left( \frac{\partial v_2}{\partial x_1} n_1 + \frac{\partial v_2}{\partial x_2} n_2 \right) - w p n_2 \right] d\Gamma_f^e. \quad (3.88)$$

We define

$$\Gamma_f = \Gamma_4 \cup \Gamma_5 \cup \Gamma_6 \cup \Gamma_7, \quad (3.89)$$

(see Figure 3.1(b)). The outward unit normal vector  $n_1$  and  $n_2$  at  $\Gamma_4, \Gamma_5, \Gamma_6$  and  $\Gamma_7$  are given by

$$\mathbf{n} = (n_1, n_2) = \begin{cases} (0, -1), & \text{on } \Gamma_4, \\ (-1, 0), & \text{on } \Gamma_5, \\ (1, 0), & \text{on } \Gamma_6, \\ (0, 1), & \text{on } \Gamma_7. \end{cases} \quad (3.90)$$

Therefore, at each boundary, we apply the boundary conditions to Eqs. (3.87) and (3.88). Therefore, at  $\Gamma_4$ :

$$\int_{\Gamma_4^e} \left[ \mu w \left( \frac{\partial v_1}{\partial x_1} n_1 + \frac{\partial v_1}{\partial x_2} n_2 \right) - w p n_1 \right] d\Gamma_4^e = - \int_{\Gamma_4^e} \mu w \frac{\partial v_1}{\partial x_2} d\Gamma_4^e, \quad (3.91)$$

$$\int_{\Gamma_4^e} \left[ \mu w \left( \frac{\partial v_2}{\partial x_1} n_1 + \frac{\partial v_2}{\partial x_2} n_2 \right) - w p n_2 \right] d\Gamma_4^e = - \int_{\Gamma_4^e} \left( \mu w \frac{\partial v_2}{\partial x_2} - w p \right) d\Gamma_4^e. \quad (3.92)$$

At  $\Gamma_5$ :

$$\int_{\Gamma_5^e} \left[ \mu w \left( \frac{\partial v_1}{\partial x_1} n_1 + \frac{\partial v_1}{\partial x_2} n_2 \right) - w p n_1 \right] d\Gamma_5^e = - \int_{\Gamma_5^e} \left( \mu w \frac{\partial v_1}{\partial x_1} - w p \right) d\Gamma_5^e, \quad (3.93)$$

$$\int_{\Gamma_5^e} \left[ \mu w \left( \frac{\partial v_2}{\partial x_1} n_1 + \frac{\partial v_2}{\partial x_2} n_2 \right) - w p n_2 \right] d\Gamma_5^e = - \int_{\Gamma_5^e} \mu w \frac{\partial v_2}{\partial x_1} d\Gamma_5^e. \quad (3.94)$$

At  $\Gamma_6$ :

$$\int_{\Gamma_6^e} \left[ \mu w \left( \frac{\partial v_1}{\partial x_1} n_1 + \frac{\partial v_1}{\partial x_2} n_2 \right) - w p n_1 \right] d\Gamma_6^e = \int_{\Gamma_6^e} \left( \mu w \frac{\partial v_1}{\partial x_1} - w p \right) d\Gamma_6^e, \quad (3.95)$$

$$\int_{\Gamma_6^e} \left[ \mu w \left( \frac{\partial v_2}{\partial x_1} n_1 + \frac{\partial v_2}{\partial x_2} n_2 \right) - w p n_2 \right] d\Gamma_6^e = \int_{\Gamma_6^e} \mu w \frac{\partial v_2}{\partial x_1} d\Gamma_6^e. \quad (3.96)$$

At  $\Gamma_7$ :

$$\int_{\Gamma_7^e} \left[ \mu w \left( \frac{\partial v_1}{\partial x_1} n_1 + \frac{\partial v_1}{\partial x_2} n_2 \right) - w p n_1 \right] d\Gamma_7^e = 0, \quad (3.97)$$

$$\int_{\Gamma_7^e} \left[ \mu w \left( \frac{\partial v_2}{\partial x_1} n_1 + \frac{\partial v_2}{\partial x_2} n_2 \right) - w p n_2 \right] d\Gamma_7^e = - \int_{\Gamma_7^e} w p d\Gamma_7^e. \quad (3.98)$$

Now, we can apply the boundary conditions given in Eqs. (3.91) – (3.98) to Eq. (3.51).

It is important to note that  $\Gamma_4$  is the interface between the domains  $\Omega_1$  and  $\Omega_2$ , serving as the interface between the porous and free-fluid regions. In this work, we assume that the velocity is continuous at  $\Gamma_4$ , i.e., there is no jump in velocity across the interface. So, we use the outward unit normal vectors at the element boundaries. This leads to the cancellation of certain boundary integrals over  $\Gamma_4$ . However, since different governing equations are used in different domains, not all integration terms at  $\Gamma_4$  can be canceled.

### 3.2.2 Boundary Condition for the Free-Fluid Region and the Mucus Layer

For the boundary conditions used in the free-fluid region ( $\Omega_3$ ) and the ML ( $\Omega_4$ ), we assume that the bottom boundary is located at the tips of the cilia when the cilia make angles with the horizontal plane  $\theta = 90^\circ, 80^\circ, 70^\circ, 60^\circ$  and  $50^\circ$  in one fixed domain. Figure 3.2 displays boundaries used in domain  $\Omega_3$  and  $\Omega_4$ . The variable  $y_{ML}$  denotes the  $x_2$ -coordinate at the top of domain  $\Omega_4$ , while the dimensionless  $y_{PCL}$  represents the cilia length in the perpendicular case, set to 1. Similarly, the dimensionless of  $y_{ML}$  is set to 2. The variable  $y_{in}$  represents the interface between the porous medium and the free-fluid region for each angle. For example,  $y_{in}(70^\circ)$  denotes the interface at  $70^\circ$ . Here, we assume cilia bend downward from  $\theta = 90^\circ$  to  $50^\circ$ , decreasing by  $10^\circ$  every 0.2 increment along the  $x_1$ -axis. These angle ranges correspond to  $x_1 = 0$  to  $x_1 = 1$ , divided into intervals of 0.2 each. At  $\theta = 40^\circ$ , the cilia are assumed to stop beating [32]. In this study, we assume the velocity is continuous at the interface ( $\Gamma_9$ ) between the free-fluid region and the ML.

Thus, the boundary conditions in domain  $\Omega_3$  are defined as follows

$$v_i(x_1, y_{in}) = v_{i_{in}} \quad \text{at } \Gamma_8, \quad (3.99)$$

where  $v_{1_{in}}$  and  $v_{2_{in}}$  represent the velocities of the PCL fluid in  $x_1$ - and  $x_2$ - directions, respectively, as obtained from [41]. Note that  $x_2$  value corresponds to  $y_{in}$  for each angle. To consider the ML boundary, we use the velocity of the PCL fluid obtained from domain  $\Omega_3$  as the boundary condition at the bottom of domain  $\Omega_4$  (at  $\Gamma_9$ ) for

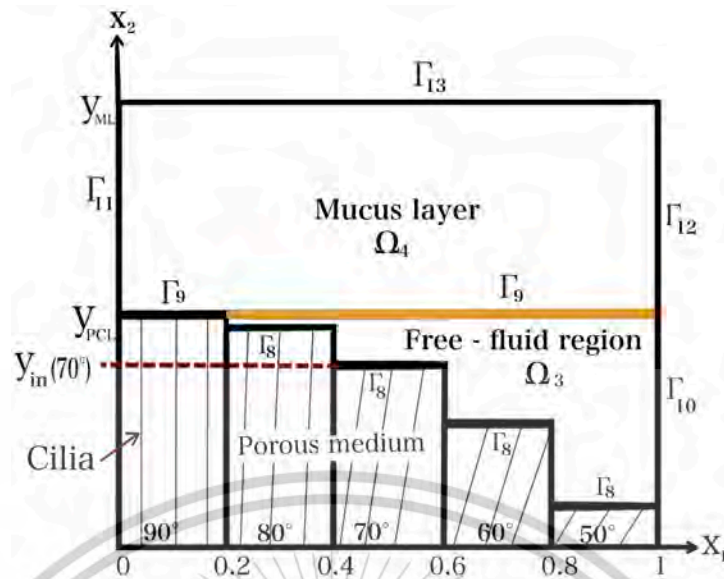


Figure 3.2: Numerical domains and boundaries of the domains  $\Omega_3$  and  $\Omega_4$ .

angle  $\theta < 90^\circ$ , while the velocity of the PCL fluid at  $x_2 = y_{in}(90^\circ)$  is obtained from [41]. At the boundary  $\Gamma_{13}$ , we assume that

$$\frac{\partial v_i}{\partial x_2} = 0. \quad (3.100)$$

The boundaries  $\Gamma_{10}$ ,  $\Gamma_{11}$  and  $\Gamma_{12}$  are assumed to be unknown.

To apply the boundary conditions Eqs. (3.99) - (3.100) to Eq. (3.68), we express the integration over boundary in Eq. (3.64) as follows,

$$\int_{\Gamma_a^e} \left( \mu w \frac{\partial v_i}{\partial x_j} n_j - w p n_i \right) d\Gamma_a^e. \quad (3.101)$$

For  $i = 1$ , we obtain

$$\int_{\Gamma_a^e} \left[ \mu w \left( \frac{\partial v_1}{\partial x_1} n_1 + \frac{\partial v_1}{\partial x_2} n_2 \right) - w p n_1 \right] d\Gamma_a^e. \quad (3.102)$$

For  $i = 2$ , we obtain

$$\int_{\Gamma_a^e} \left[ \mu w \left( \frac{\partial v_2}{\partial x_1} n_1 + \frac{\partial v_2}{\partial x_2} n_2 \right) - w p n_2 \right] d\Gamma_a^e. \quad (3.103)$$

These equations can be used for both domains  $\Omega_3$  and  $\Omega_4$ . We now focus on the domain  $\Omega_3$ , which is bounded by three segments:  $\Gamma_8$ ,  $\Gamma_9$  and  $\Gamma_{10}$ . The boundary  $\Gamma_a$  for the domain  $\Omega_3$  can be expressed as

$$\Gamma_a = \Gamma_8 \cup \Gamma_9 \cup \Gamma_{10}. \quad (3.104)$$

The outward unit normal vector  $n_1$  and  $n_2$  at  $\Gamma_8$ ,  $\Gamma_9$  and  $\Gamma_{10}$  are given by

$$\mathbf{n} = (n_1, n_2) = \begin{cases} (0, -1), & \text{on the horizontal segment of } \Gamma_8, \\ (-1, 0), & \text{on the vertical segment of } \Gamma_8, \\ (0, 1), & \text{on } \Gamma_9, \\ (1, 0), & \text{on } \Gamma_{10}. \end{cases} \quad (3.105)$$

This material is reserved for educational use only, not allowed for commercial use.

Forbidden to modify the content, and cite the document when use.

We apply the boundary conditions to Eq. (3.102) and (3.103). Therefore, at the horizontal segment of  $\Gamma_8$ :

$$\int_{\Gamma_8^e} \left[ \mu w \left( \frac{\partial v_1}{\partial x_1} n_1 + \frac{\partial v_1}{\partial x_2} n_2 \right) - w p n_1 \right] d\Gamma_8^e = 0, \quad (3.106)$$

$$\int_{\Gamma_8^e} \left[ \mu w \left( \frac{\partial v_2}{\partial x_1} n_1 + \frac{\partial v_2}{\partial x_2} n_2 \right) - w p n_2 \right] d\Gamma_8^e = \int_{\Gamma_8^e} w p d\Gamma_8^e. \quad (3.107)$$

At the vertical segment of  $\Gamma_8$ :

$$\int_{\Gamma_8^e} \left[ \mu w \left( \frac{\partial v_1}{\partial x_1} n_1 + \frac{\partial v_1}{\partial x_2} n_2 \right) - w p n_1 \right] d\Gamma_8^e = \int_{\Gamma_8^e} w p d\Gamma_8^e, \quad (3.108)$$

$$\int_{\Gamma_8^e} \left[ \mu w \left( \frac{\partial v_2}{\partial x_1} n_1 + \frac{\partial v_2}{\partial x_2} n_2 \right) - w p n_2 \right] d\Gamma_8^e = 0. \quad (3.109)$$

At  $\Gamma_9$ :

$$\int_{\Gamma_9^e} \left[ \mu w \left( \frac{\partial v_1}{\partial x_1} n_1 + \frac{\partial v_1}{\partial x_2} n_2 \right) - w p n_1 \right] d\Gamma_9^e = \int_{\Gamma_9^e} \mu w \frac{\partial v_1}{\partial x_2} d\Gamma_9^e, \quad (3.110)$$

$$\int_{\Gamma_9^e} \left[ \mu w \left( \frac{\partial v_2}{\partial x_1} n_1 + \frac{\partial v_2}{\partial x_2} n_2 \right) - w p n_2 \right] d\Gamma_9^e = \int_{\Gamma_9^e} \left( \mu w \frac{\partial v_2}{\partial x_2} - w p \right) d\Gamma_9^e. \quad (3.111)$$

At  $\Gamma_{10}$ :

$$\int_{\Gamma_{10}^e} \left[ \mu w \left( \frac{\partial v_1}{\partial x_1} n_1 + \frac{\partial v_1}{\partial x_2} n_2 \right) - w p n_1 \right] d\Gamma_{10}^e = \int_{\Gamma_{10}^e} \left( \mu w \frac{\partial v_1}{\partial x_1} - w p \right) d\Gamma_{10}^e, \quad (3.112)$$

$$\int_{\Gamma_{10}^e} \left[ \mu w \left( \frac{\partial v_2}{\partial x_1} n_1 + \frac{\partial v_2}{\partial x_2} n_2 \right) - w p n_2 \right] d\Gamma_{10}^e = \int_{\Gamma_{10}^e} \mu w \frac{\partial v_2}{\partial x_1} d\Gamma_{10}^e. \quad (3.113)$$

Now, we can apply the boundary conditions given in Eqs. (3.106) - (3.113) to Eq. (3.68).

Next, we consider the boundary  $\Gamma_a$  in the domain  $\Omega_4$ . For this domain, the boundary  $\Gamma_a$  is defined as

$$\Gamma_a = \Gamma_9 \cup \Gamma_{11} \cup \Gamma_{12} \cup \Gamma_{13}. \quad (3.114)$$

The outward unit normal vector for  $\Gamma_9, \Gamma_{11}, \Gamma_{12}$  and  $\Gamma_{13}$  are given by

$$\mathbf{n} = (n_1, n_2) = \begin{cases} (0, -1), & \text{on } \Gamma_9, \\ (-1, 0), & \text{on } \Gamma_{11}, \\ (1, 0), & \text{on } \Gamma_{12}, \\ (0, 1), & \text{on } \Gamma_{13}. \end{cases} \quad (3.115)$$

We apply the boundary conditions to Eqs. (3.102) - (3.103). Therefore, at  $\Gamma_9$ :

$$\int_{\Gamma_9^e} \left[ \mu w \left( \frac{\partial v_1}{\partial x_1} n_1 + \frac{\partial v_1}{\partial x_2} n_2 \right) - w p n_1 \right] d\Gamma_9^e = 0, \quad (3.116)$$

$$\int_{\Gamma_9^e} \left[ \mu w \left( \frac{\partial v_2}{\partial x_1} n_1 + \frac{\partial v_2}{\partial x_2} n_2 \right) - w p n_2 \right] d\Gamma_9^e = \int_{\Gamma_9^e} w p d\Gamma_9^e. \quad (3.117)$$

At  $\Gamma_{11}$ :

$$\int_{\Gamma_{11}^e} \left[ \mu w \left( \frac{\partial v_1}{\partial x_1} n_1 + \frac{\partial v_1}{\partial x_2} n_2 \right) - w p n_1 \right] d\Gamma_{11}^e = - \int_{\Gamma_{11}^e} \left( \mu w \frac{\partial v_1}{\partial x_1} - w p \right) d\Gamma_{11}^e, \quad (3.118)$$

$$\int_{\Gamma_{11}^e} \left[ \mu w \left( \frac{\partial v_2}{\partial x_1} n_1 + \frac{\partial v_2}{\partial x_2} n_2 \right) - w p n_2 \right] d\Gamma_{11}^e = - \int_{\Gamma_{11}^e} \mu w \frac{\partial v_2}{\partial x_1} d\Gamma_{11}^e. \quad (3.119)$$

At  $\Gamma_{12}$ :

$$\int_{\Gamma_{12}^e} \left[ \mu w \left( \frac{\partial v_1}{\partial x_1} n_1 + \frac{\partial v_1}{\partial x_2} n_2 \right) - w p n_1 \right] d\Gamma_{12}^e = \int_{\Gamma_{12}^e} \left( \mu w \frac{\partial v_1}{\partial x_1} - w p \right) d\Gamma_{12}^e, \quad (3.120)$$

$$\int_{\Gamma_{12}^e} \left[ \mu w \left( \frac{\partial v_2}{\partial x_1} n_1 + \frac{\partial v_2}{\partial x_2} n_2 \right) - w p n_2 \right] d\Gamma_{12}^e = \int_{\Gamma_{12}^e} \mu w \frac{\partial v_2}{\partial x_1} d\Gamma_{12}^e. \quad (3.121)$$

At  $\Gamma_{13}$ :

$$\int_{\Gamma_{13}^e} \left[ \mu w \left( \frac{\partial v_1}{\partial x_1} n_1 + \frac{\partial v_1}{\partial x_2} n_2 \right) - w p n_1 \right] d\Gamma_{13}^e = 0, \quad (3.122)$$

$$\int_{\Gamma_{13}^e} \left[ \mu w \left( \frac{\partial v_2}{\partial x_1} n_1 + \frac{\partial v_2}{\partial x_2} n_2 \right) - w p n_2 \right] d\Gamma_{13}^e = - \int_{\Gamma_{13}^e} w p d\Gamma_{13}^e. \quad (3.123)$$

Now, we can apply the boundary conditions given in Eqs. (3.116) - (3.123) to Eq. (3.68).



## Chapter 4

# Numerical Results

In this chapter, we present the velocities of the PCL fluid and mucus, obtained using a computer program to solve our governing equations. To validate our results, we provide the exact solution of the Brinkman equation in Section 4.1, and we compare our numerical solution with the exact results in Section 4.2. The numerical solutions of the nonlinear Brinkman equation, as well as the steady-state Navier-Stokes and Stokes equations, are presented in Section 4.3.

### 4.1 Exact Solution

To verify the accuracy of our code in this section, we present an analytical solution of the one-dimensional Brinkman equation, Eq. (3.1), when the nonlinear, cilia velocity, and gravitational terms are omitted. This analytical solution is used to compare with the numerical results. The simplified one-dimensional form of Eq. (3.1) can be expressed as

$$\frac{\mu}{\varepsilon^l} \frac{d^2 v}{dx_2^2} - \mu k^{-1} v = \frac{dp}{dx_1}, \quad (4.1)$$

where  $\frac{dp}{dx_1}$  is a constant. The boundary conditions are

$$v(L_m) = v_L \text{ and } v(0) = 0. \quad (4.2)$$

where  $L_m$  and  $v_L$  are constants. To derive the analytical solution that satisfies the given boundary conditions, the homogeneous form of Eq. (4.1) is

$$\frac{\mu}{\varepsilon^l} \frac{d^2 v}{dx_2^2} - \mu k^{-1} v = 0. \quad (4.3)$$

Hence, the general solution of Eq. 4.3 is given by

$$v_c(x_2) = c_1 e^{x_2 \sqrt{\varepsilon^l k^{-1}}} + c_2 e^{-x_2 \sqrt{\varepsilon^l k^{-1}}}, \quad (4.4)$$

where  $c_1$  and  $c_2$  are arbitrary constants. Next, we determine the particular solution  $v_p$ . Since the right-hand side of Eq. (4.1) is constant, we assume a constant particular solution of the form

$$v_p = A_p, \quad (4.5)$$

where  $A_p$  is a constant. Then, the first and second derivatives are

$$v'_p = 0 \text{ and } v''_p = 0. \quad (4.6)$$

Substituting Eqs.(4.5) and (4.6) into Eq. (4.1), we obtain

This material is reserved for educational use only, not allowed for commercial use.

$$-\mu k^{-1} A_p = \frac{dp}{dx_1}. \quad (4.7)$$

Forbidden to modify the content, and cite the document when use.

Rearranging Eq. (4.7), we have

$$A_p = -\frac{1}{\mu k^{-1}} \frac{dp}{dx_1}. \quad (4.8)$$

Thus, the particular solution becomes

$$v_p = -\frac{1}{\mu k^{-1}} \frac{dp}{dx_1}. \quad (4.9)$$

Therefore, the general solution is the sum of the complementary and particular solutions, given by

$$v(x_2) = c_1 e^{x_2 \sqrt{\varepsilon^l k^{-1}}} + c_2 e^{-x_2 \sqrt{\varepsilon^l k^{-1}}} - \frac{1}{\mu k^{-1}} \frac{dp}{dx_1}. \quad (4.10)$$

To find the value of  $c_1$  and  $c_2$ , we apply the boundary conditions, Eq. (4.2), to the general solution, Eq. (4.10). With  $v(0) = 0$ , we have

$$0 = v(0) = c_1 e^{0 \sqrt{\varepsilon^l k^{-1}}} + c_2 e^{0 \sqrt{\varepsilon^l k^{-1}}} - \frac{1}{\mu k^{-1}} \frac{dp}{dx_1}. \quad (4.11)$$

Eq. (4.11) is simplified to

$$c_1 = -c_2 + \frac{1}{\mu k^{-1}} \frac{dp}{dx_1}. \quad (4.12)$$

Next, applying the second boundary condition  $v(L_m) = v_L$ , we have

$$v_L = v(L_m) = c_1 e^{L_m \sqrt{\varepsilon^l k^{-1}}} + c_2 e^{-L_m \sqrt{\varepsilon^l k^{-1}}} - \frac{1}{\mu k^{-1}} \frac{dp}{dx_1}. \quad (4.13)$$

Substituting Eq. (4.12) into Eq. (4.13), we have

$$v_L = \left( -c_2 + \frac{1}{\mu k^{-1}} \frac{dp}{dx_1} \right) e^{L_m \sqrt{\varepsilon^l k^{-1}}} + c_2 e^{-L_m \sqrt{\varepsilon^l k^{-1}}} - \frac{1}{\mu k^{-1}} \frac{dp}{dx_1}. \quad (4.14)$$

Hence, the constant  $c_2$  is given by

$$c_2 = \frac{v_L - \frac{1}{\mu k^{-1}} \frac{dp}{dx_1} \left( e^{L_m \sqrt{\varepsilon^l k^{-1}}} - 1 \right)}{e^{-L_m \sqrt{\varepsilon^l k^{-1}}} - e^{L_m \sqrt{\varepsilon^l k^{-1}}}}. \quad (4.15)$$

Substituting Eq. (4.15) into Eq. (4.12), we find

$$c_1 = -\frac{v_L - \frac{1}{\mu k^{-1}} \frac{dp}{dx_1} \left( e^{L_m \sqrt{\varepsilon^l k^{-1}}} - 1 \right)}{e^{-L_m \sqrt{\varepsilon^l k^{-1}}} - e^{L_m \sqrt{\varepsilon^l k^{-1}}}} + \frac{1}{\mu k^{-1}} \frac{dp}{dx_1}. \quad (4.16)$$

With the constants  $c_1$  and  $c_2$  determined, the exact solution, Eq. (4.10), can now be computed and compared with the numerical results presented in the next section.

## 4.2 Validation of Numerical Results

To verify the numerical solution, we apply the mixed finite element method of Taylor-Hood type to the nonlinear Brinkman equation (3.1) and the continuity equation (3.2) when the nonlinear term, cilia velocity, and gravitational term are neglected. We obtain the velocity of the PCL fluid in the two-dimensional domain. The result is averaged over  $x_1$ -axis and then compared with the analytical solution, Eq. (4.10). The values of the parameters used in this computation are: the inverse of permeability  $k^{-1}$

is  $\frac{1}{0.0027}$ , the pressure gradient  $\frac{dp}{dx}$  is  $-1 \times 10^{-9}$ , the porosity  $\varepsilon^l$  is 0.7487, the viscosity  $\mu$  is  $3 \times 10^{-6}$  and the both the boundary velocity  $v_L$  and the height of domain  $L_m$  are set to be one. For a two-dimensional domain, we discretize our domain with four different levels of mesh refinement. The number of nodes in the  $x_2$ -direction ranges from 7 (coarsest mesh) to 61 (finest mesh). Figure 4.1 presents the average velocity  $v_1$  profiles for 7, 17, 31 and 61 nodes in the  $x_2$ -direction. The corresponding results are shown together with the exact solution to illustrate the convergence behavior. The average velocity  $v_1$  for 7, 17, 31 and 61 nodes are represented using plus, circle, cross, and diamond markers, respectively, while the exact solution is indicated by an asterisk marker. The  $l_2$ -norm errors of 7, 17, 31 and 61 nodes are 0.0919, 0.0277, 0.0141 and 0.0053, respectively. These results demonstrate that the numerical solution converges to the exact solution as the number of nodes in the  $x_2$ -direction increases. This indicates that the numerical result is in a good agreement with the exact solution.

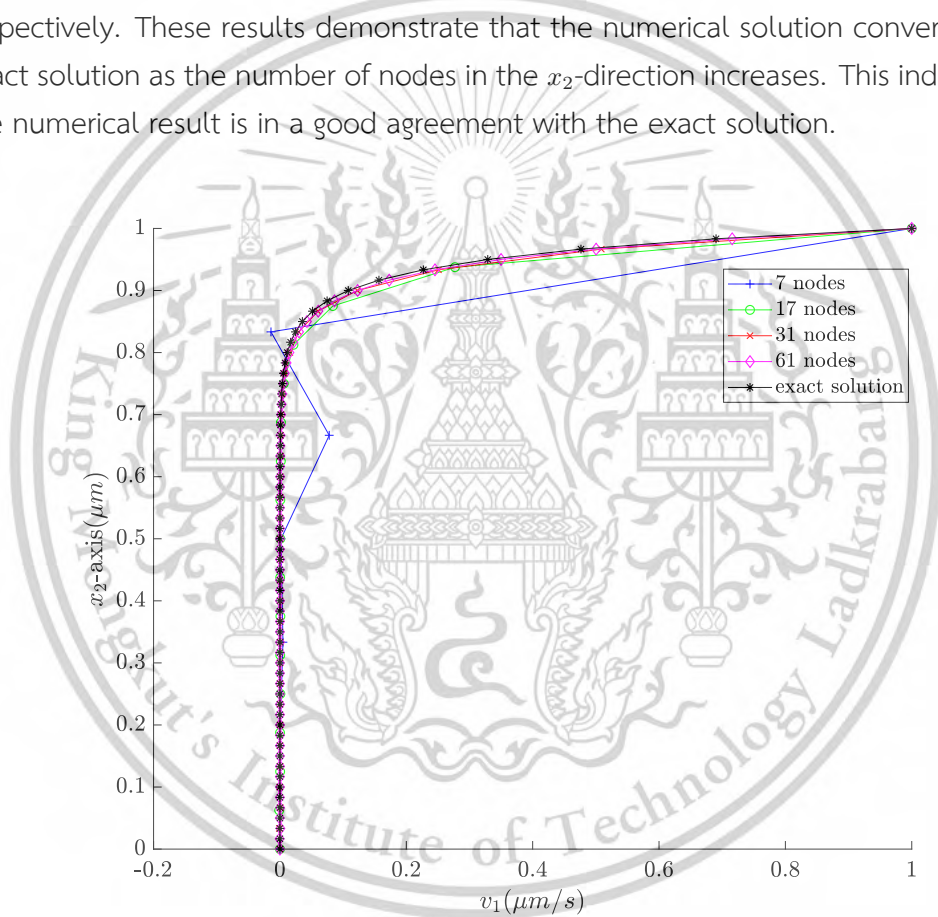


**Figure 4.1:** The average velocity  $v_1$  profile of two-dimensional numerical solution for 7, 17, 31 and 61 nodes and the exact solution when  $\theta = 90^\circ$  along  $x_2$ -axis.

### 4.3 Numerical Solutions

In this section, we present the numerical results for the velocities of the PCL and the ML using the nonlinear Brinkman, steady-state Navier-Stokes, and Stokes equations. These equations are solved using a mixed finite element method of Taylor-Hood type, and the Newton's method.

This material is reserved for educational use only, not allowed for commercial use.

Forbidden to modify the content, and cite the document when use.

### 4.3.1 The Numerical Solutions of the Nonlinear Brinkman and the Steady-State Navier-Stokes Equations

In this section, we present the numerical solutions of the nonlinear Brinkman and the steady-state Navier-Stokes equations by using a mixed finite element method combined with the Newton's method. Since only the forward stroke is considered, we assume the cilia have maximum velocity at the angle  $\theta = 90^\circ$  and the velocity decreases with decreasing angle  $\theta$  to  $\theta = 50^\circ$  and reaches zero at the angle  $\theta = 40^\circ$ , where the cilia stop beating. The speed of cilia  $|v^s|$  used in this study is provided in [42], which contains eighth-order polynomial functions describing the speed of cilia at each angle. The cilium length is normalized to a unit length of one. So, the polynomial function from [42] is shown in Table 4.1.

**Table 4.1:** The eighth-order polynomial functions:  $a_1\lambda^8 + a_2\lambda^7 + a_3\lambda^6 + a_4\lambda^5 + a_5\lambda^4 + a_6\lambda^3 + a_7\lambda^2 + a_8\lambda$  is used to approximate the speed along a cilium for the angles  $\theta = 90^\circ$  to  $50^\circ$ .

Coefficients	Degree ( $\theta$ )					
	$10^5 \times$	$50^\circ$	$60^\circ$	$70^\circ$	$80^\circ$	$90^\circ$
$a_1$		0.2498	0.4043	-0.4987	-0.3648	-0.5386
$a_2$		-1.0781	-1.6788	2.1268	1.5687	2.2148
$a_3$		1.9290	2.8656	-3.7102	-2.7659	-3.7309
$a_4$		-1.8459	-2.5945	3.4021	2.5751	3.3198
$a_5$		1.0133	1.3380	-1.7529	-1.3584	-1.6788
$a_6$		-0.3157	-0.3896	0.5012	0.4022	0.4803
$a_7$		0.0504	0.0585	-0.0717	-0.0593	-0.0694
$a_8$		-0.0023	-0.0024	0.0049	0.0044	0.0050

The variable  $\lambda$  is the distance along cilia divided by the length of cilia. So,  $0 \leq \lambda \leq 1$ . Figure 4.2 shows the speed of cilia for the angles  $\theta = 50^\circ$  to  $90^\circ$ . The speed along the cilia increases from the base to the tip. The maximum speed occurs at  $90^\circ$  and it decreases as  $\theta$  decreases. For the cilia velocity  $v^s$  that appears in the nonlinear Brinkman equation, it is as follows

$$v^s = (v_1^s, v_2^s) = (|v^s| \sin(\theta), -|v^s| \cos(\theta)). \quad (4.17)$$

Notice that when the cilia bend downward to the angle  $\theta < 90^\circ$ , the vertical velocity of cilia becomes negative. Therefore, the vertical velocity of the cilia  $v_2^s$  is negative in this work.

For other variables, the viscosity  $\mu$  is  $3 \times 10^{-6}$  ( $g/(\mu m \cdot s)$ ) and the gravity  $\mathbf{g}$  is  $(0, 9.8 \times 10^6)$  ( $\mu m/s^2$ ). The density of the fluid  $\rho = 992.2 \times 10^{-15}$  ( $g/\mu m^3$ ) is the water density at  $40^\circ$  [36]. For the inverse of the permeability tensor,  $\mathbf{k}^{-1}$ , is obtained by inverting the permeability tensor  $\mathbf{k}$  from [9]. The values of  $\mathbf{k}^{-1}$  for the angle  $\theta = 90^\circ$  to  $50^\circ$  are provided in Table 4.2. Table 4.2 shows the values of the element  $k_{ij}^{-1}$ ,  $i, j = 1, 2$ .

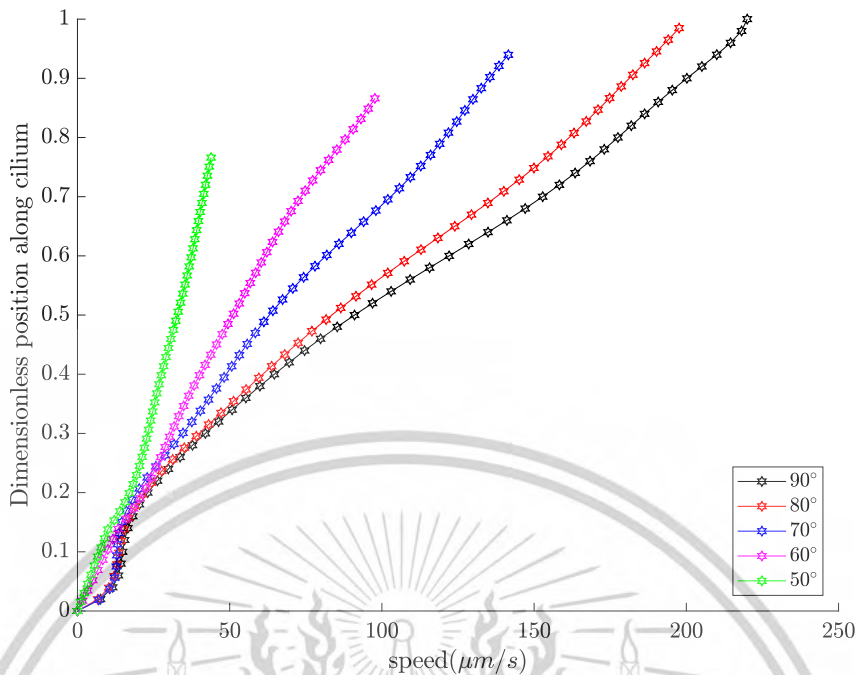


Figure 4.2: The cilia speed for the angle 50°, 60°, 70°, 80° and 90° of the tensor  $k^{-1}$ .

Table 4.2: The inverse of the permeability tensor  $k^{-1}$  for the angles  $\theta = 50^\circ$  to  $90^\circ$ .

$\theta$	The inverse of the permeability tensor, $k^{-1}$			
	$k_{11}^{-1}$	$k_{12}^{-1}$	$k_{21}^{-1}$	$k_{22}^{-1}$
50°	992.3664	-381.6794	-381.6794	916.0305
60°	748.2993	-204.0816	-204.0816	510.2041
70°	658.1741	-106.1571	-106.1571	339.7028
80°	596.5463	-47.0958	-47.0958	266.8760
90°	556.3690	-14.6413	-14.6413	263.5432

Next, we provide the value of the porosity. The porosity  $\varepsilon^l$  representing the fluid volume fraction depends on the angle  $\theta$ . It is adopted from [9, 42] expressed as follows

$$\varepsilon^l(\theta) = 0.5223\theta^5 - 3.0283\theta^4 + 7.0630\theta^3 - 8.4987\theta^2 + 5.5056\theta - 0.8627. \tag{4.18}$$

The plot of the porosity function (4.18) is shown in Figure 4.3, illustrating how the porosity  $\varepsilon^l$  varies with the angle  $\theta$  (in radians) from  $50^\circ$  to  $90^\circ$ , which is used in the domain  $\Omega_1$ . Notice that the porosity is a constant for each angle  $\theta$ . The term  $\varepsilon^l$  appearing in the term  $f$  is employed from [42], which is

$$\varepsilon^l = \frac{\partial \varepsilon^l}{\partial \theta} \frac{\partial \theta}{\partial t}, \tag{4.19}$$

and

This material is reserved for educational use only, not allowed for commercial use.  
 Forbidden to modify the content, and cite the document when use.

$$\frac{\partial \theta}{\partial t} = \frac{|\psi^*|}{\lambda}. \tag{4.20}$$

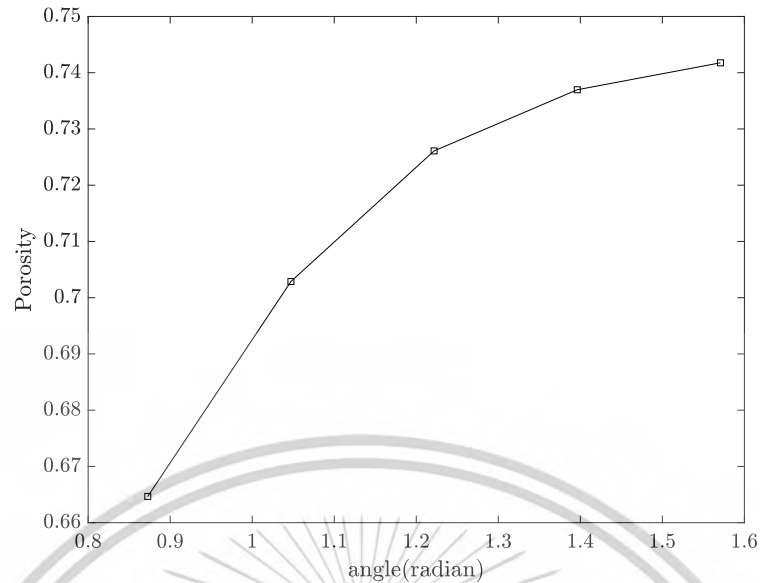


Figure 4.3: The porosity for the angles  $50^\circ$ ,  $60^\circ$ ,  $70^\circ$ ,  $80^\circ$  and  $90^\circ$

Next, we determine the velocity of the PCL fluid for angles  $50^\circ$  -  $90^\circ$  by applying the mixed finite element method of the Taylor–Hood type and the Newton’s method to the nonlinear Brinkman and steady-state Navier–Stokes equations with the boundary conditions provided in Section 3.2.1. The mesh refinement is generated by the open-source software Netgen [31]. The numbers of nodes are between 1000 to 1700 grid points, as shown in Figure 4.4. Figure 4.4 shows the meshes generated in the PCL domain where the cilia make the angles  $50^\circ$  to  $90^\circ$  to the horizontal plane. In each graph, the bold horizontal line represents the free-fluid/porous-medium interface at  $x_2 = y_s$ .

For the nonlinear term solved by the Newton’s method, we use an initial guess  $\bar{\mathbf{V}}^{(1)} = \mathbf{1}$  to calculate the numerical solutions. The iterations are stopped when  $\|\Delta\bar{\mathbf{V}}\|_2 < tol$ . Here, we let the  $tol = 5 \times 10^{-4}$ . Table 4.3 shows the number of iterations of the Newton’s method, the computation time, and the number of degrees of freedom (#dof) for each angle. Since the height of our numerical domain is 1, when the cilia bend down from  $90^\circ$  to the angle  $\theta = 80^\circ$ , the height of the porous medium at  $80^\circ$  is  $y_s = 0.9848$  and the height of the free-fluid region is 0.0152, a small value. So finer elements are required in the free-fluid region. Therefore, the number of degrees of freedom when the angle  $\theta = 80^\circ$  is higher those that for the other angles.

The velocities of the PCL fluid,  $v_1$  and  $v_2$ , are illustrated in Figures 4.5 and 4.6. Figure 4.5 shows the velocity  $v_1$  of the PCL fluid when the angles  $\theta = 50^\circ$  to  $90^\circ$ . The velocity is zero at the roots of the cilia. Figure 4.6 illustrates the velocity  $v_2$  of the PCL fluid when the angles  $\theta = 50^\circ$  to  $90^\circ$ . During the forward stroke, the cilia start at the angle  $\theta = 90^\circ$ , bend down to the angle  $\theta = 50^\circ$  and stop beating at  $\theta = 40^\circ$ . So, the velocity  $v_2$  becomes negative for  $\theta < 90^\circ$ , while at  $\theta = 90^\circ$ , the velocity  $v_2$  is supposed

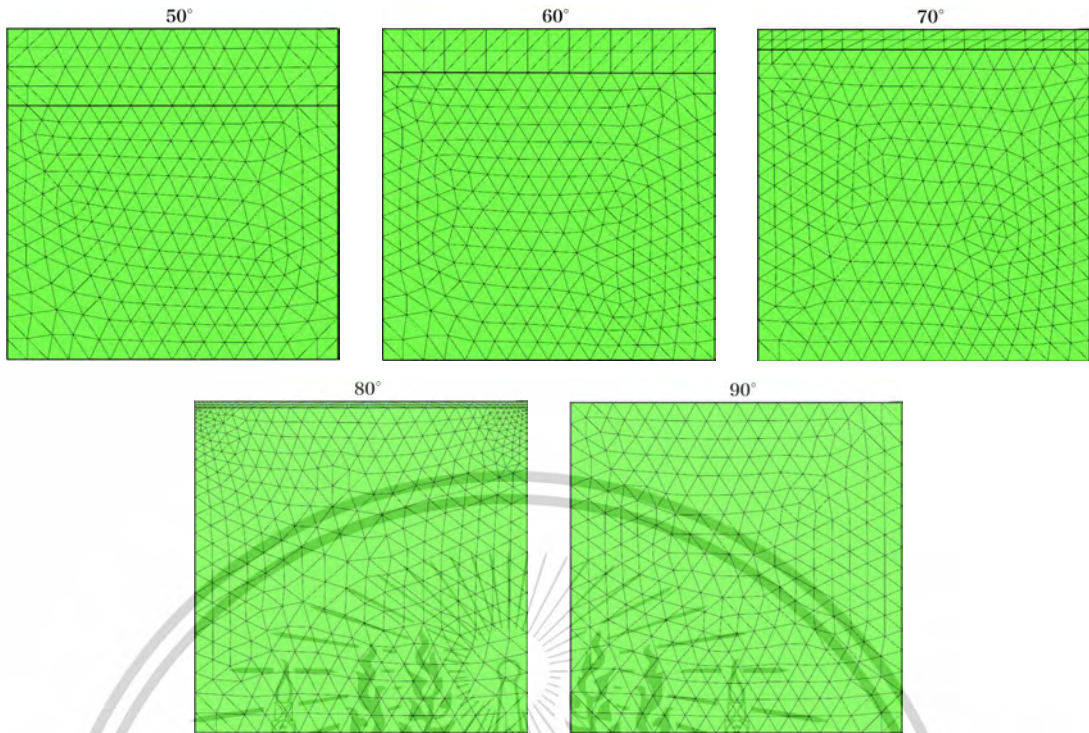


Figure 4.4: The generated mesh of the PCL domain for various angles by using the open-source software Netgen [31].

Table 4.3: The number of iterations of Newton's method, computation time and number of degrees of freedom for each angle.

$\theta$	number of iterations	time (min)	#dof
50°	84	1600	2678
60°	56	1065	2863
70°	34	748	3184
80°	7	178	3725
90°	2	29	2267

to be zero but it is shaking around zero because of the numerical error.

Next, we average the velocities of  $v_1$  and  $v_2$  over  $x_1$ -direction as shown in Figures 4.7 and 4.8. In these Figures, each curve is represented by two colors, except at  $\theta = 90^\circ$ , which is represented by a single color. The color in the lower part of the curve indicates the velocity in the porous domain  $\Omega_1$ , while the upper part represents the velocity in the free-fluid region  $\Omega_2$ . The color distinction is also used in Figure 4.9. Figure 4.7 shows the average velocities  $v_1$  of the PCL fluid for all angles. The highest velocity occurs at the angle  $\theta = 90^\circ$  and the velocity  $v_1$  decreases when  $\theta$  decreases. The average velocities  $v_2$  of the PCL fluid for all angles are illustrated in Figure 4.8. The figure shows that the velocity at the angle  $\theta = 90^\circ$  is almost zero, while the velocities at other angles are negative. Notice that the average velocities of  $v_2$  of the PCL fluid decrease rapidly from  $\theta = 90^\circ$  to  $\theta = 80^\circ$ , then gradually decrease until  $\theta = 60^\circ$ . From  $\theta = 60^\circ$  to  $\theta = 50^\circ$ , the

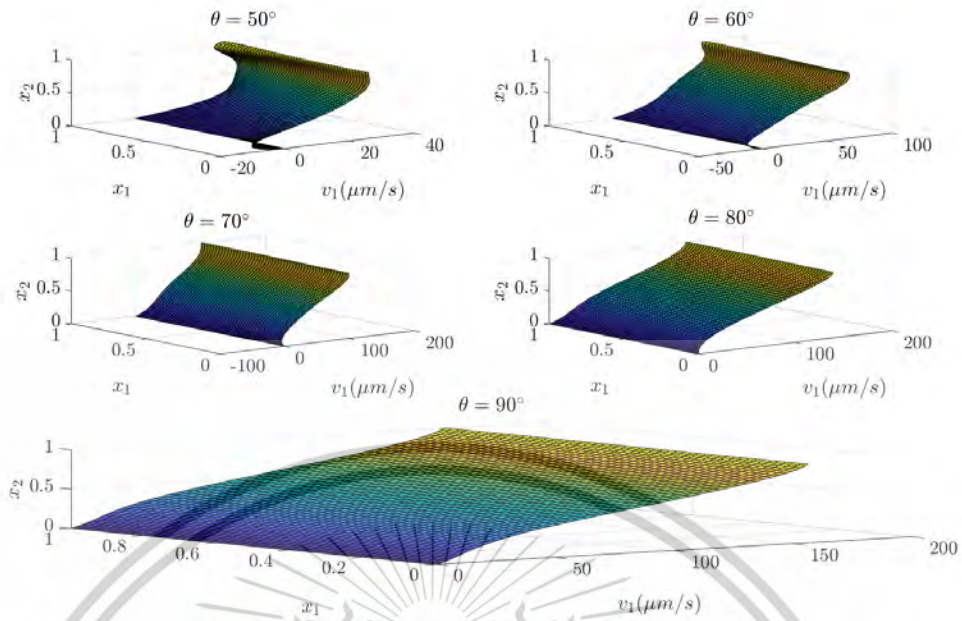


Figure 4.5: The velocity of the PCL fluid  $v_1$  in  $x_1$ -direction when the angles  $\theta = 50^\circ, 60^\circ, 70^\circ, 80^\circ,$  and  $90^\circ$ .

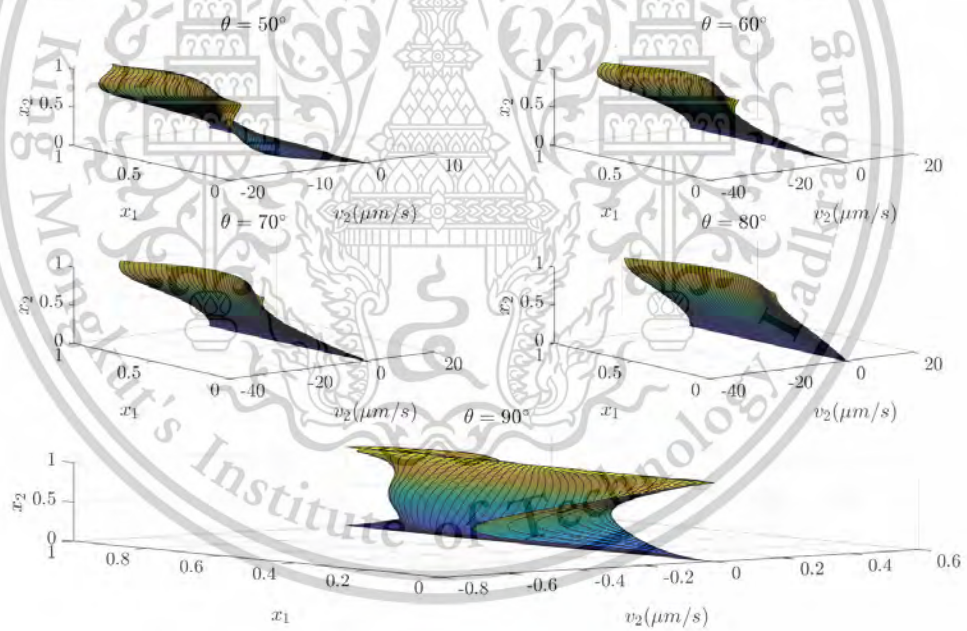


Figure 4.6: The velocity of the PCL fluid  $v_2$  in  $x_2$ -direction when the angles  $\theta = 50^\circ, 60^\circ, 70^\circ, 80^\circ,$  and  $90^\circ$ .

average velocity increases. This is because the cilia begin to stop beating, and the cilia stop beating at  $\theta = 40^\circ$ . Figure 4.9 displays the speeds of the PCL fluid by using the value from Figures 4.7 and 4.8 for all angles. Note that the speed profiles of each angle are almost the same as the average velocity of  $v_1$ . This indicates that the velocity in the  $x_1$ -direction has significant influence on the motion of the PCL fluid than the velocity in the  $x_2$ -direction. Figure 4.10 shows the speed of the PCL fluid and the speed of cilia for

each angle. The speed of the PCL fluid is approximately 11%, 12%, 20%, 25% and 26% lower than the speed of cilia for the angle  $\theta = 50^\circ, 60^\circ, 70^\circ, 80^\circ$  and  $90^\circ$ , respectively, which is in accordance with a physical meaning that the fluid speed is slower than the speed of solid phases.

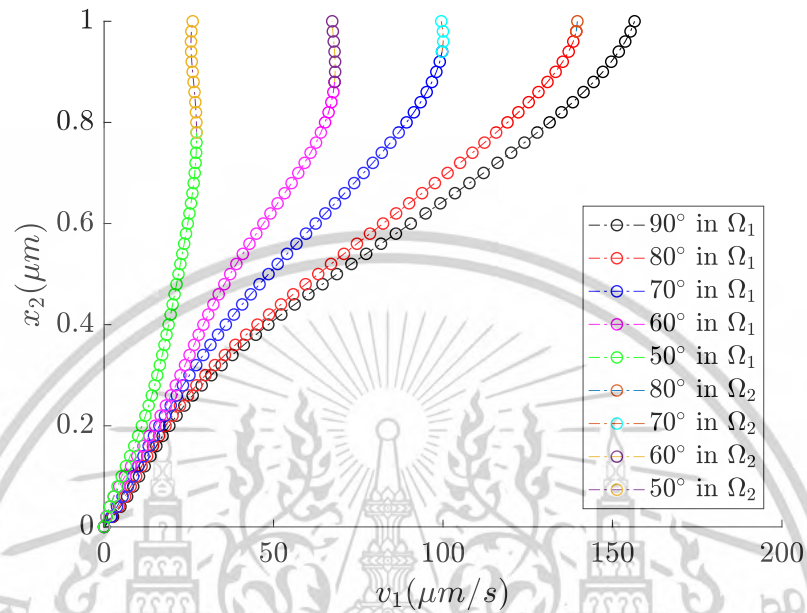


Figure 4.7: The average velocity  $v_1$  of the PCL fluid for 5 different angles.

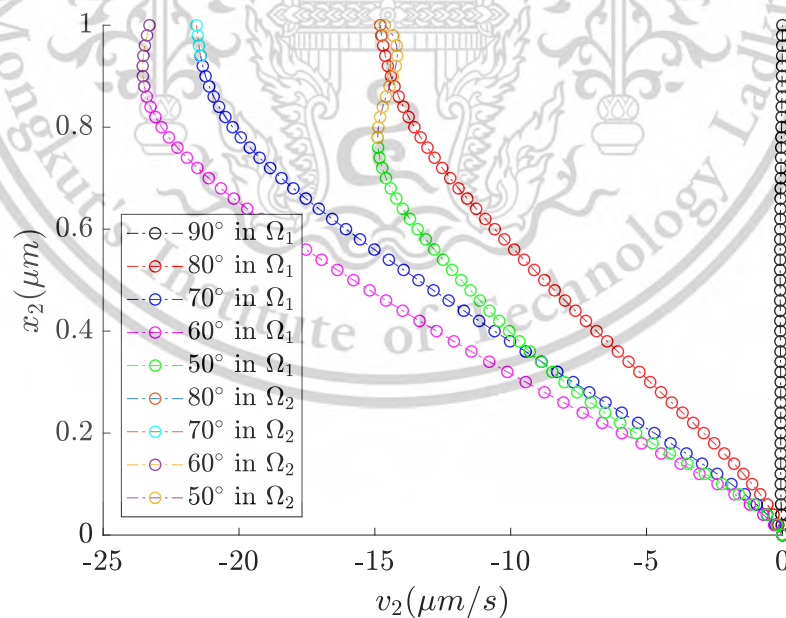


Figure 4.8: The average velocity  $v_2$  of the PCL fluid for 5 different angles.

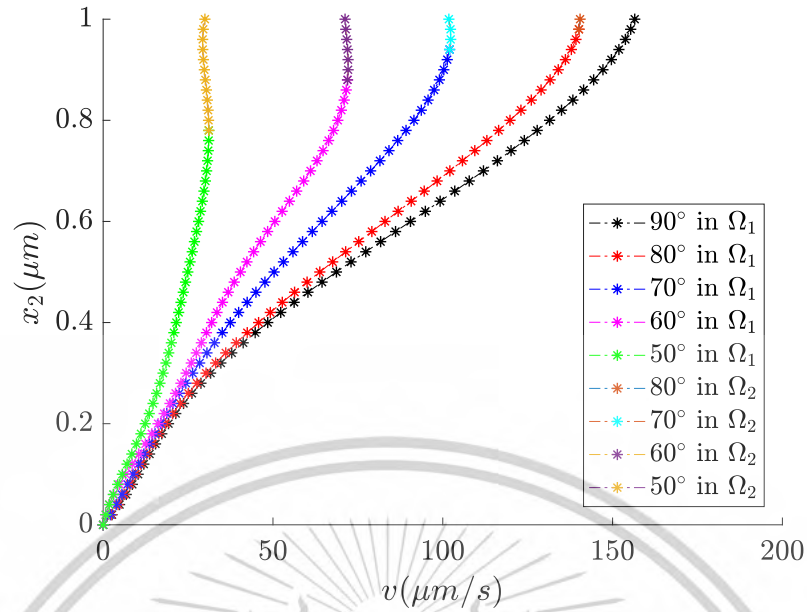


Figure 4.9: The speeds of the PCL fluid for 5 different angles.

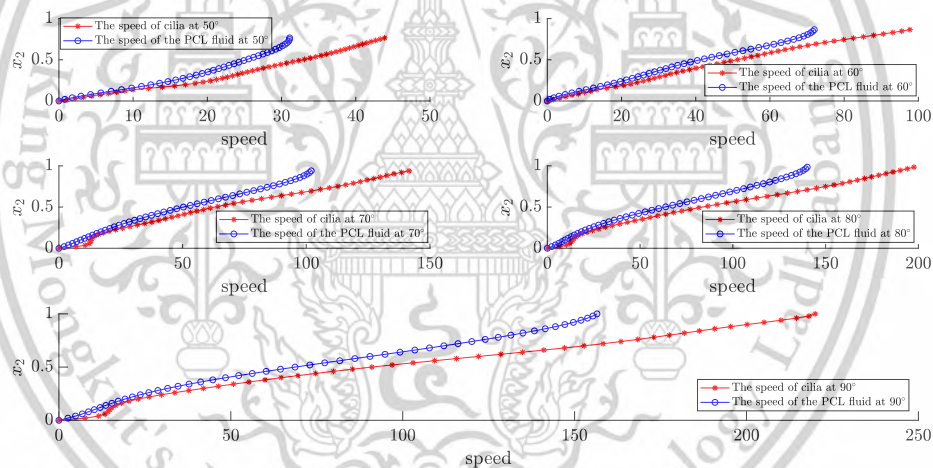


Figure 4.10: Comparison between the speeds of the PCL fluid and cilia for each angle.

To compare our numerical solution with an available research, we compute the average speed of the PCL fluid for all angles. The result depicted in Figure 4.11 shows that the velocity is zero at the bottom and increases smoothly, reaching its maximum at the top of the domain. Next, we compare the average speed for all angles with the experimental data reported in [21]. They investigated the movement of the PCL in well-differentiated human tracheobronchial epithelial cell cultures derived from non-diseased (healthy) donors. The study employed conventional and confocal microscopy techniques using fluorescent microspheres and photoactivated fluorescent dyes. The research has revealed that the velocity of the PCL fluid is approximately  $39.2 \pm 4.7 \mu\text{m}/\text{s}$ . From Figure 4.11, the average speed for all angles is found to be approximately  $43 \mu\text{m}/\text{s}$ , which is in good agreement with the experimental results.

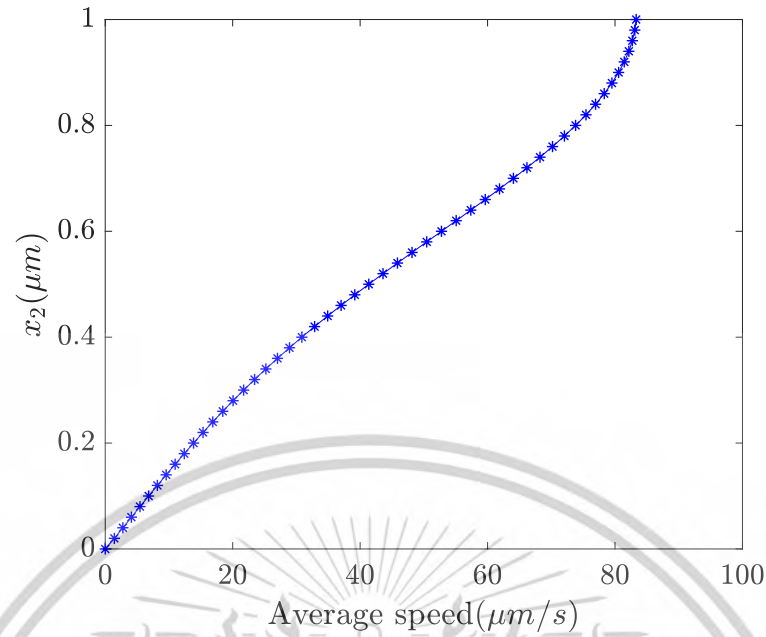


Figure 4.11: The average speed for all angles.

To enable more convenient use of the results for applications, we approximate the average speed profile for all angles using the 15th-degree polynomial. The coefficients of this polynomial approximation are presented in Table 4.4. In this context, the variable  $h_p$  represents the position along the  $x_2$ -axis, ranging from 0 to 1 and  $\varphi_i, i = 0, 1, \dots, 15$  are the coefficients. Figure 4.12 illustrates the comparison between the 15th-degree polynomial approximation and the average speed for all angles. The  $l_2$ -norm error between the two curves is 0.0078.

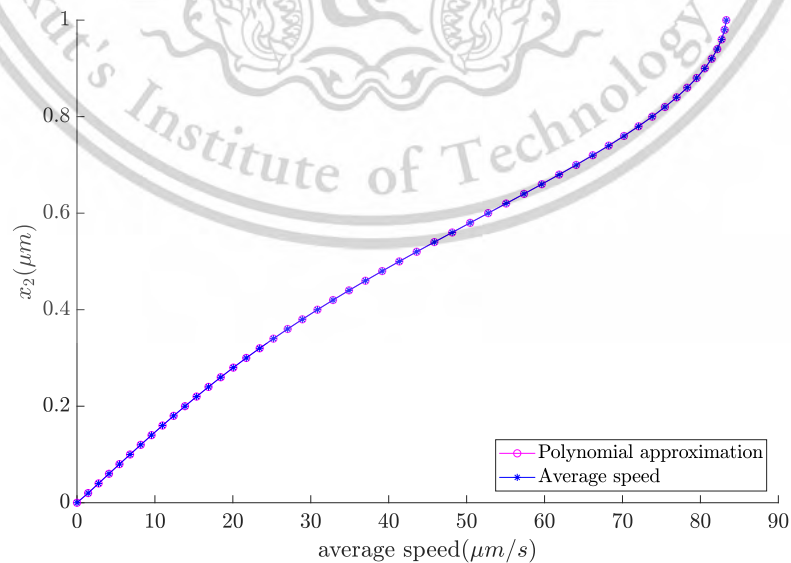


Figure 4.12: The polynomial approximation and the average speed of the PCL fluid.

**Table 4.4:** The fifteenth-order polynomial functions:  $p(h_p) = \varphi_{15}h_p^{15} + \varphi_{14}h_p^{14} + \varphi_{13}h_p^{13} + \varphi_{12}h_p^{12} + \varphi_{11}h_p^{11} + \varphi_{10}h_p^{10} + \varphi_9h_p^9 + \varphi_8h_p^8 + \varphi_7h_p^7 + \varphi_6h_p^6 + \varphi_5h_p^5 + \varphi_4h_p^4 + \varphi_3h_p^3 + \varphi_2h_p^2 + \varphi_1h_p + \varphi_0$  for the average speed of the PCL fluid for all angles.

Coefficient	$10^7 \times$
$\varphi_{15}$	0.085160354082839
$\varphi_{14}$	-0.665839529348487
$\varphi_{13}$	2.355791755084539
$\varphi_{12}$	-4.987656285240524
$\varphi_{11}$	7.041097650319588
$\varphi_{10}$	-6.990579023195928
$\varphi_9$	5.016958957810736
$\varphi_8$	-2.634288563320434
$\varphi_7$	1.012894674178318
$\varphi_6$	-0.282632301281962
$\varphi_5$	0.056087826666958
$\varphi_4$	-0.007641781629541
$\varphi_3$	0.000682936187941
$\varphi_2$	-0.000035983965625
$\varphi_1$	0.000007645678491
$\varphi_0$	0.000000000059390

#### 4.3.2 The Numerical Solutions of the Stokes Equation

In this section, we present the numerical results of the Stokes equation by using a mixed finite element method of Taylor-Hood type in both the free-fluid region ( $\Omega_3$ ) and the ML ( $\Omega_4$ ). To determine the mucus velocity as realistically as possible, we adopt the PCL fluid velocity in the porous medium from [41], where the angles ranging from  $90^\circ$  to  $50^\circ$  are considered, within a single fixed numerical domain. Unlike the previous work that each fixed numerical domain contains only one angle  $\theta$ . This velocity profile, obtained from [41], is used as the bottom boundary condition of the domain  $\Omega_3$ . Then, the velocity of the fluid at the top of the domain  $\Omega_3$  is used to be the bottom boundary condition for the domain  $\Omega_4$ . To find the fluid velocity in the domain  $\Omega_3$ , we first provide the velocities  $v_1$  and  $v_2$  of the PCL fluid at the cilia tips during the forward stroke obtained from [41] in Figures 4.13 and 4.14, respectively. The different colors represent the velocity at different angles. Figure 4.13 illustrates the velocity  $v_1$  of the PCL fluid at the tips of the cilia for the angles  $\theta = 50^\circ, 60^\circ, 70^\circ, 80^\circ$  and  $90^\circ$ . It is observed that the velocity is maximum at  $\theta = 90^\circ$  and then it decreases as  $\theta$  decreases, reaching its minimum at  $\theta = 50^\circ$ . Figure 4.14 shows the velocity  $v_2$  of the PCL fluid at the tips of the cilia of the angles  $\theta = 50^\circ, 60^\circ, 70^\circ, 80^\circ$  and  $90^\circ$ . Note that the velocity  $v_2$

This material is reserved for educational use only; not allowed for commercial use.

is positive at  $\theta = 90^\circ$  and decreases to negative values at other angles. This is because the cilia bend downward during the forward stroke. These velocities are then applied as the bottom boundary condition of the domain  $\Omega_3$  (at  $\Gamma_8$ ), except for the velocity at  $\theta = 90^\circ$  because of the absence of the free-fluid region when the cilia are perpendicular to the horizontal plane.

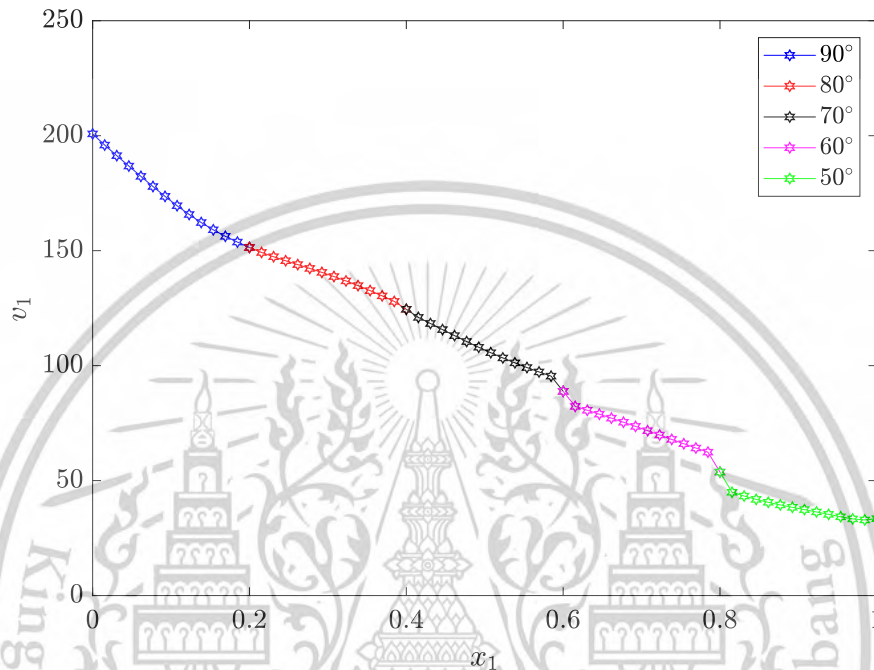


**Figure 4.13:** The velocities  $v_1$  of the PCL fluid at the tips of cilia at the angles  $\theta = 50^\circ, 60^\circ, 70^\circ, 80^\circ$  and  $90^\circ$ .

To find the velocity of the fluid in  $\Omega_3$  and  $\Omega_4$ , we specify the values of the variables used in the numerical calculations for these domains. Since the viscosities of the PCL fluid and mucus are different, we use  $\mu = 3 \times 10^{-6}$  ( $g/(\mu m \cdot s)$ ) in  $\Omega_3$  [42] and  $\mu = 2 \times 10^{-2}$  ( $g/(\mu m \cdot s)$ ) in  $\Omega_4$  [10]. The values of the other variables are the same as those in the previous section. The velocities of the fluids in  $\Omega_3$  and  $\Omega_4$  are solved by solving the Stokes equation with the boundary condition mentioned in Section 3.2.2 using the mixed finite element method of Taylor-Hood type. The mesh refinement is generated using the open-source software Netgen [31] as drawn in Figure 4.15. Figure 4.15 shows the mesh generation for the free-fluid region  $\Omega_3$  and the ML  $\Omega_4$  with 3051 grid points. The red bold horizontal line represents the interface between the PCL and ML, serving as the boundary separating the two regions. The region above the interface is the mucus layer ( $\Omega_4$ ), while the region below the interface represents the free-fluid region ( $\Omega_3$ ). Each of the horizontal steps below the interface corresponds to the tips of the cilia at each angle. At  $\theta = 90^\circ$ , the cilia are fully vertical, and no free-fluid region is formed. As the angle decreases to  $\theta = 80^\circ$ , the cilia begin to tilt, and a free-fluid region appears with small height. Further decreases in angle to  $\theta = 70^\circ, 60^\circ$  and  $50^\circ$ , result in free-fluid regions with increasing vertical height. Therefore, each step in the domain  $\Omega_3$

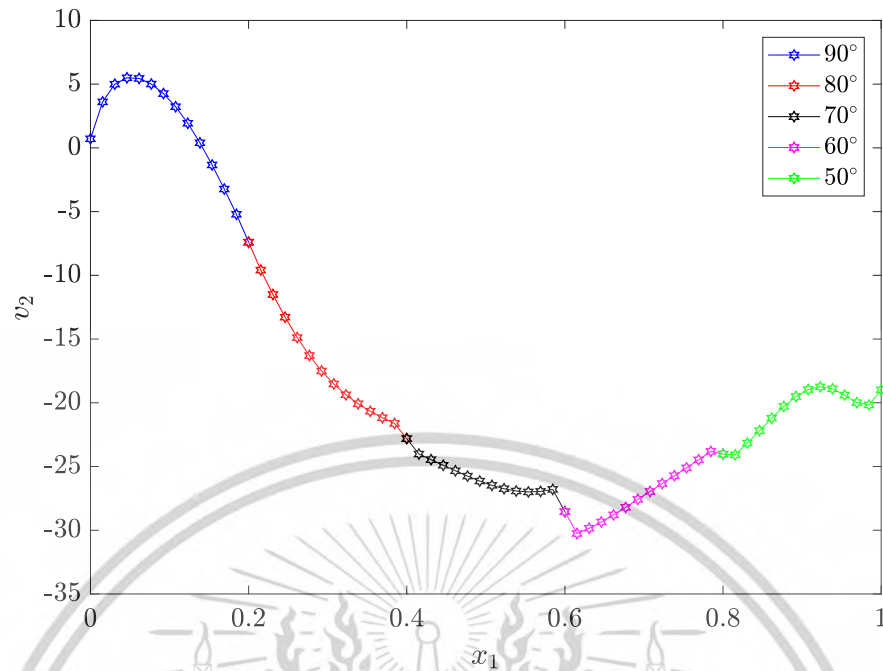


Figure 4.14: The velocities  $v_2$  of the PCL fluid at the tips of cilia at the angles  $\theta = 50^\circ, 60^\circ, 70^\circ, 80^\circ$  and  $90^\circ$ .

increases in height as the angle decreases, with the tallest free-fluid region occurring at  $\theta = 50^\circ$ .

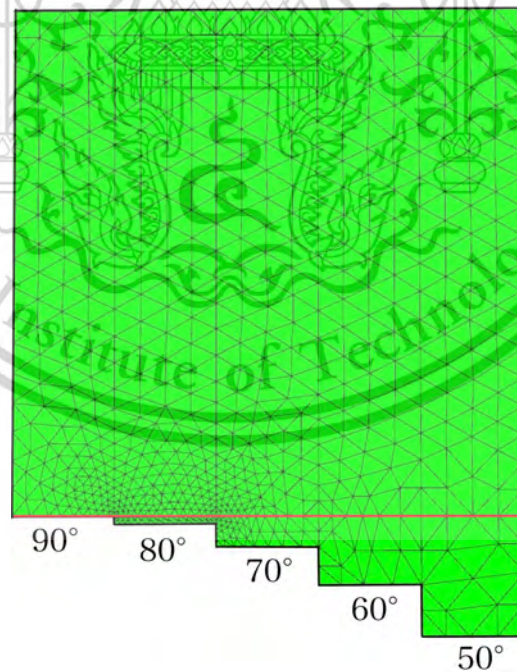


Figure 4.15: Generated mesh for the free-fluid and ML domains using the open-source software Netgen software [31].

From Figure 3.2, the free-fluid domain  $\Omega_3$  covers the angles from  $\theta = 80^\circ$  to  $\theta = 50^\circ$  since the free-fluid region appears when the cilia beat at angles less than  $90^\circ$ .

This corresponds to the range of  $x_1$  from 0.2 to 1. The heights of the vertical segment of  $\Omega_3$ , measured from the  $y_{in}(\theta)$  to  $y_{PCL}$ , for the angles  $\theta = 80^\circ, 70^\circ, 60^\circ$ , and  $50^\circ$  are 0.0152, 0.0603, 0.1339, and 0.2339, respectively. As a result, the velocities  $v_1$  and  $v_2$  of the fluid in  $\Omega_3$  are plotted for angles ranging from the angles  $\theta = 80^\circ$  to  $\theta = 50^\circ$ , as shown in Figures 4.16 and 4.17, respectively. Figure 4.16 shows the velocity  $v_1$  of the fluid in  $\Omega_3$ , where the maximum velocity occurs at the angle  $\theta = 80^\circ$  and gradually decreases as  $\theta$  decreases, reaching its minimum at the angle  $\theta = 50^\circ$ . Figure 4.17 demonstrates the velocity  $v_2$  of the fluid in  $\Omega_3$ , which is negative until  $\theta = 60^\circ$ . After that it begins to increase, becoming less negative.

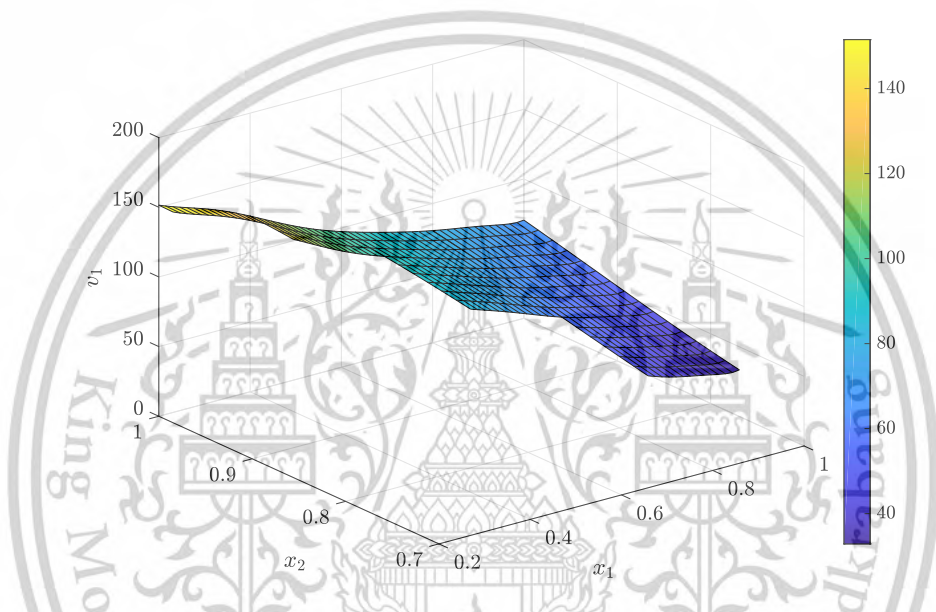


Figure 4.16: The velocity  $v_1$  of the fluid in  $\Omega_3$

Next, to determine the velocity of the mucus, we apply the fluid velocity at the top of  $\Omega_3$  as the bottom velocity for the ML ( $\Omega_4$ ). The domain  $\Omega_4$  is  $[0, 1] \times [1, 2]$ . Figure 4.18 shows the mucus velocity  $v_1$ , with the maximum value occurring at the point  $(x_1, x_2) = (0, 1)$  and the minimum values is at  $(x_1, x_2) = (0.98, 1)$ . Both maximum and minimum values occur at the bottom boundary of  $\Omega_4$ . For  $x_2 \in [1, 1.4]$ , a  $x_1$  increases, the velocity  $v_1$  decreases, whereas for  $x_2 \in [1.4, 2]$ , the velocity  $v_1$  is almost the same for all values of  $x_1$ . This indicates that most of the mucus flows with a constant velocity in the  $x_1$ -direction. Figure 4.19 displays the velocity  $v_2$  of mucus. Since the velocity  $v_2$  of the mucus is affected by the velocity  $v_2$  of the PCL fluid in  $\Omega_3$ , the velocity  $v_2$  of the mucus is negative when  $x_1 \in [0.14, 1]$  for  $x_2 \leq 1.4$ . The velocity  $v_2$  of mucus fluctuates like a wave but the value does not vary much when  $x_2 \geq 1.4$  for all  $x_1$ .

The horizontal velocity of the fluids in  $\Omega_3$  (Figure 4.16) and the mucus velocity in  $\Omega_4$  (Figure 4.18) are averaged over the  $x_1$ -axis and plotted together in Figure 4.20. This figure shows the average velocity  $v_1$  of the fluid in  $\Omega_3$  and the mucus in  $\Omega_4$ . The red squares represent the average velocity of the fluid in  $\Omega_3$  and the blue diamonds

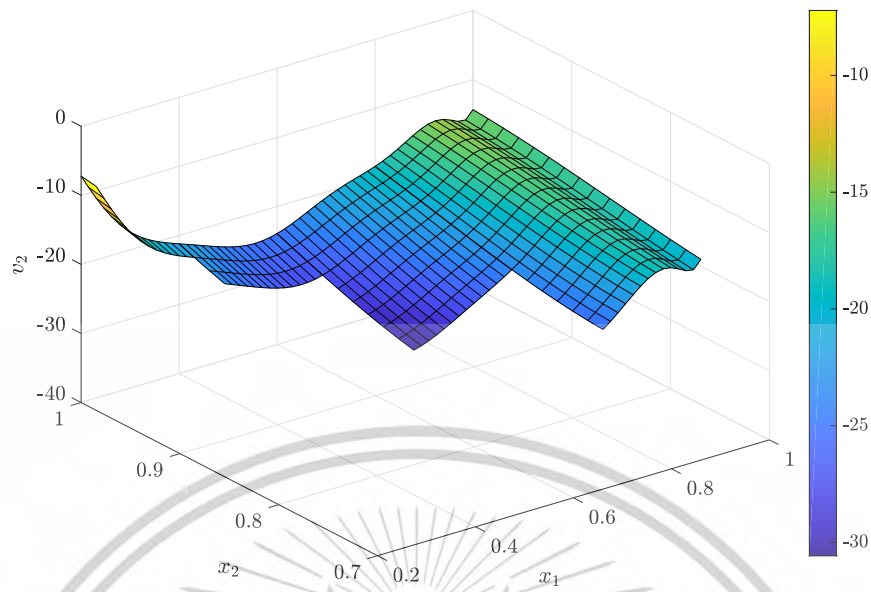


Figure 4.17: The velocity  $v_2$  of the fluid in  $\Omega_3$

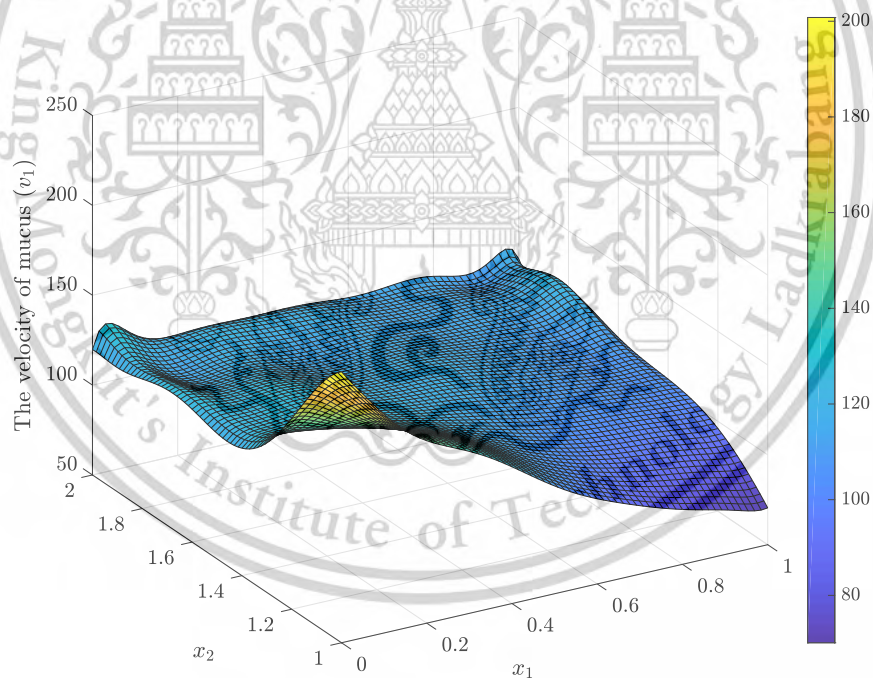


Figure 4.18: The velocity  $v_1$  of mucus.

represent the average velocity of the mucus. The average velocity  $v_1$  begins to oscillate like a vertical wave when  $x_2 \geq 1$ . The mean value of the average velocity  $v_1$  from  $x_2 = 0.7660$  to  $x_2 = 2$  is approximately  $119 \mu\text{m/s}$ . Similarly, Figure 4.21 illustrates the average vertical velocity, which shows that the average velocity  $v_2$  is negative and becomes less negative as  $x_2$  increases.

This material is reserved for educational use only, not allowed for commercial use.

Forbidden to modify the content, and cite the document when use.

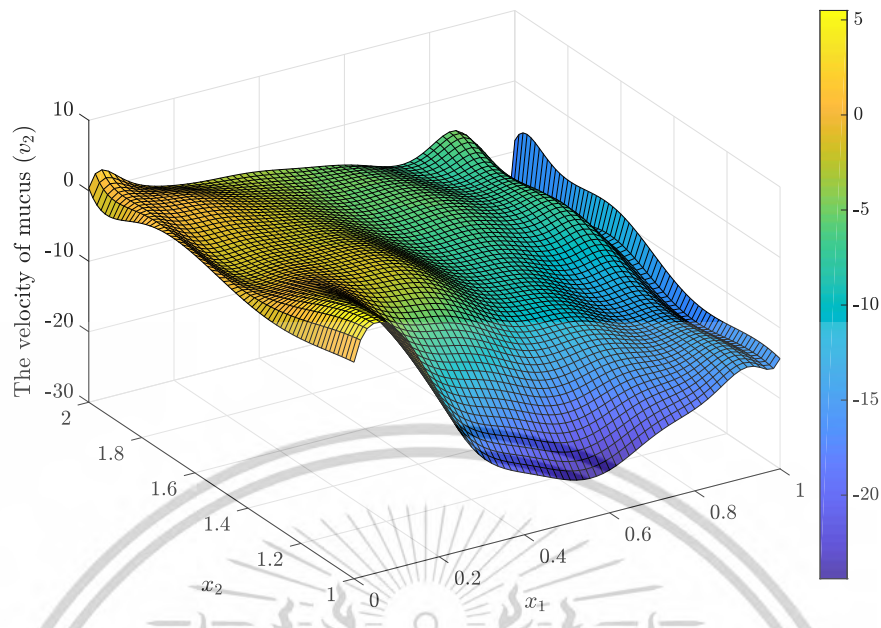


Figure 4.19: The velocity  $v_2$  of mucus.

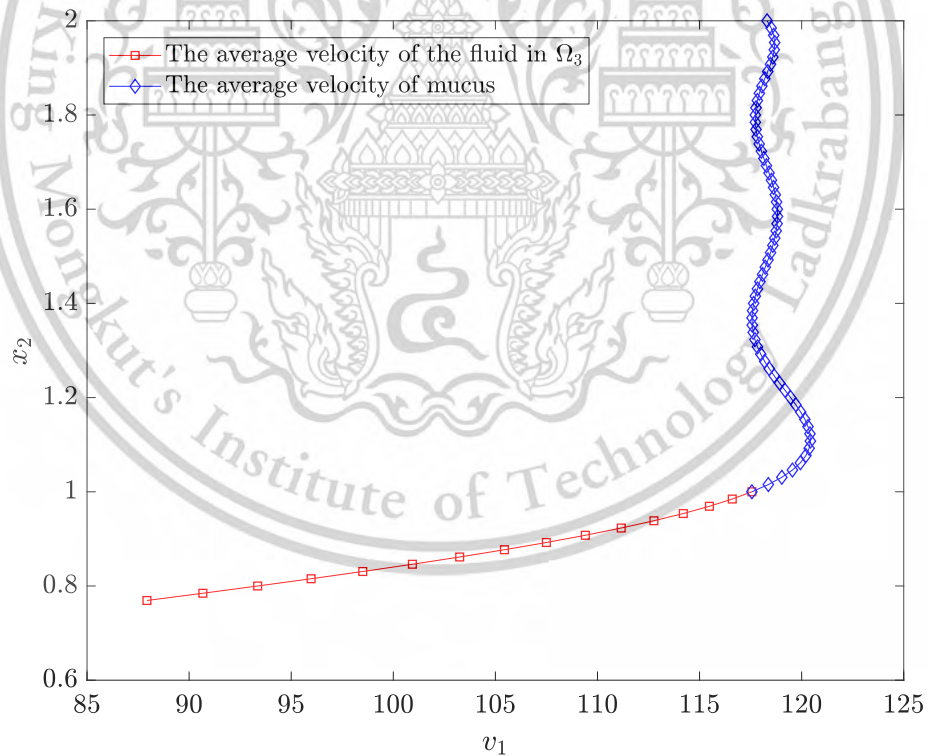


Figure 4.20: The average velocities  $v_1$  of the fluid in  $\Omega_3$  and mucus.

The velocities  $v_1$  and  $v_2$  are used to determine the speeds of the fluid in  $\Omega_3$  and mucus, denoted as  $\|v\|$ , shown in Figure 4.22. The red asterisk and blue circle represent the speeds of the fluid in  $\Omega_3$  and the mucus, respectively. The mean of mucus speed is approximately  $118 \mu\text{m/s}$  (or about  $7.1 \text{ mm/min}$ ). The curve of the speed is similar to the

This material is reserved for educational use only, not allowed for commercial use.  
 Forbidden to modify the content, and cite the document when use.

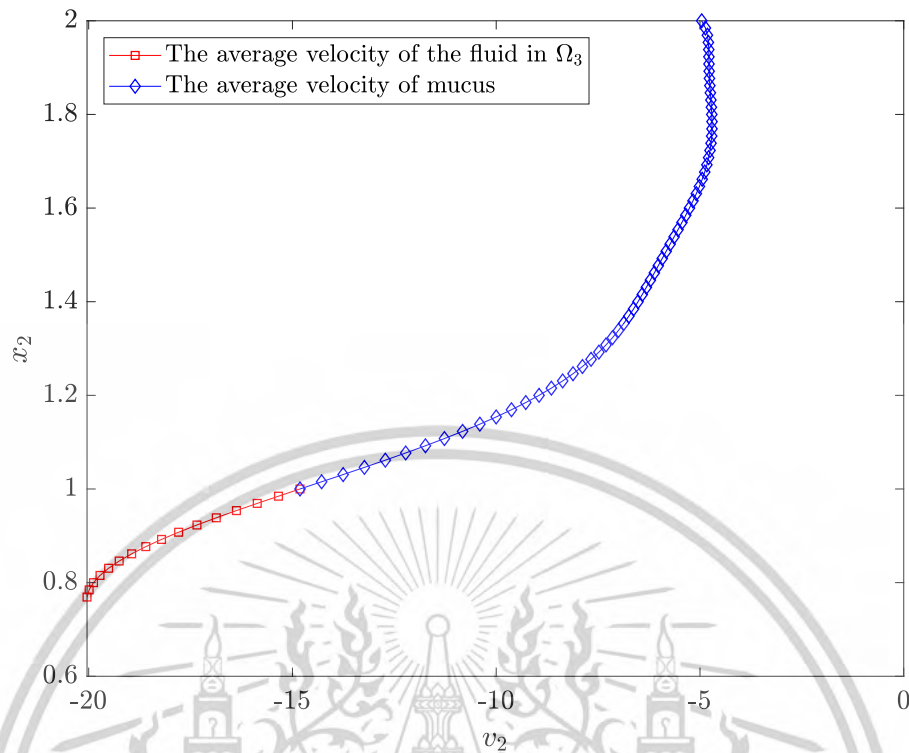


Figure 4.21: The average velocities  $v_2$  of the fluid in  $\Omega_3$  and mucus.

average horizontal velocity curve, indicating that the fluid movement is primarily driven by the velocity in the  $x_1$ -direction. Next, we compare our result with the experimental data from [45]. They studied mucociliary transport rates in 42 nonsmoking, healthy adults aged 20 to 43 years. They observed that the mucus speed ranged from 0.8 to 12.4  $mm/min$ , while our result is approximately 7.1  $mm/min$ . This result is close to the mucus transport rates observed in men aged 22–32 years and women aged 22–30 years [45].

To make the results more useful, we approximate the speeds of the fluid in  $\Omega_3$  and mucus using the 9th degree polynomial approximation. The coefficients of the ninth-order polynomial approximation of the speed are shown in Table 4.5, where the variable  $h$  is from  $y_{in}(50^\circ)$  to  $y_{ML}$ , i.e., from  $h = 0.7660$  to  $h = 2$ . Figure 4.23 displays the comparison between the ninth-order polynomial approximation and the fluid speed in  $\Omega_3$  and  $\Omega_4$  (Figure 4.22). The green square, red asterisk, and blue circle represent the polynomial approximation, the speed of the fluid in  $\Omega_3$  and the speed of the mucus, respectively. The  $l_2$ -norm error of the polynomial approximation is 0.0282.

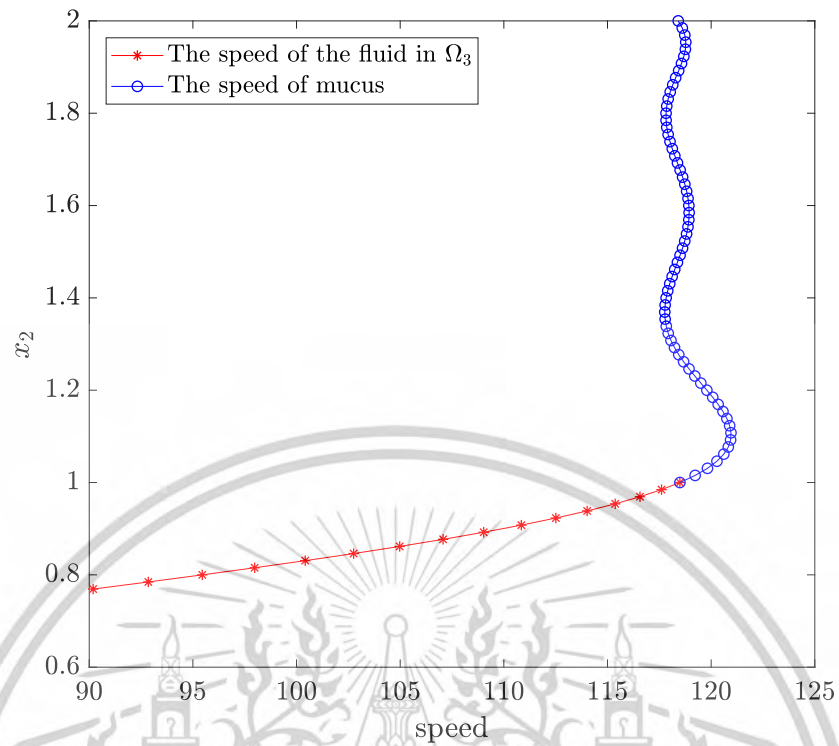


Figure 4.22: The speeds of the fluid in  $\Omega_3$  and mucus.

Table 4.5: The ninth-order polynomial functions:  $p(h) = b_9h^9 + b_8h^8 + b_7h^7 + b_6h^6 + b_5h^5 + b_4h^4 + b_3h^3 + b_2h^2 + b_1h + b_0$  for the speeds of the fluid in  $\Omega_3$  and mucus.

Coefficient	$10^6 \times$
$b_9$	0.002271511545374
$b_8$	-0.029497677298672
$b_7$	0.166716780614724
$b_6$	-0.537680842522555
$b_5$	1.089315989130731
$b_4$	-1.436339487060982
$b_3$	1.232011089245644
$b_2$	-0.663157249265035
$b_1$	0.203717832820274
$b_0$	-0.027239428286010

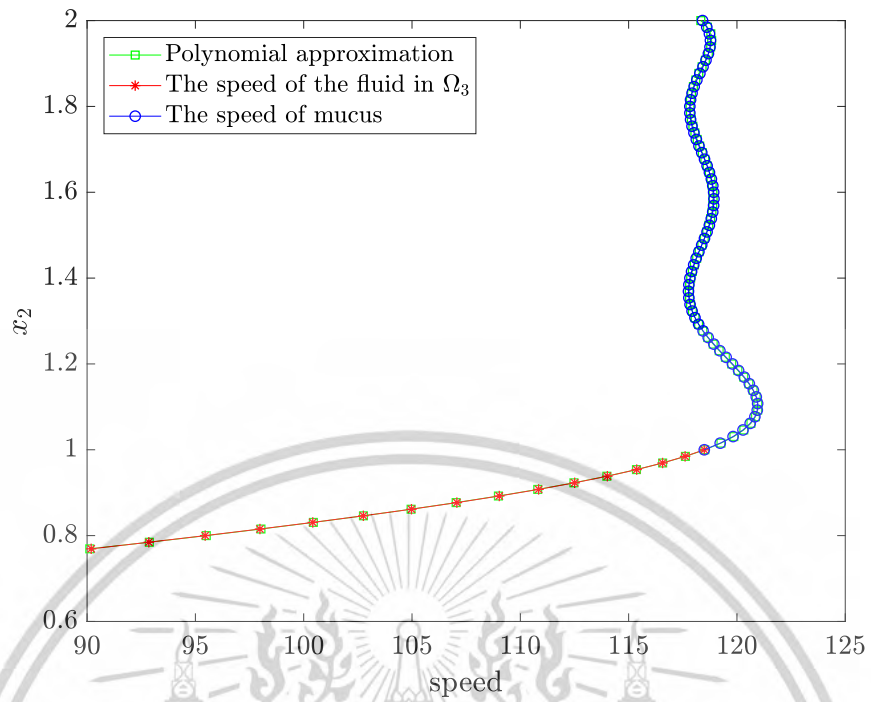


Figure 4.23: The polynomial approximation and the speeds of the fluid in  $\Omega_3$  and mucus.

# Chapter 5

## Conclusions

We consider fluid flow in the periciliary layer (PCL) and the mucus layer (ML) of the human lungs. The PCL consists of two phases: a fluid phase, known as a Newtonian fluid or PCL fluid, and a solid phase, represented by cilia. The ML lies above the PCL and consists of a single fluid phase known as mucus. When the cilia beat forward to transport mucus out of the respiratory tract, they form angles with the horizontal plane. In this study, the cilia begin the beating at  $\theta = 90^\circ$  and stop at  $\theta = 40^\circ$ . This motion divides the PCL into two distinct layers: a porous medium and a free-fluid region. The porous medium consists of both cilia and PCL fluid, whereas the free-fluid region contains only PCL fluid. The fluid flow in both the PCL and ML is influenced by the movement of cilia.

In this work, we examine fluid flow in the PCL and ML under two different cases. In the first case, we determine the velocity of the PCL fluid when the cilia make angles  $\theta = 50^\circ, 60^\circ, 70^\circ, 80^\circ$  and  $90^\circ$  with the horizontal plane, where the numerical result is solved in the fixed domain that the cilia make only one angle  $\theta$  with horizontal plane. It is important to note that the free-fluid region emerges when the cilia make the angle  $\theta \leq 80^\circ$  to the horizontal plane. To determine the velocity of the PCL fluid, we apply the nonlinear Brinkman equation in the porous domain ( $\Omega_1$ ) and the steady-state Navier-Stokes equation in the free-fluid region ( $\Omega_2$ ). These equations are discretized using the mixed finite element method of Taylor–Hood type, and Newton’s method is employed to solve the nonlinear term in the equation. The velocity is assumed to be continuous at the porous medium/free-fluid interface. The two-dimensional numerical results for the velocities  $v_1$  and  $v_2$  are provided. The velocities are then averaged to obtain the velocity profiles as well as the speed of the PCL fluid. The shape of the  $v_1$  profile is almost the same as the speed profile of the PCL fluid. This fact indicates that the velocity  $v_1$  has a significant influence on the movement of the PCL fluid. The speed of the PCL fluid is compared to the speed of cilia for each angle. This confirms that the speed of the PCL fluid is slower than that of the cilia, which follows the physical meaning. To validate our results, we compare the average speed of the PCL fluid for all angles, approximately  $43 \mu\text{m/s}$ , with the available research in [21], which is  $39.2 \pm 4.7 \mu\text{m/s}$ . The values are in good agreement.

For the second case, we examine the velocities of the fluid in the free-fluid region ( $\Omega_3$ ) and the ML ( $\Omega_4$ ). The fluid flow in  $\Omega_3$  and  $\Omega_4$  is assumed to be influenced by cilia motion in the porous medium when the cilia make various angles to the horizontal plane in one fixed domain. We first examine the velocity of the fluid in  $\Omega_3$  and then calculate the mucus velocity in  $\Omega_4$ . We employ the Stokes equation and then apply

This material is reserved for educational use only, not allowed for commercial use.

Forbidden to modify the content, and cite the document when use.

the mixed finite element method of Taylor–Hood type to the equation to calculate the velocities of the fluids in  $\Omega_3$  and  $\Omega_4$ . In this case, we assume velocity continuity at the PCL/ML interface. For the two-dimensional solution, we first compute the velocities  $v_1$  and  $v_2$  of the fluid in  $\Omega_3$ . These velocities are then used to determine the velocity of mucus. Next, the velocities of the fluid in  $\Omega_3$  and the mucus are averaged over the  $x_1$ -axis and displayed together in one graph. We then compute the speed of the average velocities in both domains. The speed profile is almost the same as the average velocity  $v_1$ , indicating that  $v_1$  has a greater influence on fluid motion than  $v_2$ . The speed of the mucus is averaged and compared with the experimental data. Our calculated mucus velocity is approximately  $118 \mu\text{m/s}$  (or about  $7.1 \text{ mm/min}$ ), which closely aligns with the experimental data for men aged 22 to 32 years and women aged 22 to 30 years, as reported by [45]. The speeds of the fluid in  $\Omega_3$  and mucus are approximated using the ninth-order polynomial approximation.

The methods and results presented here can be applied to a range of problems involving fluid flow influenced by self-movement of solid phases. The approach can be particularly useful in fields like biomedical engineering. Additionally, this study can be extended to investigate the behavior of fluids in other biological systems, such as the gastrointestinal tract, where analogous fluid transport mechanisms occur. Moreover, the results obtained from this work can be used in designing and optimizing medical devices, such as artificial lungs or respiratory support systems.

## References

- [1] R. Bansil and B.S. Turner. The biology of mucus: Composition, synthesis and organization. *Advanced drug delivery reviews*, 124:3–15, 2018.
- [2] C. Battle, C.M. Ott, D.T. Burnette, J. Lippincott-Schwartz, and C.F. Schmidt. Intracellular and extracellular forces drive primary cilia movement. *Proceedings of the National Academy of Sciences*, 112(5):1410–1415, 2015.
- [3] L.S. Bennethum and J.H. Cushman. Multiscale, hybrid mixture theory for swelling systems-I: balance laws. *International Journal of Engineering Science*, 34(2):125–145, 1996.
- [4] J.R. Blake. An active porous medium model for ciliary propulsion. *Journal of theoretical biology*, 64(4):697–701, 1977.
- [5] X.M. Bustamante-Marin and L.E. Ostrowski. Cilia and mucociliary clearance. *Cold Spring Harb Perspect Bio*, 2016.
- [6] X.M. Bustamante-Marin and L.E. Ostrowski. Cilia and mucociliary clearance. *Cold Spring Harbor perspectives in biology*, 9(4):a028241, 2017.
- [7] K. Chamsri. *Modeling the flow of PCL fluid due to the movement of lung cilia*. University of Colorado at Denver, 2012.
- [8] K. Chamsri. N-dimensional Stokes-Brinkman equations using a mixed finite element method. *Australian Journal of Basic and Applied Sciences*, 8:30–36, 2014.
- [9] K. Chamsri and L.S. Bennethum. Permeability of fluid flow through a periodic array of cylinders. *Applied Mathematical Modelling*, 39(1):244–254, 2015.
- [10] Robin Chatelin and Philippe Poncet. A parametric study of mucociliary transport by numerical simulations of 3D non-homogeneous mucus. *Journal of biomechanics*, 49(9):1772–1780, 2016.
- [11] A.P. Corfield. Mucins: a biologically relevant glycan barrier in mucosal protection. *Biochimica et Biophysica Acta (BBA)-General Subjects*, 1850(1):236–252, 2015.
- [12] L. Dormieux, D. Kondo, and F.J. Ulm. *Microporomechanics*. John Wiley & Sons, 2006.
- [13] Fluidics and Biocomplexity Group, Department of Engineering, University of Oxford. The microfluidics of cilia motion home page. <http://www.eng.ox.ac.uk/fbg/cilia.html>, 2010.

This material is reserved for educational use only, not allowed for commercial use.

Forbidden to modify the content, and cite the document when use.

- [14] K. Fujisawa and A. Murakami. Numerical analysis of coupled flows in porous and fluid domains by the Darcy-Brinkman equations. *Soils and foundations*, 58(5):1240–1259, 2018.
- [15] E. Houtmeyers, R. Gosselink, G. Gayan-Ramirez, and M. Decramer. Regulation of mucociliary clearance in health and disease. *European Respiratory Journal*, 13(5):1177–1188, 1999.
- [16] M. Jory, D. Donnarumma, C. Blanc, K. Bellouma, A. Fort, I. Vachier, L. Casanellas, A. Bourdin, and G. Massiera. Mucus from human bronchial epithelial cultures: rheology and adhesion across length scales. *Interface Focus*, 12(6):20220028, 2022.
- [17] T. Kasamwan and K. Wuttanachamsri. Unsteady one-dimensional flow in PCL with Stokes-Brinkman equations. *Phayao Research Confernce*, 2020.
- [18] S.J. Kelly, V. Genevskiy, S. Björklund, J.F. Gonzalez-Martinez, L. Poeschke, M. Schröder, G. Nilius, S. Tatkov, and V. Kocherbitov. Water sorption and structural properties of human airway mucus in health and muco-obstructive diseases. *Biomacromolecules*, 25(3):1578–1591, 2024.
- [19] J. Kori and Pratibha. Numerical simulation of mucus clearance inside lung airways. *Journal of Applied Fluid Mechanics*, 11(5):1163–1171, 2018.
- [20] W.L. Lee, P.G. Jayathilake, Z. Tan, D.V. Le, H.P. Lee, and B.C. Khoo. Muco-ciliary transport: effect of mucus viscosity, cilia beat frequency and cilia density. *Computers & Fluids*, 49(1):214–221, 2011.
- [21] H. Matsui, S.H. Randell, S.W. Peretti, C.W. Davis, R.C. Boucher, et al. Coordinated clearance of periciliary liquid and mucus from airway surfaces. *The Journal of clinical investigation*, 102(6):1125–1131, 1998.
- [22] L.W. Matthews, S. Spector, J. Lemm, and J.L. Potter. Studies on pulmonary secretions: I. The over-all chemical composition of pulmonary secretions from patients with cystic fibrosis, bronchiectasis, and laryngectomy. *American Review of Respiratory Disease*, 88(2):199–204, 1963.
- [23] M.A. Modaresi and E. Shirani. Mucociliary clearance affected by mucus-periciliary interface stimulations using analytical solution during cough and sneeze. *The European Physical Journal Plus*, 138(3):1–18, 2023.
- [24] M. Munkholm and J. Mortensen. Mucociliary clearance: Pathophysiological aspects. *Clinical physiology and functional imaging*, 34(3):171–177, 2014.
- [25] N. Oaungwatcharapran and K. Wuttanachamsri. Solution of flow over periciliary layer using finite difference and n-dimensional Newton-Raphson method. *Journal of Science Ladkrabang*, 29(2):16–30, 2020.

- [26] S. Phaenchat and K. Wuttanachamsri. On the nonlinear Stokes-Brinkman equations for modeling flow in PCL. *The 24th Annual Meeting in Mathematics*, 2019.
- [27] S. Poopra and K. Wuttanachamsri. The velocity of PCL fluid in human lungs with Beaver and Joseph boundary condition by using asymptotic expansion method. *Mathematics*, 7(6):567, 2019.
- [28] S. Poopra and K. Wuttanachamsri. On the asymptotic boundary condition at the free-fluid/porous-medium interface in periciliary layer due to the ciliary movement. *Mathematical Problems in Engineering*, 2022, 2022.
- [29] J.L. Potter, L.W. Matthews, S. Spector, and J. Lemm. Studies on pulmonary secretions: II. Osmolality and the ionic environment of pulmonary secretions from patients with cystic fibrosis, bronchiectasis, and laryngectomy. *American Review of Respiratory Disease*, 96(1):83–87, 1967.
- [30] S. Ren, W. Li, L. Wang, Y. Shi, M. Cai, L. Hao, Z. Luo, J. Niu, W. Xu, and Z. Luo. Numerical analysis of airway mucus clearance effectiveness using assisted coughing techniques. *Scientific reports*, 10(1):2030, 2020.
- [31] J. Schöberl. NETGEN An advancing front 2D/3D-mesh generator based on abstract rules. *Computing and visualization in science*, 1(1):41–52, 1997.
- [32] P. R. Sears, K. Thompson, M. R. Knowles, and C. W. Davis. Human airway ciliary dynamics. *American Journal of Physiology-Lung Cellular and Molecular Physiology*, 304(3):L170–L183, 2013.
- [33] M.H. Sedaghat, S. Sadrizadeh, and O. Abouali. Three-dimensional simulation of mucociliary clearance under the ciliary abnormalities. *Journal of Non-Newtonian Fluid Mechanics*, 316:105029, 2023.
- [34] M.H. Sedaghat, M.M. Shahmardan, M. Norouzi, P.G. Jayathilake, and M. Nazari. Numerical simulation of muco-ciliary clearance: Immersed boundary-lattice Boltzmann method. *Computers & Fluids*, 131:91–101, 2016.
- [35] S. Suankasem, A. Pimkote, I. Thammathon, and K. Wuttanachamsri. Matched asymptotic expansion for PCL fluid due to the movement of lung cilia: part 1. *10th National Science Research Conference*, 2018.
- [36] The Engineering ToolBox (2003). Water-density, specific weight and thermal expansion coefficients. [https://www.engineeringtoolbox.com/water-density-specific-weight-d\\_595.html](https://www.engineeringtoolbox.com/water-density-specific-weight-d_595.html).
- [37] S.M. Vanaki, D. Holmes, S.C. Saha, J. Chen, R.J. Brown, and P.G. Jayathilake. Mucociliary clearance: A review of modeling techniques. *Journal of Biomechanics*, 99, 2020.

- [38] V.S. Verma and V. Rana. Mucus transport in the human lung airways: Effect of porosity parameter and air velocity, 2015.
- [39] T.F. Weinstein and L.S. Bennethum. On the derivation of the transport equation for swelling porous materials with finite deformation. *International journal of engineering science*, 44(18-19):1408–1422, 2006.
- [40] K. Wuttanachamsri. Free interfaces at the tips of the cilia in the one-dimensional periciliary layer. *Mathematics*, 8(11):1961, 2020.
- [41] K. Wuttanachamsri, N. Oangwatcharaparkan, and S. Phaenchat. Wave of cilia affecting the velocity of fluid in periciliary layer. Submitted.
- [42] K. Wuttanachamsri and L. Schreyer. Effects of cilia movement on fluid velocity: II numerical solutions over a fixed domain. *Transport in Porous Media*, 134(2):471–489, 2020.
- [43] K. Wuttanachamsri and L. Schreyer. Effects of cilia movement on fluid velocity: I model of fluid flow due to a moving solid in a porous media framework. *Transport in Porous Media*, 136(2):699–714, 2021.
- [44] L. Xu and Y. Jiang. Mathematical modeling of mucociliary clearance: A mini-review. *Cells*, 8(7):736, 2019.
- [45] D.B. Yeates, N. Aspin, H. Levison, M.T. Jones, and A.C. Bryan. Mucociliary tracheal transport rates in man. *Journal of applied physiology*, 39(3):487–495, 1975.



Appendices

This material is reserved for educational use only, not allowed for commercial use.

Forbidden to modify the content, and cite the document when use.

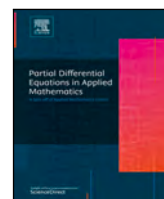
# Appendix A

The research paper



This material is reserved for educational use only, not allowed for commercial use.

Forbidden to modify the content, and cite the document when use.



## Two-dimensional nonlinear Brinkman and steady-state Navier–Stokes equations for fluid flow in PCL

Surachai Phaenchat<sup>\*</sup>, Kanognudge Wuttanachamsri

Department of Mathematics, King Mongkut's Institute of Technology Ladkrabang, Ladkrabang, Bangkok 10520, Thailand

### ARTICLE INFO

#### Keywords:

Steady-state Navier–Stokes equations  
Nonlinear Brinkman equations  
Cilia  
Moving solid Phases  
Mixed finite element method  
Newton's method

### ABSTRACT

To remove mucus from the human body, periciliary layer (PCL) is an important region found in the human respiratory system. When a human inhales strange particles along with air into the body, goblet cells inside the epithelial cells secrete mucus to catch those particles and form a mucus layer on the top of the PCL. Since the velocity of the fluid in the PCL and cilia residing in the PCL affect the movement of mucus, in this work, we apply two-dimensional nonlinear Brinkman and steady-state Navier–Stokes equations to find the velocity of the fluid in the PCL. In the equations, the velocity of cilia is also contributed in the mathematical model which perturbs the fluid movement instead of the pressure gradient. Because bundles of cilia are considered in this work rather than a single cilium, the governing equations are derived from the hybrid mixture theory (HMT) which are the equations in a macroscopic scale. The numerical solutions are obtained by using a mixed finite element method of Taylor–Hood type and Newton's method. We focus on five different angles of cilia that make with the horizontal plane. The velocity of the PCL fluid is presented for each angle. The numerical solutions obtained in this study can be useful in finding the mucus velocity that can help physicians to treat patients who have massive mucus in their lungs.

### 1. Introduction

Mucus is normally found in the human respiratory tract where excess mucus may occur when the body gets sick or breathes in unclean air such as particles in air pollution and smoke. Mucus forms a mucus layer in the respiratory tract and then it moves out of the body by a clearance system.<sup>1</sup> The study of mucus has garnered significant attention because of its essential role in protecting mucosal surfaces and supporting various physiological processes. Fig. 1 shows the platform of mucus clearance. The left side of Fig. 1 shows the respiratory system in the human body including nose, trachea and lungs. The right side of Fig. 1 illustrates a portion of the cross section of the trachea consisting of PCL, mucus layer and epithelial cells. The PCL consists of liquid and solid phases. The liquid phase is a Newtonian fluid known as PCL fluid. The solid phase consists of hair-like structures known as cilia. Mucus is right above the PCL, which is secreted from goblet cells embedded in the epithelial cells. After that, cilia within the PCL beat forward (effective) stroke and backward (recovery) stroke to dump mucus out of the body.

This mechanism is called mucociliary clearance, which had been extensively investigated and well documented.<sup>2–7</sup> For example, Bansil and Turner<sup>8</sup> reviewed the fundamental aspects of mucus including its structure, synthesis, composition, and secretion. Jory et al.<sup>9</sup> studied

mucus in human bronchial epithelial (HBE) cultures and measured the viscoelastic properties of HBE mucus from patients with chronic obstructive pulmonary disease (COPD), and smokers. Kelly et al.<sup>10</sup> investigated water sorption properties of human airway mucus and analyzed the available mucus samples from COPD, cystic fibrosis (CF) patients and healthy individuals. Ren et al.<sup>11</sup> used the Eulerian wall film model to simulate four coughing approaches in COPD and neuromuscular weakening illness to investigate the effects of mucus thickness and viscosity on cough efficiency. Lee et al.<sup>4</sup> studied a two-layer Newtonian fluid model, which consists of an upper mucus layer and a lower periciliary layer. Based on the projection method combined with the Immersed Boundary Method, he simulated the mucociliary transport process with the prescribed velocity of the beating cilia. For the motion of the cilia, Ding et al.<sup>12</sup> and Gue et al.<sup>13</sup> examined the cilia beating patterns in three different situations: synchronized beating, symplectic wave, and antiplectic wave in different approaches. Sear<sup>14</sup> studied ciliary motion by using video microscopy to record planar ciliary motions that could be used to validate mathematical models or investigate ciliary function such as in primary ciliary dyskinesia (PCD). Xu and Jiang<sup>15</sup> investigated the cilia motion with the velocity and height differences by using a rod-propel-fluid model to examine

<sup>\*</sup> Corresponding author.

E-mail addresses: [62605007@kmitl.ac.th](mailto:62605007@kmitl.ac.th) (S. Phaenchat), [kanognudge.wu@kmitl.ac.th](mailto:kanognudge.wu@kmitl.ac.th) (K. Wuttanachamsri).

<https://doi.org/10.1016/j.padiff.2024.100961>

Received 23 October 2023; Received in revised form 1 September 2024; Accepted 9 October 2024

Available online 18 October 2024

2666-8181/© 2024 The Authors. Published by Elsevier B.V. This is an open access article under the CC BY-NC-ND license (<http://creativecommons.org/licenses/by-nc-nd/4.0/>).

This material is reserved for educational use only, not allowed for commercial use.

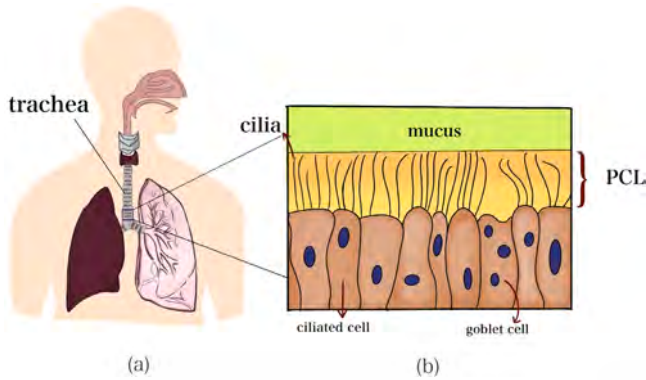


Fig. 1. (a) the human respiratory system (b) a sector of the cross-section of the trachea which consists of the mucus layer, the periciliary layer (PCL), the cilia, ciliated cells, and goblet cells.

the effects of the cilia density, beating frequency, metachronal wavelength, and the extending height of the beating cilia. Jayathilak et al.<sup>16</sup> investigated that the PCL velocity was proportionally dependent on the cilia beat frequency. Wei et al.<sup>17</sup> examined the velocity of the fluid flow in the PCL around the beating of cilia by using the Navier–Stokes equations. Vanaki et al.<sup>18</sup> studied the flow of PCL fluid when the respiratory disease influenced the cilia to have low beating frequency, abnormal beating pattern and reduced ciliary density. The disease also effected epithelium patchiness due to missing cilia in the PCL transport. They used the immersed boundary (IB) method combined with the finite-difference projection method. In this work, we study the effect of the ciliary movement on the velocity of the PCL fluid. For the forward stroke, we assume that the cilia make angles with the horizontal plane, which start from 90° and lean forward to 40°. We suppose that cilia have the highest velocity at the angle  $\theta = 90^\circ$  and bend down gradually to the angle 50° and stop beating at the angle  $\theta = 40^\circ$ .<sup>14</sup>

Fig. 2 illustrates the PCL where the left-hand side of Fig. 2 shows the cilia perpendicular to the horizontal plane and the right-hand side of Fig. 2 shows the cilia make the angle  $\theta$  with the horizontal plane. The layer consisting of the cilia and the PCL fluid is considered as a porous medium,  $\Omega_1$ . When the cilia bend down, there exists a free-fluid region above the porous medium. We call the domain  $\Omega_2$ . The variable  $b$  at the vertical line is the height of the domain  $\Omega_1$  which depends on the angle  $\theta$  that the cilia make with the horizontal plane. The unit of the height is micrometer ( $\mu\text{m}$ ). The parameter  $\xi$  is the length of cilia which is about  $7.5 \mu\text{m}$ .<sup>19</sup> In this research, we study the fluid flow in both  $\Omega_1$  and  $\Omega_2$  regions. Because a bundle of cilia is inspected, the equations used to determine the velocity of the PCL fluid are in the macroscopic scale. The equations are upscaled by using the Hybrid Mixer Theory (HMT), which upscales the equations from a microscale equation to a macroscale equation.<sup>20,21</sup> Several mathematical macroscale models were used to study the fluid flow in the free-fluid region and porous medium. Hwang and Advani<sup>22</sup> used Stokes–Brinkman equations for flow in a parallel channel over a porous medium to predict the effective permeability of dual scale fibrous media by using finite element method. Fujisawa and Murakami<sup>23</sup> studied the flow in porous medium and free-fluid domains by using Darcy–Brinkman equations with a continuous model. Suankasem et al.<sup>24</sup> and Poopra and Wuttanachamsri<sup>25,26</sup> applied the asymptotic expansion method to one-dimensional macroscale Stokes–Brinkman equations to find the velocities of the PCL fluid in different approaches. Chen et al.<sup>27</sup> derived asymptotic solutions for Stokes–Darcy and Stokes–Brinkman equations in free flow and porous medium for one-dimensional and quasi-two-dimensional cases with different interface conditions: the Beavers–Joseph, Beavers–Joseph–Saffman–Jones, zero tangential velocity, and free-slip interface conditions. Phaenchat and Wuttanachamsri<sup>28</sup> discretized one-dimensional

macroscale nonlinear Stokes–Brinkman equation by using Galerkin finite element method combined with the classical linearization method. Kasamwan and Wuttanachamsri<sup>29</sup> found the velocities of the PCL fluid using one-dimensional macroscale unsteady Stokes–Brinkman equations by using a finite element method with an isoparametric linear element combined with the Crank–Nicolson method. Chamsri<sup>30</sup> discretized  $n$ -dimensional macroscale Stokes–Brinkman equations by using a mixed-finite element method which was employed to find the velocity of the PCL fluid in Ref. 31. Oangwatcharapran and Wuttanachamsri<sup>32</sup> provided the velocity of the PCL fluid using one-dimensional Navier–Stokes–Brinkman equations. Wuttanachamsri<sup>33</sup> studied the free interfaces at the tips of cilia using a macroscale Brinkman equation. Most of the macroscale equations are one-dimensional linear equations and only slow flows are considered in their studies. However, sometimes the fluid flow is nonlinear and perturbed by unusual environments. So, in this research, we focus on the two-dimensional macroscale nonlinear Brinkman equation for the porous domain,  $\Omega_1$ , and the steady-state Navier–Stokes equations for the free-fluid region,  $\Omega_2$ , which are provided in Section 2. A mixed-finite element method of Taylor–Hood type combined with Newton’s method is applied to the equations in Sections 3 and 4. The numerical solutions of the velocities of the PCL fluid for 5 different angles are provided in Section 5. The conclusions are summarized in Section 6.

## 2. Mathematical models

In this section, we present the governing equations used in this work, which are the two-dimensional nonlinear Brinkman equation upscaled from Hybrid Mixture Theory (HMT)<sup>20,21</sup> and steady-state Navier–Stokes equations.<sup>21</sup> The HMT is an upscaling method used to derive equations for multiphase materials, such as solid and liquid phases. The process of the HMT is to apply the averaging theorem to the conservation equation to upscale a microscale equation to a macroscale equation.<sup>20,21</sup> For the conservation of momentum, the macroscale equation is<sup>21</sup>

$$\epsilon^\alpha \rho^\alpha \frac{D^\alpha \mathbf{v}^\alpha}{Dt} - \nabla \cdot (\epsilon^\alpha \mathbf{t}^\alpha) - \epsilon^\alpha \rho^\alpha \mathbf{g}^\alpha = \sum_{\alpha \neq \beta} \epsilon^\alpha \rho^\alpha \hat{\mathbf{T}}_\beta^\alpha \quad (2.1)$$

where the variable  $\epsilon^\alpha$  is the volume fraction of phase  $\alpha$ ,  $\rho^\alpha$  and  $\mathbf{v}^\alpha$  are the macroscale density and velocity of phase  $\alpha$ ,  $\frac{D^\alpha}{Dt} = \frac{\partial}{\partial t} + \mathbf{v}^\alpha \cdot \nabla$  is the macroscale material time derivative,  $\mathbf{g}^\alpha$  is the macroscale gravitational vector,  $\mathbf{t}^\alpha$  is the macroscale Cauchy stress tensor and  $\hat{\mathbf{T}}_\beta^\alpha$  is the rate of exchange of momentum from  $\beta$  to  $\alpha$ . Since in our study, we have only solid (cilia) and liquid (PCL fluid) phases, we replace  $\alpha$  by  $l$  which means the liquid phase and substitute  $\beta$  by  $s$  which is the solid phase. For the stress tensor  $\mathbf{t}^\alpha$ , the constitutive equation

$$\mathbf{t}^l = -p\mathbf{I} + 2\mu\mathbf{d}^l, \quad (2.2)$$

is used in Eq. (2.1), where the rate of deformation for the liquid phase  $\mathbf{d}^l$  is  $0.5(\nabla \mathbf{v}^l + (\nabla \mathbf{v}^l)^T)$ ,  $\mu$  is the dynamic viscosity and  $p$  is pressure. For the rate of exchange  $\hat{\mathbf{T}}_s^l$ , it is linearized around the velocities,  $\mathbf{v}^l - \mathbf{v}^s$ , where  $\mathbf{v}^l$  and  $\mathbf{v}^s$  are the velocities of the fluid and solid phases, respectively,<sup>34,35</sup> giving the result:

$$\epsilon^l \rho^l \hat{\mathbf{T}}_s^l = p \nabla \epsilon^l - \epsilon^l \mathbf{R} \cdot (\mathbf{v}^l - \mathbf{v}^s), \quad (2.3)$$

where  $\mathbf{R}$  is the second-order tensor obtained from the linearization. Let  $\mathbf{R} = \mu \epsilon^l \mathbf{k}^{-1}$ , where  $\mathbf{k}^{-1}$  is the inverse of the permeability tensor, and substituting Eqs. (2.2) and (2.3) into Eq. (2.1), we have the conservation of momentum for the unsteady nonlinear Brinkman equation<sup>21</sup>

$$\rho \frac{D\mathbf{v}^l}{Dt} + \nabla p - \frac{\mu}{\epsilon^l} \nabla \cdot (2\epsilon^l \mathbf{d}^l) - \rho \mathbf{g} = -\mu \epsilon^l \mathbf{k}^{-1} \cdot (\mathbf{v}^l - \mathbf{v}^s). \quad (2.4)$$

In this study, the PCL fluid flows through the cilia and is incompressible with slow flow. To understand the behavior of fluid flow in the PCL, in this work, we concentrate on the steady-state flow condition. Therefore, the momentum equation used in this study is as follows.

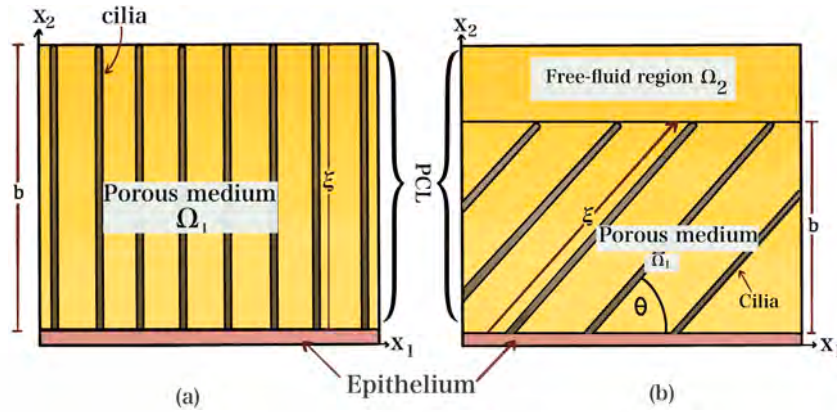


Fig. 2. The cartoon picture of the PCL domain: (a) the cilia are perpendicular to the horizontal plane. (b) the cilia make an angle  $\theta$  with the horizontal plane.

$$\rho(\mathbf{v}^l \cdot \nabla \mathbf{v}^l) + \nabla p - \frac{\mu}{\epsilon^l} (\Delta \epsilon^l \mathbf{v}^l + \nabla (\nabla \cdot \epsilon^l \mathbf{v}^l)) - \rho \mathbf{g} = -\mu \mathbf{k}^{-1} \cdot (\epsilon^l \mathbf{v}^l - \epsilon^l \mathbf{v}^s). \quad (2.5)$$

$$\frac{\partial v_j}{\partial x_j} = f, \quad (2.15)$$

Similarly, the macroscale continuity equation is derived by applying the HMT to the conservation of mass. The macroscale equation is<sup>21,36</sup>

$$\frac{\partial(\epsilon^\alpha \rho^\alpha)}{\partial t} + \nabla \cdot (\epsilon^\alpha \rho^\alpha \mathbf{v}^\alpha) = \sum_{\beta \neq \alpha} \epsilon^\alpha \rho^\alpha \hat{\epsilon}_{\beta\alpha}^\alpha, \quad (2.6)$$

where the variable  $\hat{\epsilon}_{\beta\alpha}^\alpha$  is the rate of exchange of mass from phase  $\beta$  to phase  $\alpha$ . We assume that there is no mass exchanged between the liquid and solid phases and the liquid and solid phases are incompressible. Then Eq. (2.6) for the solid and liquid phases can be written as follows<sup>21</sup>

$$\frac{D^l \epsilon^l}{Dt} + \epsilon^l \nabla \cdot \mathbf{v}^l = 0, \quad (2.7)$$

$$\frac{D^s \epsilon^s}{Dt} + \epsilon^s \nabla \cdot \mathbf{v}^s = 0. \quad (2.8)$$

We use the definition of the volume of the solid phase  $\epsilon^s = 1 - \epsilon^l$  and the definition of the material time derivative to Eqs. (2.7) and (2.8). Then, adding the two equations together yields<sup>21</sup>

$$\frac{D^s \epsilon^l}{Dt} + (1 - \epsilon^l) \nabla \cdot \epsilon^l (\mathbf{v}^l - \mathbf{v}^s) = 0, \quad (2.9)$$

which is the continuity equation in the macroscopic scale. Rearranging Eq. (2.9), we have

$$\epsilon^l \nabla \cdot \mathbf{v}^l = f, \quad (2.10)$$

where the solid-phase porous flow rate associated with the cilia  $f = -\frac{\epsilon^l}{(1-\epsilon^l)} + \nabla \cdot \epsilon^l \mathbf{v}^s$  and the material time derivative of the porosity with respect to the solid phase  $\epsilon^l = \frac{D^s \epsilon^l}{Dt} = \frac{\partial \epsilon^l}{\partial t} + \mathbf{v}^s \cdot \nabla \epsilon^l$ . Define  $\mathbf{v} = \epsilon^l \mathbf{v}^l$ . In this work, we suppose that the porosity  $\epsilon^l$  is a constant for a fixed domain because the cilia make only one angle  $\theta$  to the horizontal plane per each calculation. Then Eqs. (2.5) and (2.10) become

$$\frac{\rho}{(\epsilon^l)^2} (\mathbf{v} \cdot \nabla \mathbf{v}) + \nabla p - \frac{\mu}{\epsilon^l} (\Delta \mathbf{v} + \nabla (\nabla \cdot \mathbf{v})) - \rho \mathbf{g} = -\mu \mathbf{k}^{-1} \cdot (\mathbf{v} - \epsilon^l \mathbf{v}^s), \quad (2.11)$$

$$\nabla \cdot \mathbf{v} = f. \quad (2.12)$$

Substituting Eq. (2.12) into Eq. (2.11) yields

$$\frac{\rho}{(\epsilon^l)^2} (\mathbf{v} \cdot \nabla \mathbf{v}) + \nabla p - \frac{\mu}{\epsilon^l} (\Delta \mathbf{v} + \nabla f) - \rho \mathbf{g} = -\mu \mathbf{k}^{-1} \cdot (\mathbf{v} - \epsilon^l \mathbf{v}^s), \quad (2.13)$$

which is named PCL combined fluid–solid-phase porous governing equation of porous medium. For a two-dimensional domain, let  $\mathbf{v} = (v_1, v_2)$  and  $\mathbf{v}^s = (v_1^s, v_2^s)$ ,  $\mathbf{g} = (g_1, g_2)$  and  $\mathbf{k}^{-1} = \begin{bmatrix} k_{11}^{-1} & k_{12}^{-1} \\ k_{21}^{-1} & k_{22}^{-1} \end{bmatrix}$ . Therefore, Eqs. (2.12) and (2.13) can be rewritten in index notation as

$$\frac{\rho}{(\epsilon^l)^2} \left( v_j \frac{\partial v_i}{\partial x_j} \right) + \frac{\partial p}{\partial x_i} - \frac{\mu}{\epsilon^l} \left( \frac{\partial^2 v_i}{\partial x_j^2} + \frac{\partial f}{\partial x_i} \right) - \rho g_i = -\mu k_{ij}^{-1} (v_j - \epsilon^l v_j^s), \quad (2.14)$$

The repeated index  $j$  means the summation, where  $i, j = 1, 2$ . We rearrange Eqs. (2.14) and (2.15) by moving unknown variables,  $\mathbf{v}$  and  $p$ , to the left-hand side and known variables to the right-hand side. Define  $L_0^2(\Omega) = \{q \in L^2(\Omega) : \int_\Omega q d\Omega = 0\}$ . For a fixed domain  $\Omega_1$ , we find  $\mathbf{v} \in C^0(\bar{\Omega}_1) \cap C^2(\Omega_1)$  and  $p \in L_0^2(\Omega_1)$  such that

$$\frac{\rho}{(\epsilon^l)^2} \left( v_j \frac{\partial v_i}{\partial x_j} \right) - \frac{\mu}{\epsilon^l} \frac{\partial^2 v_i}{\partial x_j^2} + \mu k_{ij}^{-1} v_j + \frac{\partial p}{\partial x_i} = \rho g_i + \frac{\mu}{\epsilon^l} \frac{\partial f}{\partial x_i} + \mu \epsilon^l k_{ij}^{-1} v_j^s, \quad (2.16)$$

$$\frac{\partial v_j}{\partial x_j} = f, \quad (2.17)$$

This concludes the derivation of the two-dimensional nonlinear Brinkman equations that are employed in the porous domain,  $\Omega_1$ . Next, we provide the two-dimensional steady-state Navier–Stokes equations that are used in the free-fluid region,  $\Omega_2$ . For a fixed domain  $\Omega_2$ , we find  $\mathbf{v} \in C^0(\bar{\Omega}_2) \cap C^2(\Omega_2)$  and  $p \in L_0^2(\Omega_2)$  such that

$$\rho \left( v_j \frac{\partial v_i}{\partial x_j} \right) - \mu \frac{\partial^2 v_i}{\partial x_j^2} + \frac{\partial p}{\partial x_i} = \rho g_i, \quad (2.18)$$

$$\frac{\partial v_j}{\partial x_j} = 0. \quad (2.19)$$

Notice that there are no solid phases in  $\Omega_2$  and  $\epsilon^l = 1$ . Then, the inverse of the permeability,  $\mathbf{k}^{-1}$ , and  $f$  are not present in both momentum and continuity equations.

Figs. 3(a) and 3(b) illustrate the boundaries when the cilia are perpendicular and make angle  $\theta$  less than  $90^\circ$  to the horizontal plane, respectively. The variable  $y_s$  is the dimensionless height of the porous medium. That is  $y_s = b/\xi$ . Then  $y_s$  is one for the perpendicular case. In this study, we use dimensionless numerical domain. That is the size of the domain  $\Omega_1$  is  $[0, 1] \times [0, y_s]$ . Similarly, the numerical domain  $\Omega_2$  has the size  $[0, 1] \times [y_s, 1]$ . We define domain  $\Omega = \Omega_1 \cup \Omega_2$ . The variables  $\Gamma_i, i = 1, 2, \dots, 7$  are the boundaries around  $\Omega$  and also at the free-fluid/porous-medium interface. For the boundary conditions used in this paper, we first assume that there is no velocity at the ciliary rootlets in domain  $\Omega_1$ . The rate of change of velocities with respect to  $x_2$  is zero at the top of domain  $\Omega_2$  and also at  $\Gamma_4$ , see Fig. 3. For the case that the cilia are perpendicular to the horizontal plane, there is no velocity in  $x_2$ -direction at the top of the domain  $\Omega_1$ . The illustration of the distribution of the velocities on the cilia and on the free-fluid domain including the velocity profile corresponding to the boundary condition is provided in Fig. 4. Fig. 4(a) depicts the distributions and the velocity profile of  $v_1$  when the cilia are perpendicular to the horizontal plane. That is no velocity at the bottom of the domain  $\Omega_1$ . The velocity  $\mathbf{v} = v_1$  and  $v_1$  is maximum at  $\Gamma_4$ . So the lengths of the quivers are zero at the rootlet and increase to the highest magnitude at  $\Gamma_4$ . Since the cilia move

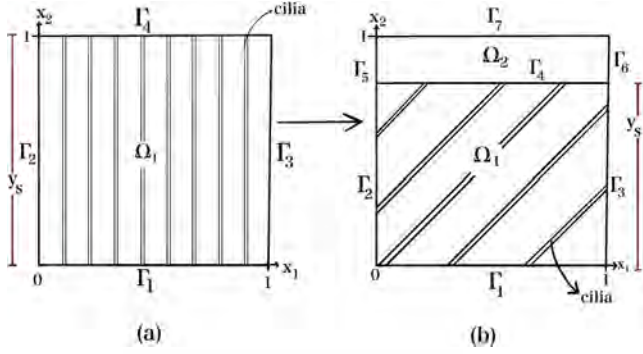


Fig. 3. Numerical domains and boundaries of the problem. (a) The cilia are perpendicular to the horizontal plane. (b) The cilia make angle  $\theta$  less than  $90^\circ$  to the horizontal plane.

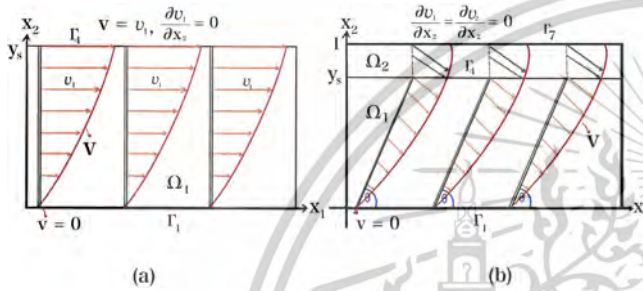


Fig. 4. Distribution of the velocities on the cilia. (a) The cilia are perpendicular to the horizontal plane. (b) The cilia make angle  $\theta$  less than  $90^\circ$  to the horizontal plane and distribution of the velocities on the free-fluid region.

from left to right, the direction of the flow goes from the left to the right. Fig. 4(b) illustrates the velocity distributions and profiles when the cilia make the angle, less than  $90^\circ$ , to the horizontal plane. At  $\Gamma_1$ , the boundary condition is the same as the perpendicular case, which is zero. The velocity is continuous at  $\Gamma_4$ . At  $\Gamma_7$ , the rate of change of the velocities with respect to  $x_2$  is zero. That is maximum magnitudes of  $v_1$  and  $v_2$  occur at  $\Gamma_7$ . So the lengths of the quivers of the velocity  $\mathbf{v}$  are zero at the rootlet and increase continuously to the greatest value at  $\Gamma_7$ . The boundary conditions are concluded as follows.

$$\begin{aligned}
 v_i &= 0, \quad \text{for } i = 1, 2, \text{ at } \Gamma_1, \\
 \frac{\partial v_i}{\partial x_2} &= 0, \quad \text{for } i = 1, 2, \text{ at } \Gamma_7, \\
 \frac{\partial v_1}{\partial x_2} &= 0, \quad \text{at } \Gamma_4 \text{ for the angle } \theta = 90^\circ, \\
 v_2 &= 0, \quad \text{at } \Gamma_4 \text{ for the angle } \theta = 90^\circ.
 \end{aligned}
 \tag{2.20}$$

These boundary conditions provide that the velocities  $v_1$  and  $v_2$  are zero at the bottom of the porous domain. The velocities  $v_1$  and  $v_2$  do not vary in the  $x_2$  direction at the top of the free-fluid region. When the cilia are perpendicular to the horizontal plane ( $\theta = 90^\circ$ ), the velocity  $v_1$  does not change in the  $x_2$  direction and the velocity  $v_2$  is zero at the top of the porous region.

Because the velocities at the boundaries  $\Gamma_2, \Gamma_3, \Gamma_5$  and  $\Gamma_6$  are unknown, they are moved to the left-hand side of the Eqs. (3.10) or (3.17) written below. So after the calculation, we obtain the velocities at these boundaries. In this work, we do not place the boundary condition for the pressure but we use the normalization  $\int_{\Omega} p \, d\Omega = 0$  because our system of equations determines the pressure up to an additive constant.<sup>37</sup> We now have two-dimensional governing equations including boundary conditions that is discretized in the next section.

### 3. Model discretization

The mathematical models provided in Section 2 are discretized in this section using a mixed finite element method of Taylor–Hood type. Let  $\Omega_1^e$  and  $\Omega_2^e$  be the element domains in  $\Omega_1$  and  $\Omega_2$ , respectively, and  $\Omega_1 = \bigcup_e \Omega_1^e$  and  $\Omega_2 = \bigcup_e \Omega_2^e$ .

For the finite element approximation, we approximate the dependent variables  $(v_i, p) \in V_h \times P_h$ , where  $V_h$  and  $P_h$  are finite-dimensional subspaces of  $H^1(\Omega)$  and  $L_0^2(\Omega) = \{p \in L^2(\Omega) : \int_{\Omega} p \, d\Omega = 0\}$ . The variables  $v_i$  and  $p$  are approximated by expansions of the form

$$v_i(\mathbf{x}) = \sum_{k=1}^K \psi_k(\mathbf{x}) v_i^k = \boldsymbol{\psi}^T \mathbf{V}_i, \quad i = 1, 2 \tag{3.2}$$

$$p(\mathbf{x}) = \sum_{d=1}^D \phi_d(\mathbf{x}) p_d = \boldsymbol{\phi}^T \mathbf{P}, \tag{3.3}$$

where  $\boldsymbol{\psi}$  and  $\boldsymbol{\phi}$  are the vectors of shape functions,  $\mathbf{V}_i$  and  $\mathbf{P}$  are vectors of the velocities and pressure, respectively, and the superscript  $T$  represents the transpose operation. The integers  $K$  and  $D$  are the number of local degrees of freedom determined by the shape functions. In this work, we choose the shape functions for the velocity and pressure to be piecewise quadratic and linear polynomials on triangular elements, respectively. Therefore  $K = 6$  and  $D = 3$ . The approximation of the velocity of cilia can be written as

$$v_j^s(\mathbf{x}) = \sum_{k=1}^K \psi_k(\mathbf{x}) (v_j^s)^k = \boldsymbol{\psi}^T \mathbf{V}_j^s, \quad j = 1, 2. \tag{3.4}$$

The weak formulation of the mathematical models over the element domain  $\Omega_1^e$  and  $\Omega_2^e$  are derived by multiplying Eq. (2.16) by shape functions  $w$  and Eq. (2.17) by the shape functions  $Q$  and then integrating over the domain  $\Omega_1^e$ . Therefore, Eqs. (2.16) and (2.17) become

$$\begin{aligned}
 \int_{\Omega_1^e} \left[ \frac{\rho}{(\epsilon^l)^2} \left( w v_j \frac{\partial v_i}{\partial x_j} \right) - \frac{\mu}{\epsilon^l} \left( w \frac{\partial^2 v_i}{\partial x_j^2} \right) + \mu k_{ij}^{-1} w v_j + w \frac{\partial p}{\partial x_i} \right] d\Omega_1^e \\
 = \int_{\Omega_1^e} \left[ \rho g_i w + \frac{\mu}{\epsilon^l} \left( w \frac{\partial f}{\partial x_i} \right) + \mu \epsilon^l k_{ij}^{-1} w v_j^s \right] d\Omega_1^e,
 \end{aligned}
 \tag{3.5}$$

$$\int_{\Omega_1^e} Q \frac{\partial v_j}{\partial x_j} \, d\Omega_1^e = \int_{\Omega_1^e} Q f \, d\Omega_1^e. \tag{3.6}$$

Next, we apply Green's identity to the second and fourth terms in Eq. (3.5) and also the source term  $\frac{\mu}{\epsilon^l} \left( w \frac{\partial f}{\partial x_i} \right)$ . Then we have

$$\begin{aligned}
 \int_{\Omega_1^e} \left[ \frac{\rho}{(\epsilon^l)^2} \left( w v_j \frac{\partial v_i}{\partial x_j} \right) + \frac{\mu}{\epsilon^l} \frac{\partial w}{\partial x_j} \frac{\partial v_i}{\partial x_j} + \mu k_{ij}^{-1} w v_j - \frac{\partial w}{\partial x_i} p \right] d\Omega_1^e \\
 = \int_{\Omega_1^e} \left[ \rho g_i w - \frac{\mu}{\epsilon^l} \frac{\partial w}{\partial x_i} f + \mu \epsilon^l k_{ij}^{-1} w v_j^s \right] d\Omega_1^e \\
 + \int_{\Gamma_p^e} \left[ \frac{\mu}{\epsilon^l} \left( w \frac{\partial v_i}{\partial x_j} n_j \right) - w p n_i + \frac{\mu}{\epsilon^l} w f n_i \right] d\Gamma_p^e,
 \end{aligned}
 \tag{3.7}$$

where  $n_i, i = 1, 2$ , is an outward unit normal vector of each element and  $\Gamma_p^e$  is the boundary of the element in the porous domain. For the weak formulation over the element domain  $\Omega_2^e$  of the free-fluid region, applying the same process as above, we obtain

$$\int_{\Omega_2^e} \left[ \rho w v_j \frac{\partial v_i}{\partial x_j} + \mu \frac{\partial w}{\partial x_j} \frac{\partial v_i}{\partial x_j} - \frac{\partial w}{\partial x_i} p \right] d\Omega_2^e \tag{3.8}$$

$$= \int_{\Omega_2^e} \rho g_i w \, d\Omega_2^e + \int_{\Gamma_f^e} \left[ \mu w \frac{\partial v_i}{\partial x_j} n_j - w p n_i \right] d\Gamma_f^e,$$

$$\int_{\Omega_2^e} Q \frac{\partial v_j}{\partial x_j} \, d\Omega_2^e = 0, \tag{3.9}$$

where  $\Gamma_f^e$  is the boundary of the element in the free-fluid region. Substituting Eqs. (3.2)–(3.4) into Eqs. (3.6) and (3.7), we have the element matrix form as follows.

$$\begin{bmatrix} N + A_{11} + A_{22} + \mu k_{11}^{-1} B & \mu k_{12}^{-1} B & -Z_1^T \\ \mu k_{21}^{-1} B & N + A_{11} + A_{22} + \mu k_{22}^{-1} B & -Z_2^T \\ Z_1 & Z_2 & \mathbf{0} \end{bmatrix} \begin{Bmatrix} \mathbf{V}_1 \\ \mathbf{V}_2 \\ \mathbf{P} \end{Bmatrix} = \begin{Bmatrix} \bar{F}_1 \\ \bar{F}_2 \\ \bar{E} \end{Bmatrix}, \tag{3.10}$$

where the coefficients in the element matrix are defined as

$$N = \frac{\rho}{(\epsilon^l)^2} C_j(\mathbf{V}_j), \tag{3.11}$$

$$C_i(\mathbf{V}_j) = \int_{\Omega_1^e} \psi(\psi^T \mathbf{V}_j) \frac{\partial \psi^T}{\partial x_i} d\Omega_1^e, \quad B = \int_{\Omega_1^e} \psi \psi^T d\Omega_1^e, \tag{3.12}$$

$$A_{ij} = \frac{\mu}{\epsilon^l} \int_{\Omega_1^e} \frac{\partial \psi}{\partial x_i} \frac{\partial \psi^T}{\partial x_j} d\Omega_1^e, \quad Z_i = \int_{\Omega_1^e} \phi \frac{\partial \psi^T}{\partial x_i} d\Omega_1^e,$$

$$\begin{aligned} F_i &= \rho g_i \int_{\Omega_1^e} \psi d\Omega_1^e - \frac{\mu}{\epsilon^l} \int_{\Omega_1^e} \frac{\partial \psi}{\partial x_i} f d\Omega_1^e + \mu \epsilon^l k_{ij}^{-1} \int_{\Omega_1^e} \psi \psi^T \mathbf{V}_j^s d\Omega_1^e \\ &+ \frac{\mu}{\epsilon^l} \int_{\Gamma_p^e} \left( \psi \frac{\partial \psi^T}{\partial x_j} n_j \right) d\Gamma_p^e \mathbf{V}_i - \int_{\Gamma_p^e} \psi \phi^T n_i d\Gamma_p^e \mathbf{P} + \frac{\mu}{\epsilon^l} \int_{\Gamma_p^e} \psi f n_i d\Gamma_p^e, \end{aligned} \tag{3.13}$$

$$E = \int_{\Omega_1^e} \phi f d\Omega_1^e, \tag{3.14}$$

where  $i, j = 1, 2$ . The repeated  $j$  index refers to the summation over  $j, j = 1, 2$ . We next provide the element matrix for the free-fluid region,  $\Omega_2$ . Substituting Eqs. (3.2)–(3.4) into Eqs. (3.8) and (3.9), we have

$$\begin{aligned} \rho \int_{\Omega_2^e} \psi(\psi^T \mathbf{V}_j) \frac{\partial \psi^T}{\partial x_j} d\Omega_2^e \mathbf{V}_i + \mu \int_{\Omega_2^e} \frac{\partial \psi}{\partial x_j} \frac{\partial \psi^T}{\partial x_j} d\Omega_2^e \mathbf{V}_i - \int_{\Omega_2^e} \frac{\partial \psi}{\partial x_i} \phi^T d\Omega_2^e \mathbf{P} \\ = \rho g_i \int_{\Omega_2^e} \psi d\Omega_2^e + \mu \int_{\Gamma_f^e} \psi \frac{\partial \psi^T}{\partial x_j} n_j d\Gamma_f^e \mathbf{V}_i - \int_{\Gamma_f^e} \psi \phi^T n_i d\Gamma_f^e \mathbf{P}, \end{aligned} \tag{3.15}$$

$$\int_{\Omega_2^e} \phi \frac{\partial \psi^T}{\partial x_j} d\Omega_2^e \mathbf{V}_j = 0. \tag{3.16}$$

Therefore, the element matrix form of Eqs. (3.15) and (3.16) is

$$\begin{bmatrix} \tilde{N} + \tilde{A}_{11} + \tilde{A}_{22} & \mathbf{0} & -Z_1^T \\ \mathbf{0} & \tilde{N} + \tilde{A}_{11} + \tilde{A}_{22} & -Z_2^T \\ Z_1 & Z_2 & \mathbf{0} \end{bmatrix} \begin{Bmatrix} \mathbf{V}_1 \\ \mathbf{V}_2 \\ \mathbf{P} \end{Bmatrix} = \begin{Bmatrix} \tilde{F}_1 \\ \tilde{F}_2 \\ \mathbf{0} \end{Bmatrix}, \tag{3.17}$$

where

$$\tilde{F}_i = \rho g_i \int_{\Omega_2^e} \psi d\Omega_2^e + \mu \int_{\Gamma_f^e} \psi \frac{\partial \psi^T}{\partial x_j} n_j d\Gamma_f^e \mathbf{V}_i - \int_{\Gamma_f^e} \psi \phi^T n_i d\Gamma_f^e \mathbf{P}, \tag{3.18}$$

$$\tilde{A}_{ij} = \mu \int_{\Omega_2^e} \frac{\partial \psi}{\partial x_i} \frac{\partial \psi^T}{\partial x_j} d\Omega_2^e, \tag{3.19}$$

$$\tilde{N} = \rho C_j(\mathbf{V}_j). \tag{3.20}$$

We now have the element matrix for both domains  $\Omega_1$  and  $\Omega_2$ . To be able to solve the nonlinear term  $N$  and  $\tilde{N}$  in Eqs. (3.10) and (3.17), we write both Eqs. (3.10) and (3.17) into a general form. That is

$$\bar{K}(\bar{V})\bar{V} = \bar{F}, \tag{3.21}$$

where  $\bar{K}(\bar{V})$  is the coefficient matrix in Eqs. (3.10) or (3.17),  $\bar{V}$  is the vector of the unknown and  $\bar{F}$  is the right-hand side vector. If the element that we consider is in  $\Omega_1$ , we use  $\bar{K}(\bar{V})$  in Eq. (3.10). If the element is in  $\Omega_2$ , we use  $\bar{K}(\bar{V})$  in Eq. (3.17), as well as the vectors  $\bar{V}$  and  $\bar{F}$ . Although Eqs. (3.10) and (3.17) are written in the same form, Eq. (3.21), applying these equations in different domains the component of Eq. (3.21) varies accordingly in Eqs. (3.10) and (3.17). The Eq. (3.21) is solved by using Newton's method provided in the next section.

**Table 1**  
The values of  $y_s$  for each angle.

$\theta$	$y_s$
50°	0.7660
60°	0.8660
70°	0.9397
80°	0.9848
90°	1

#### 4. Newton's method

In this section, we present the Newton's method which is an iterative method for solving nonlinear equations. Define

$$R(\bar{V}) = \bar{K}(\bar{V})\bar{V} - \bar{F} = \bar{0}. \tag{4.1}$$

To solve Eq. (4.1) iteratively, we approximate  $R(\bar{V})$  around  $\bar{V}^n$  as follows

$$R(\bar{V}) \approx R(\bar{V}^n) + \frac{\partial R}{\partial \bar{V}} \Big|_{\bar{V}^n} \Delta \bar{V} + O(\Delta \bar{V})^2, \tag{4.2}$$

where  $\Delta \bar{V} = (\bar{V} - \bar{V}^n)$ , and  $\bar{V}^n$  is the known vectors at the current iterative. Substituting Eq. (4.2) into Eq. (4.1), we obtain

$$\bar{0} = R(\bar{V}^n) + \frac{\partial R}{\partial \bar{V}} \Big|_{\bar{V}^n} \Delta \bar{V} + O(\Delta \bar{V})^2. \tag{4.3}$$

Omitting the  $O(\Delta \bar{V})^2$  term and updating  $\bar{V}$  to be  $\bar{V}^{n+1}$  yield

$$R(\bar{V}^{n+1}) = - \frac{\partial R}{\partial \bar{V}} \Big|_{\bar{V}^n} (\bar{V}^{n+1} - \bar{V}^n) \equiv -J(\bar{V}^n)(\bar{V}^{n+1} - \bar{V}^n), \tag{4.4}$$

where

$$J = \frac{\partial R}{\partial \bar{V}} \Big|_{\bar{V}^n} \tag{4.5}$$

is the Jacobian matrix. Therefore

$$\bar{V}^{n+1} = \bar{V}^n - J^{-1}(\bar{V}^n)R(\bar{V}^n), \tag{4.6}$$

which will be used to find the numerical results presented in Section 5.

#### 5. Numerical solutions

The numerical solutions obtained from the mixed finite element approach of Taylor–Hood type and Newton's method are provided in this section. In this study, we let the velocity of cilia be zero at the base of the domain  $\Omega_1$ , the velocity increases along the cilia and the velocity is maximum at the tip of the cilia.

Since only the forward stroke is considered, we assume that the cilia start at 90° with maximum velocity and the velocity decreases with decreasing angle  $\theta$ . When the angle decreases to less than 90°, the numerical domain consists of two regions: the porous medium,  $\Omega_1$ , and the free-fluid region,  $\Omega_2$ , (see Fig. 2). The line at  $x_2 = y_s$  is separate between the domains  $\Omega_1$  and  $\Omega_2$ . Table 1 shows the values of  $y_s$  for each angle  $\theta$ . So the velocities of cilia are provided only from  $x_2 = 0$  to  $x_2 = y_s$ .

The velocity along cilia increases from roots to tips of cilia, which is shown in Fig. 5(a).<sup>14,31</sup> Fig. 5(a) illustrates the velocity of cilia making angles 50° to 90° to the horizontal plane, which contains in the domain  $\Omega_1$ . The leftmost velocity profile is the velocity of cilia when the angle  $\theta = 50^\circ$ . The next right graph is for the angle  $\theta = 60^\circ$ . It goes on like this until it reaches the rightmost graph, which is the velocity profile of cilia at the angle  $\theta = 90^\circ$ . We suppose that the velocity stops beating at 40°. The graphs are reproduced from Ref. 31, where they have provided the eighth-order polynomial functions of the velocity of cilia of each angle, and the length of cilia has normalized to have a unit length equal to one. The polynomial function provided in Ref. 31 is

$$a_1 \lambda^8 + a_2 \lambda^7 + a_3 \lambda^6 + a_4 \lambda^5 + a_5 \lambda^4 + a_6 \lambda^3 + a_7 \lambda^2 + a_8 \lambda, \tag{5.1}$$

where the coefficients  $a_i, i = 1, 2, \dots, 8$  for each angle  $\theta$  are presented in Table 1 in Ref. 31 and  $\lambda$  is the distance along cilia divided by  $\xi$ . Then

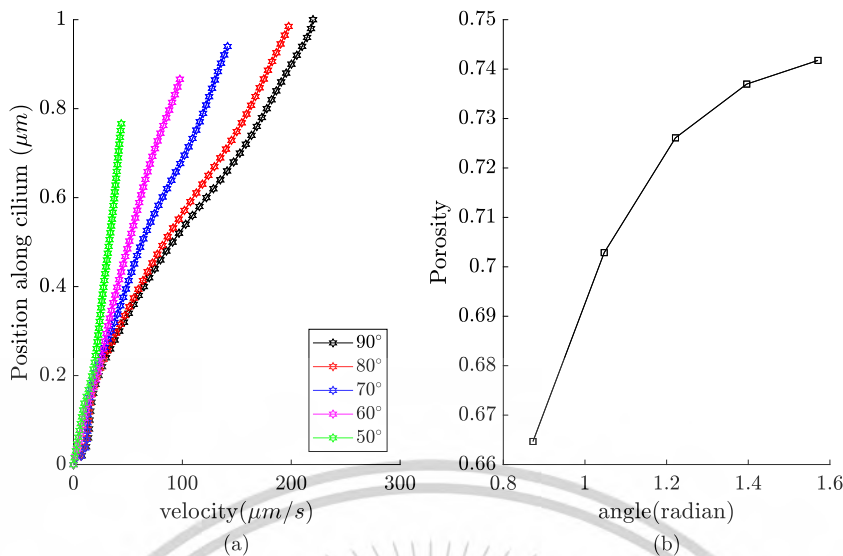


Fig. 5. (a) The velocity of the cilia for the angle  $\theta = 50^\circ, 60^\circ, 70^\circ, 80^\circ,$  and  $90^\circ$ . (b) The porosity at various angles.

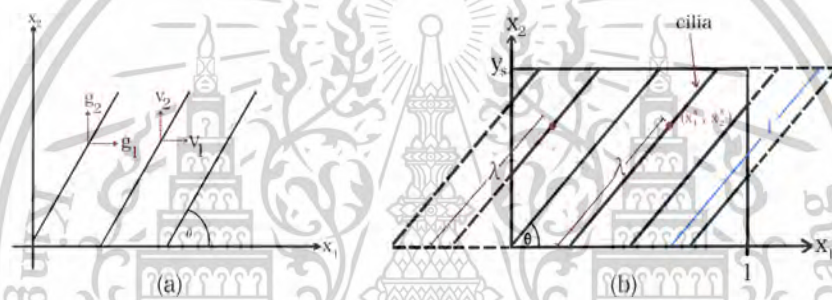


Fig. 6. (a) The directions of the velocity and the gravity components along the  $x_1$  and  $x_2$  axes. (b) The dimensionless domain  $\Omega_1$  and a bundle of cilia in the domain.

$0 \leq \lambda \leq 1$ . Fig. 5(b) shows the porosity for the angle (in radians) from  $50^\circ$  to  $90^\circ$ , which is used in the domain  $\Omega_1$ . Note that the porosity is a constant for each angle  $\theta$ . The viscosity is a constant in both domains  $\Omega_1$  and  $\Omega_2$  and for all angles  $\theta$ .

Fig. 6(a) illustrates the direction of the velocity and gravity. The upward and rightward directions are considered positive. So, the downward direction is considered negative. Fig. 6(b) shows our dimensionless numerical domain and cilia making angle  $\theta$  to the horizontal plane. The variable  $\lambda$  is the distance from the roots of cilia to the point  $(x_1^s, x_2^s)$  on the cilia. If the cilia are perpendicular to the horizontal plane, the variable  $y_s$  is equal to one. For the vectors of the solid velocities  $\mathbf{V}_1^s$  and  $\mathbf{V}_2^s$  in Eq. (3.4), which are the velocities of cilia in each element in  $x_1$  and  $x_2$  directions, respectively, since we use the quadratic triangular element for the velocity, each element contains six nodes. So the vectors  $\mathbf{V}_i^s, i = 1, 2$  have the size  $6 \times 1$ . For each node, we have the position  $(x_1^s, x_2^s)$ . For example, in Fig. 6(b), the point  $(x_1^s, x_2^s)$  is a node in an element. We substitute  $\lambda = y^s / \sin(\theta)$  into the polynomial function Eq. (5.1) to find the solid velocity at each point in the element. Then we calculate

$$v_1^s = v^s \sin(\theta) \text{ and } v_2^s = -v^s \cos(\theta). \tag{5.2}$$

Notice that the solid velocity  $v_2^s$  has the negative sign because when cilia bend down, less than  $90^\circ$ , the direction of  $v_2^s$  is downwards.

For other variables, the fluid density  $\rho = 992.2 \times 10^{-15} (\text{g}/\mu\text{m}^3)$  is the water density at  $40^\circ\text{C}$ .<sup>38</sup> The dynamic viscosity  $\mu$  is  $3 \times 10^{-6} (\text{g}/(\mu\text{m} \cdot \text{s}))$  and the gravity  $\mathbf{g}$  is  $(0, 9.8 \times 10^6) (\mu\text{m}/\text{s}^2)$ . The porosity  $\epsilon^l$  is the fluid volume fraction, depending on the angle  $\theta$ . It is employed from Ref. 31 and Ref. 39 as follows

$$\epsilon^l = 0.5223\theta^5 - 3.0283\theta^4 + 7.0630\theta^3 - 8.4987\theta^2 + 5.5056\theta - 0.8627. \tag{5.3}$$

Since

$$\epsilon^l = \frac{\partial \epsilon^l}{\partial \theta} \frac{\partial \theta}{\partial t}, \tag{5.4}$$

we use the angular velocity to determine  $\frac{\partial \theta}{\partial t}$ . That is  $\frac{\partial \theta}{\partial t}$  equal to the negative value of the speed of cilia over  $\lambda$ . For the inverse of the permeability tensor,  $\mathbf{k}^{-1}$ , we employ the value of  $\mathbf{k}$  from Ref. 39, where numerically have provided the permeability when a periodic array of cylinders makes angle  $\theta, 26 \leq \theta \leq 90$ , to the horizontal plane with different radius of cylinders and various distance between cylinders. Fig. 7(a) presents the arrangement of the periodic array of cylinders studied in Ref. 39. Fig. 7(b) depicts the top view of the array of cylinders for the case that the array of cylinders is oriented perpendicularly to the bottom surface. The variable  $r$  represents the radius of the cylinders and  $\omega$  is the distance between cylinders. In this work, we employ the permeability tensor from Ref. 39 for  $r = 0.1$ , and  $\omega = 0.3$ , which are the radius of cilia and distance between cilia in lungs, respectively.<sup>40</sup>

We find the inverse of the permeability  $\mathbf{k}$  for the angle  $\theta = 50^\circ, 60^\circ, 70^\circ, 80^\circ, 90^\circ$  and provide the values in Table 2.

Table 2 illustrates the elements  $k_{11}^{-1}, k_{12}^{-1}, k_{21}^{-1}$  and  $k_{22}^{-1}$  of the matrix  $\mathbf{k}^{-1}$ . These values will be placed in Eq. (4.6) to find the numerical solutions. We first verify the results by comparing our numerical solutions without the nonlinear and source term with an exact solution which is obtained from the one-dimensional Stokes–Brinkman equations.<sup>32</sup> That is

$$v(y) = \frac{1}{1 + \left(\frac{1-y_s}{\sqrt{k}}\right)} \begin{cases} 1 + \left(\frac{y-y_s}{\sqrt{k}}\right) & , y > y_s, \\ e^{\frac{y-y_s}{\sqrt{k}}} & , y < y_s, \end{cases} \tag{5.5}$$

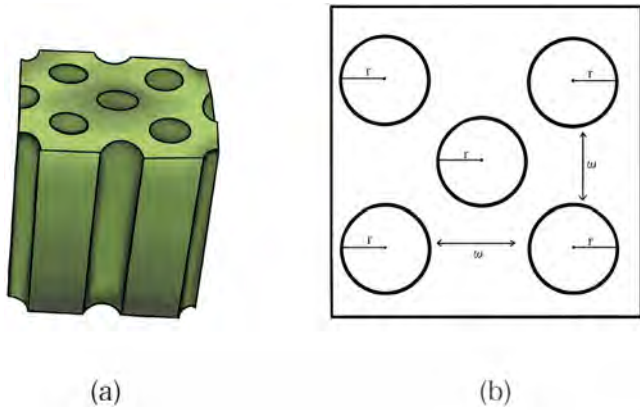


Fig. 7. (a) A periodic cell of the array of cylinders. (b) The top view of the array of cylinders.

Table 2

The inverse of the permeability tensor for the angles  $\theta = 50^\circ, 60^\circ, 70^\circ, 80^\circ$  and  $90^\circ$ .

$\theta$	The inverse of the permeability tensor, $\mathbf{k}^{-1}$			
	$k_{11}^{-1}$	$k_{12}^{-1}$	$k_{21}^{-1}$	$k_{22}^{-1}$
$50^\circ$	992.3664	-381.6794	-381.6794	916.0305
$60^\circ$	748.2993	-204.0816	-204.0816	510.2041
$70^\circ$	658.1741	-106.1571	-106.1571	339.7028
$80^\circ$	596.5463	-47.0958	-47.0958	266.8760
$90^\circ$	556.3690	-14.6413	-14.6413	263.5432

where  $y_s$  is the interface between the porous domain and free-fluid region. For the permeability, we choose the value  $k = 0.0027$  or  $k^{-1} = 1/0.0027$ , which is the state that the cilia are perpendicular to the horizontal plane. We discretize our domain with four different levels of mesh refinement. For the coarser grid, we have 7 nodes in  $x_2$ -direction. For our two-dimensional domain, we use the value of parameters when cilia are perpendicular to the horizontal plane. So, only the velocity in  $x_1$ -direction ( $v_1$ ) is obtained for each  $x_2$  value because we assume that  $v_2$  is zero for the perpendicular case. We then average the velocity,  $v_1$ , over  $x_1$  values. So, we have 7 different velocities for the coarsest mesh refinement. For other mesh refinements, we have 17, 31, and 61 nodes in  $x_2$ -direction. The average velocities are plotted in Fig. 8(a). The plus, circle, cross, diamond and star marks show the velocities for 7, 17, 31, and 61 nodes and the exact solution, respectively. The  $l_2$ -norm errors for 7, 17, 31, and 61 nodes in the  $x_2$ -direction are 0.0919, 0.0277, 0.0141, and 0.0053, respectively. Notice that the numerical solutions converge to the exact solution when the number of nodes in the  $x_2$ -direction increases. Fig. 8(b) depicts the average velocity  $v_2$  over  $x_1$  values for 7, 17, 31, and 61 nodes in the  $x_2$ -direction. The solutions converge to zero as the number of nodes in the  $x_2$ -direction increases. The  $l_2$ -norm errors for 7, 17, 31, and 61 nodes in the  $x_2$ -direction are 0.1257, 0.0425, 0.0123, and 0.0032, respectively. Since, for the perpendicular case, the velocity  $v_2^s$  of the cilia is zero in the direction  $x_2$ , the numerical values of the velocity  $v_2$  of the PCL fluid are close to zero, which is about  $10^{-4}$  for the finest refinement.

Next, we show the convergence of the average of the PCL velocities with having the nonlinear and the velocity of the cilia terms in the governing equation, when the number of degrees of freedom (#dof) increases. We plot the average values of  $v_1$ ,  $v_2$  and the speed in Figs. 9(a), 9(b) and 9(c), respectively, with 187, 659, 1265 and 2678 degrees of freedom when the angle  $\theta = 50^\circ$ . The blue, red, green, and black colors represent the PCL velocities using 187, 659, 1265 and 2678 degrees of freedom, respectively. The solutions obtained from the coarser meshes converge to those of the finest mesh, which is 2678 degrees of freedom. Table 3 shows the number of iterations and times (minutes) used to compute the solutions with different number of degrees of freedom. The

Table 3

The number of iterations and time for each number of degrees of freedom.

#dof	Number of iterations	Time (min)
187	46	41
659	40	179
1265	40	355
2678	40	785

Table 4

The  $l_2$ -norm errors of the numerical solutions for different number of degrees of freedom.

#dof	The $l_2$ -norm errors		
	$v_1$	$v_2$	speed
187	2.3467	1.5123	2.0129
659	1.1231	0.5676	1.8875
1265	0.5550	0.1886	0.6687

Table 5

The number of iterations of Newton's method, computation time and number of degrees of freedom for each angle.

$\theta$	Number of iterations	Time (min)	#dof
$50^\circ$	84	1600	2678
$60^\circ$	56	1065	2863
$70^\circ$	34	748	3184
$80^\circ$	7	178	3725
$90^\circ$	2	29	2267

tolerance (tol) is  $5 \times 10^{-3}$ . The  $l_2$ -norm errors of the results are shown in Table 4. Table 4 illustrates the errors of the average velocities  $v_1$  and  $v_2$  and the speed of the PCL fluid compared with the solutions obtained from the finest grid. It shows that the errors decrease when the number of degrees of freedom increases.

Next, we apply the mixed finite element technique of Taylor-Hood type combined with the Newton's method to the governing equations to find the velocity of the PCL fluid when the cilia make angles with the horizontal plane. The mesh refinement is generated by using the open software Netgen,<sup>41</sup> see Fig. 10, which is between 1000 and 1700 grid points. Fig. 10 illustrates the mesh generations on the domain  $\Omega$ . From left to right and from top to bottom, the plots show the meshes from the angles  $\theta = 50^\circ$  to  $90^\circ$ , respectively, where the horizontal line in each picture indicates the free-fluid/porous-medium interface at  $x_2 = y_s$ .

Table 5 shows the number of iterations of Newton's method, the computation time and the number of degrees of freedom (#dof) for each angle  $\theta$ . The initial guess used in Eq. (4.6) is  $\bar{V}^n = 1$  to calculate the numerical solution. The iterations are stopped when  $\|\Delta \bar{V}\|_2 < tol$ , where  $tol = 5 \times 10^{-4}$ . Since the height of our numerical domain is 1, when cilia bend down and make angle  $80^\circ$  with the horizontal plane, the height of the free-fluid region is 0.0152, which is a small number. So finer elements are needed in this free-fluid region. Then the number of degrees of freedom for the angle  $80^\circ$  is higher than that of the others and it is similar for other smaller angles. The velocities of the PCL fluid,  $v_1$  and  $v_2$ , are depicted in Figs. 11 and 12, where from left to right and from top to bottom of these figures are the velocities of the PCL fluid for angles  $50^\circ$  to  $90^\circ$ , respectively. Fig. 11 illustrates the velocities of  $v_1$  of the PCL fluid for angles  $50^\circ$  to  $90^\circ$ , where the velocity is maximum at the top of the domain  $\Omega_2$  and zero at the root of cilia. The maximum velocity occurs when  $\theta = 90^\circ$ , and the velocities decrease when the angle decreases. The velocities are constants from the tips of the cilia to the top of the domain  $\Omega_2$  for angles  $50 \leq \theta < 90$ . Fig. 12 shows the velocities  $v_2$  of the PCL fluid for angles  $50^\circ$  to  $90^\circ$ . For the forward stroke, cilia start at  $\theta = 90^\circ$  and then bend down to  $50^\circ$  and stop beating at  $\theta = 40^\circ$ . So, the velocity  $v_2$  at angle  $\theta = 90^\circ$  is almost zero and the velocities for the angles  $\theta = 50^\circ, 60^\circ, 70^\circ$ , and  $80^\circ$  are negative.

Figs. 13 and 14 show the average velocities of  $v_1$  and  $v_2$ , over the  $x_1$ -axis. In Figs. 13 and 14, each curve has two colors. The color in the

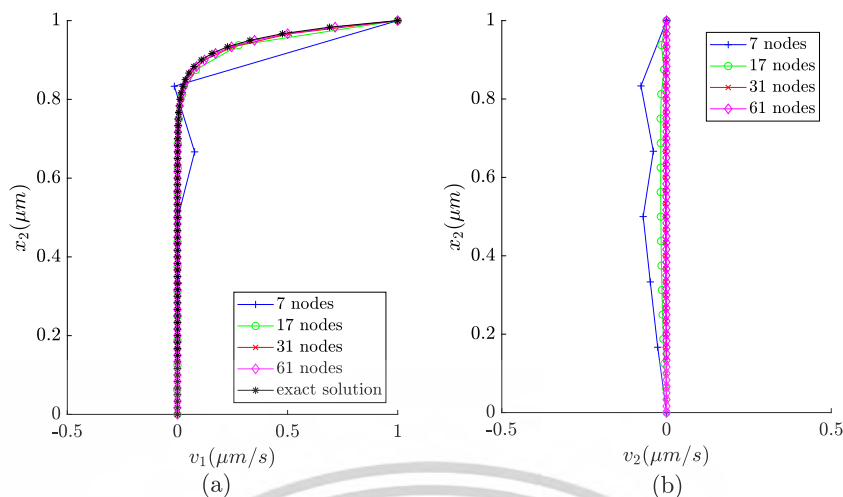


Fig. 8. The average velocity profile of two-dimensional numerical solution for 7, 17, 31, and 61 nodes when  $\theta = 90^\circ$  along the  $x_2$ -axis. (a) the average velocity  $v_1$  for each node and the exact solution. (b) the average velocity  $v_2$  for each node.

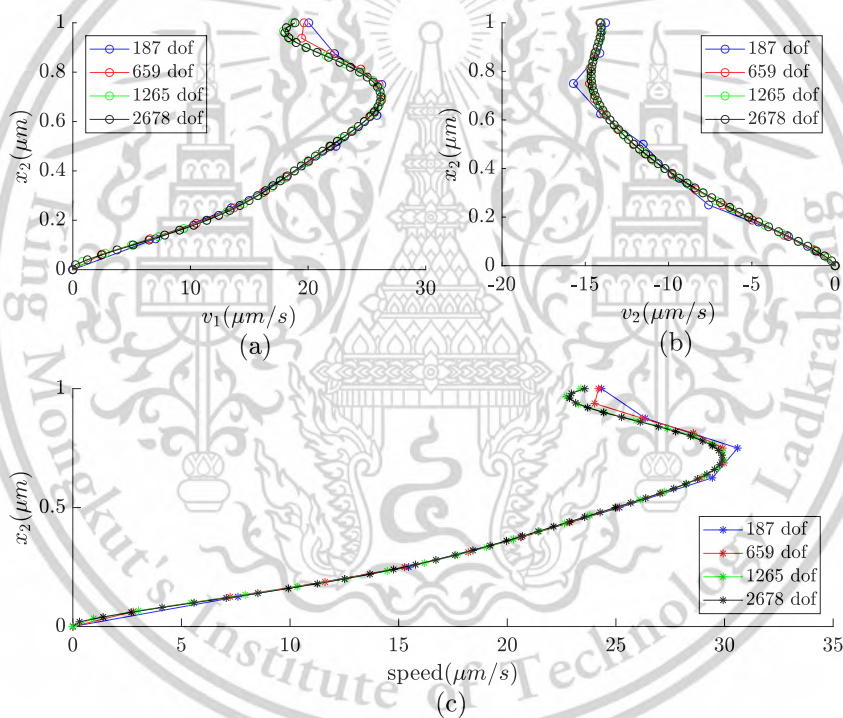


Fig. 9. The average velocities and speed with 187, 659, 1265 and 2678 degrees of freedom at the angle  $\theta = 50^\circ$ . (a) The average velocity  $v_1$ . (b) The average velocity  $v_2$ . (c) The average speed.

lower part of the line shows the solutions in the porous medium and the color located towards the tip of the cilia presents the solutions in the free-fluid region as well as in Fig. 15. For Fig. 13, the highest velocity of the PCL fluid is at the angle  $\theta = 90^\circ$  and it decreases as the degree decreases. So the slowest velocity is at the angle  $\theta = 50^\circ$ . Comparing with Fig. 5, the average velocity of  $v_1$  is lower than the velocity of cilia about 21%, 18%, 22%, 25% and 26% for the angles  $\theta = 50^\circ, 60^\circ, 70^\circ, 80^\circ$  and  $90^\circ$ , respectively. The average velocities of  $v_2$  of the PCL fluid for all angles are plotted in Fig. 14, which shows that the average velocity at the angle  $\theta = 90^\circ$  is almost zero, and the other angles are negative. Notice that the average velocities of  $v_2$  of the PCL fluid from the angle  $\theta = 90^\circ$  to  $80^\circ$  rapidly decrease and gradually decrease until  $\theta = 60^\circ$  and the average velocity from the angle  $\theta = 60^\circ$  to  $50^\circ$  increases because the cilia begin to stop beating and the cilia stop beating at the

angle  $\theta = 40^\circ$ , which results in increasing velocity and become zero at  $\theta = 40^\circ$ . Fig. 15 illustrates the speeds over the  $x_1$ -axis,  $\|v\|$ , for the angles  $50^\circ, 60^\circ, 70^\circ, 80^\circ$ , and  $90^\circ$ . The shape of the speed of each angle is almost the same as the average velocity of  $v_1$  over the  $x_1$ -axis. This means the velocity in  $x_1$ -direction has greater effect of motion of the PCL fluid than  $v_2$ . To compare our numerical solution with an available research, we compute the average speed of the PCL fluid for all angles. The result is depicted in Fig. 16. Next, we compare the average speed for all angles with the experimental data reported in Ref. 42. They investigated the movement of the PCL in well-differentiated human tracheobronchial epithelial cell cultures exhibiting spontaneous and radial mucociliary transport. The study employed conventional and confocal microscopy techniques using fluorescent microspheres and photoactivated fluorescent dyes. The research has revealed that the

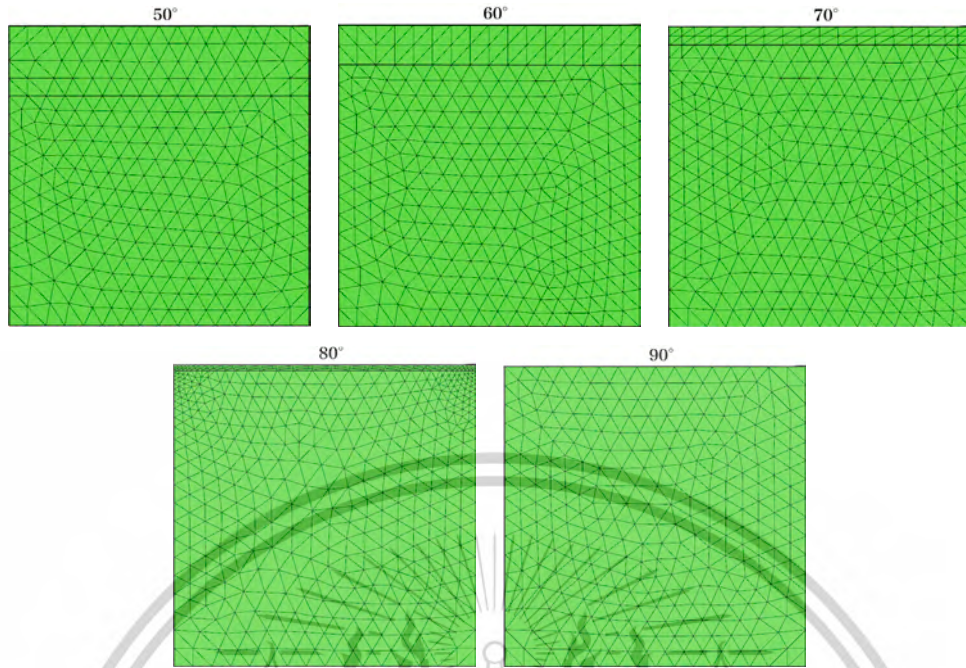


Fig. 10. Netgen<sup>41</sup> generated mesh of the PCL domain for various angles.

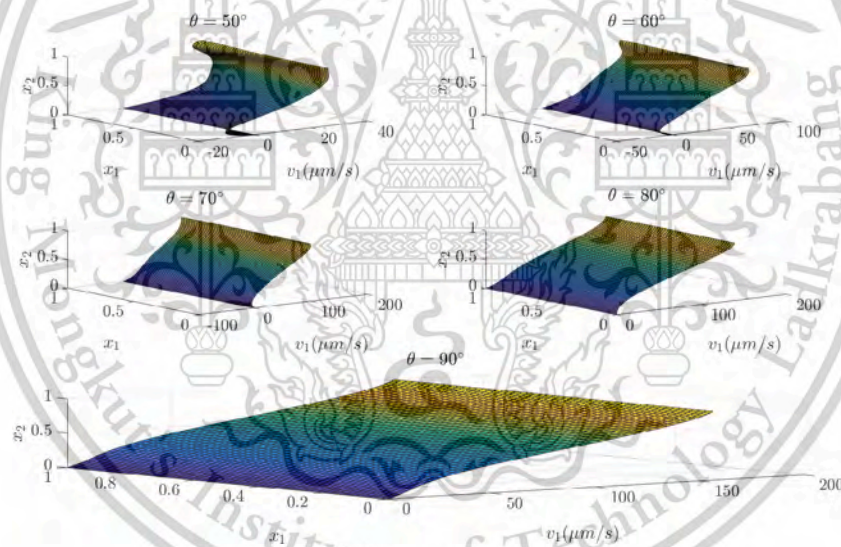


Fig. 11. The velocity of the PCL fluid,  $v_1$ , in  $x_1$ -direction when the angles  $\theta = 50^\circ, 60^\circ, 70^\circ, 80^\circ$ , and  $90^\circ$ .

velocity of the PCL fluid is approximately  $39.2 \pm 4.7 \mu\text{m/s}$ . From Fig. 16, we find the average of the average speed for all angles, which is about  $43 \mu\text{m/s}$  being in the range of the experimental results.

**6. Conclusion**

We consider the fluid flow in the Periciliary layer (PCL) in the human lungs. The PCL consists of two phases: the fluid phase, Newtonian fluid, and the solid phase known as cilia. When the cilia move forward in order to remove the mucus from the human body, the cilia make angles with the horizontal plane. In this study, we consider the forward stroke of cilia having maximum velocity at  $\theta = 90^\circ$  and the velocity decreases when the angle decreases and then the cilia stop beating at  $\theta = 40^\circ$ . The angles used in this work are  $\theta = 50^\circ, 60^\circ, 70^\circ, 80^\circ$ , and  $90^\circ$ . The PCL region is divided into two domains when  $\theta < 90^\circ$ : the porous domain and free-fluid region, and the PCL region has only the

porous domain when cilia are perpendicular to the horizontal plane. We apply the nonlinear Brinkman equations in the macroscopic scale to the porous domain  $\Omega_1$  and the steady-state Navier–Stokes equations to the free-fluid region  $\Omega_2$ . We use the mixed finite element method of Taylor–Hood type combined with Newton’s method to find the velocity of the PCL fluid. Regarding the boundary conditions, we assume that the bottom of the domain has zero velocity and the rate of change of the velocity with respect to  $x_2$  at the top of the domain is zero. The velocity is continuous at the porous medium/free-fluid interface. The velocities of the cilia are plotted in Fig. 5. The mesh refinement for each angle is shown in Fig. 10. The numerical solutions are first averaged and compared with the exact solution for a one-dimensional domain to verify the result. The result are in a good agreement. For the two-dimensional numerical solutions of the velocities of the PCL fluid, we provide the velocities in  $x_1$ -direction,  $v_1$ , and  $x_2$ -direction,  $v_2$ , for all angles in Figs. 11 and 12. Then the velocities are averaged to see the

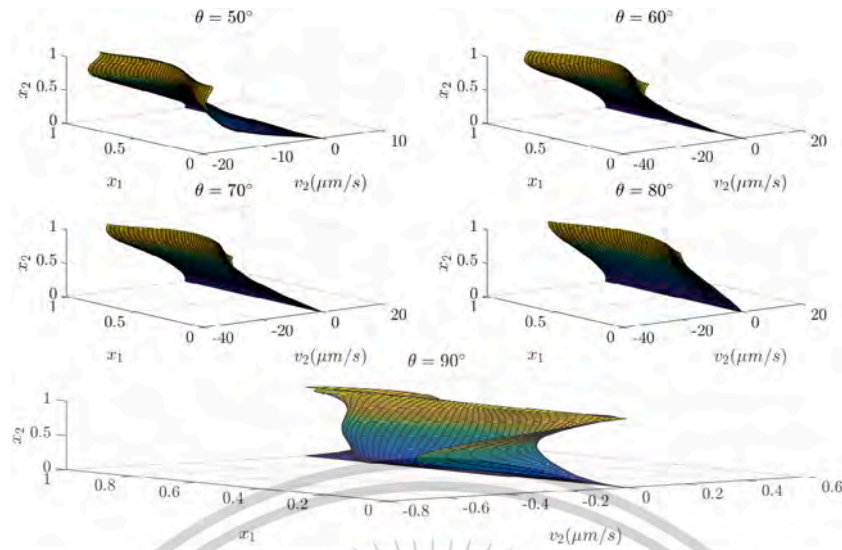


Fig. 12. The velocity of the PCL fluid,  $v_2$ , in  $x_2$ -direction when the angles  $\theta = 50^\circ, 60^\circ, 70^\circ, 80^\circ$ , and  $90^\circ$ .

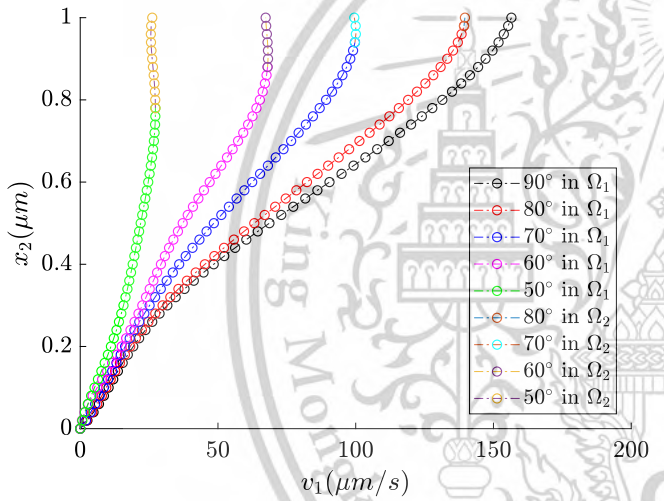


Fig. 13. The average velocity of  $v_1$  of the PCL fluid for 5 different angles in  $x_2$ -direction.

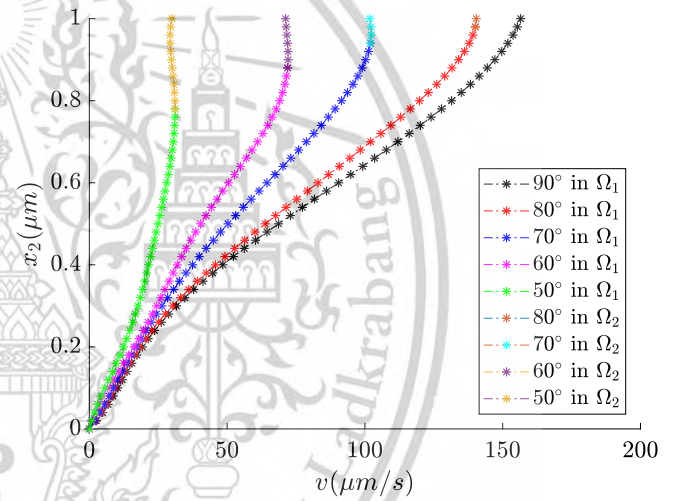


Fig. 15. The speeds of the PCL fluid for 5 different angles in  $x_2$ -direction.

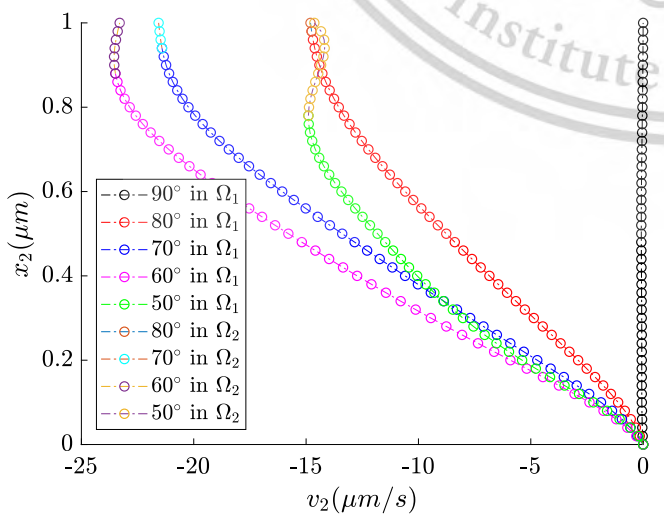


Fig. 14. The average velocity of  $v_2$  of the PCL fluid for 5 different angles in  $x_2$ -direction.

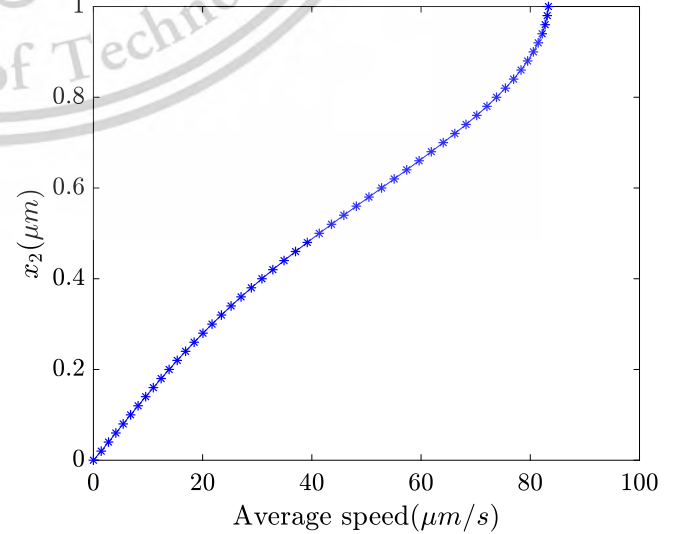


Fig. 16. The average speed for all angles.

This material is reserved for educational use only, not allowed for commercial use.

Forbidden to modify the content, and cite the document when use.

velocity profiles including the speed of the PCL fluid. The shapes of the profiles of  $v_1$  are similar to those of speed. This fact provides that the velocity  $v_1$  takes more effect to the movement of the PCL fluid. In future research, we aim to incorporate the full movement of cilia into our study. We also will use the unsteady state equations to see the movement of the PCL fluid affecting the mucus velocity.

### Declaration of competing interest

The authors declare that they have no known competing financial interests or personal relationships that could have appeared to influence the work reported in this paper.

### Acknowledgment

This paper is supported by the School of Science, King Mongkut's Institute of Technology Ladkrabang, Bangkok, Thailand.

### Data availability

No data was used for the research described in the article.

### References

- Corfield AP. Mucins: a biologically relevant glycan barrier in mucosal protection. *Biochim Biophys Acta*. 2015;1850(1):236–252. <http://dx.doi.org/10.1016/j.bbagen.2014.05.003>.
- Bustamante-Marin XM, Ostrowski LE. Cilia and mucociliary clearance. *Cold Spring Harbor Perspect Biol*. 2017;9(4):a028241. <http://dx.doi.org/10.1101/cshperspect.a028241>.
- Kori J, Pratibha. Numerical simulation of mucus clearance inside lung airways. *J Appl Fluid Mech*. 2018;11(5):1163–1171. <http://dx.doi.org/10.29252/JAFM.11.05.28011>.
- Lee WL, Jayathilake PG, Tan Z, Le DV, Lee HP, Khoo BC. Muco-ciliary transport: effect of mucus viscosity, cilia beat frequency and cilia density. *Comput & Fluids*. 2011;49(1):214–221. <http://dx.doi.org/10.1016/j.compfluid.2011.05.016>.
- Sedaghat M, Shahmardan M, Norouzi M, Jayathilake P, Nazari M. Numerical simulation of muco-ciliary clearance: immersed boundary-lattice Boltzmann method. *Comput & Fluids*. 2016;131:91–101. <http://dx.doi.org/10.1016/j.compfluid.2016.03.015>.
- Munkholm M, Mortensen J. Mucociliary clearance: Pathophysiological aspects. *Clin Physiol Funct Imaging*. 2014;34(3):171–177. <http://dx.doi.org/10.1111/cpf.12085>.
- Vanaki SM, Holmes D, Saha SC, Chen J, Brown RJ, Jayathilake PG. Mucociliary clearance: A review of modelling techniques. *J Biomech*. 2020;99:109578. <http://dx.doi.org/10.1016/j.jbiomech.2019.109578>.
- Bansil R, Turner BS. The biology of mucus: Composition, synthesis and organization. *Adv Drug Del Rev*. 2018;124:3–15. <http://dx.doi.org/10.1016/j.addr.2017.09.023>.
- Jory M, Donnarumma D, Blanc C, et al. Mucus from human bronchial epithelial cultures: rheology and adhesion across length scales. *Interface Focus*. 2022;12(6):20220028. <http://dx.doi.org/10.1098/rsfs.2022.0028>.
- Kelly SJ, Genevskiy V, Björklund S, et al. Water sorption and structural properties of human airway mucus in health and muco-obstructive diseases. *Biomacromolecules*. 2024. <http://dx.doi.org/10.1021/acs.biomac.3c01170>.
- Ren S, Li W, Wang L, et al. Numerical analysis of airway mucus clearance effectiveness using assisted coughing techniques. *Sci Rep*. 2020;10(1):2030. <http://dx.doi.org/10.1038/s41598-020-58922-7>.
- Ding Y, Nawroth JC, McFall-Ngai MJ, Kanso E. Mixing and transport by ciliary carpets: A numerical study. *J Fluid Mech*. 2014;743:124–140. <http://dx.doi.org/10.1017/jfm.2014.36>.
- Guo H, Nawroth J, Ding Y, Kanso E. Cilia beating patterns are not hydrodynamically optimal. *Phys Fluids*. 2014;26(9):091901. <http://dx.doi.org/10.1063/1.4894855>.
- Sears PR, Thompson K, Knowles MR, Davis CW. Human airway ciliary dynamics. *Am J Physiol-Lung Cell Mol Physiol*. 2013;304(3):L170–L183. <http://dx.doi.org/10.1152/ajplung.00105.2012>.
- Xu L, Jiang Y. Cilium height difference between strokes is more effective in driving fluid transport in mucociliary clearance: A numerical study. *Math Biosci Eng*. 2015;12(5):1107–1126. <http://dx.doi.org/10.3934/mbe.2015.12.1107>.
- Jayathilake PG, Tan Z, Le DV, Lee HP, Khoo BC. Three-dimensional numerical simulations of human pulmonary cilia in the periciliary liquid layer by the immersed boundary method. *Comput & Fluids*. 2012;67:130–137. <http://dx.doi.org/10.1016/j.compfluid.2012.07.016>.
- Wei D, Dehnavi PG, Aubin-Tam M, Tam D. Measurements of the unsteady flow field around beating cilia. *J Fluid Mech*. 2021;915:A70. <http://dx.doi.org/10.1017/jfm.2021.149>.
- Vanaki SM, Holmes D, Jayathilake PG, Brown R. Three-dimensional numerical analysis of periciliary liquid layer: Ciliary abnormalities in respiratory diseases. *Appl Sci*. 2019;9(19):4033. <http://dx.doi.org/10.3390/app9194033>.
- Sleigh MA. Ciliary adaptations for the propulsion of mucus. *Biorheology*. 1990;27(3–4):527–532. <http://dx.doi.org/10.3233/bir-1990-273-431>.
- Cushman JH, Bennethum LS, Hu BX. A primer on upscaling tools for porous media. *Adv Water Resour*. 2002;25(8–12):1043–1067. [http://dx.doi.org/10.1016/S0309-1708\(02\)00047-7](http://dx.doi.org/10.1016/S0309-1708(02)00047-7).
- Wuttanachamsri K, Schreyer L. Effects of cilia movement on fluid velocity: I model of fluid flow due to a moving solid in a porous media framework. *Transp Porous Media*. 2021;136(2):699–714. <http://dx.doi.org/10.1007/s11242-020-01539-1>.
- Hwang WR, Advani SG. Numerical simulations of Stokes-Brinkman equations for permeability prediction of dual scale fibrous porous media. *Phys Fluids*. 2010;22(11). <http://dx.doi.org/10.1063/1.3484273>.
- Fujisawa K, Murakami A. Numerical analysis of coupled flows in porous and fluid domains by the Darcy-Brinkman equations. *Soils Found*. 2018;58(5):1240–1259. <http://dx.doi.org/10.1016/j.sandf.2018.07.003>.
- Suankasem S, Pimkote A, Thammathon I, Wuttanachamsri K. Matched asymptotic expansion for PCL fluid due to the movement of lung cilia: part 1. 2018 Paper presented at: 10th National Science Research Conference; May 24–25, 2018; Maha Sarakham, TH.
- Poopra S, Wuttanachamsri K. The velocity of PCL fluid in human lungs with Beaver and Joseph boundary condition by using asymptotic expansion method. *Mathematics*. 2019;7(6):567. <http://dx.doi.org/10.3390/math7060567>.
- Poopra S, Wuttanachamsri K. On the asymptotic boundary condition at the free-fluid/porous-medium interface in periciliary layer due to the ciliary movement. *Math Probl Eng*. 2022;2022. <http://dx.doi.org/10.1155/2022/1390486>.
- Chen N, Gunzburger M, Wang X. Asymptotic analysis of the differences between the Stokes-Darcy system with different interface conditions and the Stokes-Brinkman system. *J Math Anal Appl*. 2010;368(2):658–676. <http://dx.doi.org/10.1016/j.jmaa.2010.02.022>.
- Phaenchat S, Wuttanachamsri K. On the nonlinear Stokes-Brinkman equations for modeling flow in PCL. 2019 Paper presented at: The 24th Annual Meeting in Mathematics; May 15–17, 2019; Chonburi, TH.
- Kasamwan T, Wuttanachamsri K. Unsteady one-dimensional flow in PCL with Stokes-Brinkman equations. 2020 Paper presented at: Phayao Research Conference; January 23–24 2020; Phayao, TH.
- Chamsri K. N-dimensional Stokes-Brinkman equations using a mixed finite element method. *Aust J Basic Appl Sci*. 2014;8(11):30–36.
- Wuttanachamsri K, Schreyer L. Effects of cilia movement on fluid velocity: II numerical solutions over a fixed domain. *Transp Porous Media*. 2020;134(2):471–489. <http://dx.doi.org/10.1007/s11242-020-01455-4>.
- Oangwacharaparkan N, Wuttanachamsri K. The flow in periciliary layer in human lungs with Navier-Stokes-Brinkman equations. *Tamkang J Math*. 2023;54(2):107–120. <http://dx.doi.org/10.5556/j.tkmj.54.2023.3738>.
- Wuttanachamsri K. Free interfaces at the tips of the cilia in the one-dimensional periciliary layer. *Mathematics*. 2020;8(11):1961. <http://dx.doi.org/10.3390/math8111961>.
- Hassanizadeh M, Gray WG. General conservation equations for multi-phase systems: 1. Averaging procedure. *Adv Water Resour*. 1979;2:131–144. [http://dx.doi.org/10.1016/0309-1708\(79\)90025-3](http://dx.doi.org/10.1016/0309-1708(79)90025-3).
- Hassanizadeh M, Gray WG. General conservation equations for multi-phase systems: 2. Mass, momenta, energy, and entropy equations. *Adv Water Resour*. 1979;2:191–203. [http://dx.doi.org/10.1016/0309-1708\(79\)90035-6](http://dx.doi.org/10.1016/0309-1708(79)90035-6).
- Weinstein T, Bennethum LS. On the derivation of the transport equation for swelling porous materials with finite deformation. *Int J Eng Sci*. 2006;44(18–19):1408–1422. <http://dx.doi.org/10.1016/j.ijengsci.2006.08.001>.
- Braess D. *Finite Elements: Theory, Fast Solvers, and Applications in Solid Mechanics*. Cambridge University Press; 2007. <http://dx.doi.org/10.1017/CBO9780511618635>.
- The Engineering ToolBox. Water-density, specific weight and thermal expansion coefficients. 2003 [https://www.engineeringtoolbox.com/water-density-specific-weight-d\\_595.html](https://www.engineeringtoolbox.com/water-density-specific-weight-d_595.html). [Accessed 26 September 2023].
- Chamsri K, Bennethum L. Permeability of fluid flow through a periodic array of cylinders. *Appl Math Model*. 2015;39(1):244–254. <http://dx.doi.org/10.1016/j.apm.2014.05.024>.
- ICRP. Human respiratory tract model for radiological protection. 1994:1. ICRP Publication 66. Ann. 24.
- Schöberl J. NETGEN An advancing front 2D/3D-mesh generator based on abstract rules. *Comput Vis Sci*. 1997;1(1):41–52. <http://dx.doi.org/10.1007/s007910050004>.
- Matsui H, Randell SH, Peretti SW, Davis CW, Boucher RC. Coordinated clearance of periciliary liquid and mucus from airway surfaces. *J Clin Invest*. 1998;102(6):1125–1131. <http://dx.doi.org/10.1172/JCI2687>.

# Appendix B

The research paper



This material is reserved for educational use only, not allowed for commercial use.

Forbidden to modify the content, and cite the document when use.

## EFFECT OF POROUS MEDIUM TO FLUID FLOW IN MUCUS LAYER

Surachai Phaenchat,  Kanognudge Wuttanachamsri\*

Department of Mathematics, King Mongkut's Institute of Technology Ladkrabang,  
Bangkok, Thailand

**Abstract.** Mucociliary clearance (MCC) is a protective process in human respiratory system to expel inhaled strange particles such as dust, dirt, and smoke out of the human body. The particles are caught by mucus residing in the respiratory tract and then mucus forms a mucus layer (ML) lining above the cilia settling on the ciliated epithelial cells. The mucus is removed from the human body by ciliary beating. Here, we study the fluid flow above the tips of cilia up to the mucus layer affected by the movement of cilia. In this work, the two-dimensional Stokes equation is applied to find the velocities of the fluid in the free-fluid region. The numerical solutions are approximated by using a mixed finite element method. This problem can be usefully applied to problems in which fluids are affected by the self-movement of a solid phase.

**Keywords:** Stokes equation, mixed finite element method, free-fluid region, mucus layer.

**AMS Subject Classification:** 35Q35, 35Q90, 35Q92, 65N30, 76D07, 76Z05, 76Z10, 92B05.

**Corresponding author:** Kanognudge Wuttanachamsri, Department of Mathematics, King Mongkut's Institute of Technology Ladkrabang, Ladkrabang, Bangkok 10520, Thailand, e-mail: [kanognudge.wu@kmitl.ac.th](mailto:kanognudge.wu@kmitl.ac.th)

*Received: 20 May 2024; Revised: 28 July 2025; Accepted: 16 September 2025; Published: 10 April 2025.*

### 1 Introduction

Mucus is a viscous fluid produced in the human body, in which the mucus comprises of 95% water, 2–3% glycoproteins and proteins, 1% mineral, 1% lipids and 0.02% DNA (Matthews et al., 1963; Potter et al., 1967). The mucus is part of airway surface liquid (ASL) that lines between the epithelial cells and air in the respiratory tract. The ASL consists of two layers: the mucus layer (ML) and the periciliary layer (PCL). The mucus layer is adjacent to the air surface and is on the PCL covering the epithelial cell surface (Boucher, 1999; Derichs et al., 2011) as shown in Figure 1. Figure 1 shows a portion of a cross-section of the trachea that comprises of the inhaled particles, air, the mucus layer (ML), the periciliary layer (PCL), cilia, epithelial cells, ciliated cells and goblet cells. The PCL consists of two phases: liquid and solid phases, where the liquid and solid phases are the PCL fluid and cilia, respectively. Therefore, the PCL is considered as a porous medium. The mucus is secreted from the goblet cell scattering in the epithelial cell to catch foreign particles that get into the human body. After that the mucus forms the mucus layer lining above the PCL and is moved out of the body by the beating of cilia. This mechanism is called Mucociliary clearance (MCC), which is the primary innate defense mechanism of the human respiratory system (Knowles & Boucher, 2002; Wanner et al., 1996).

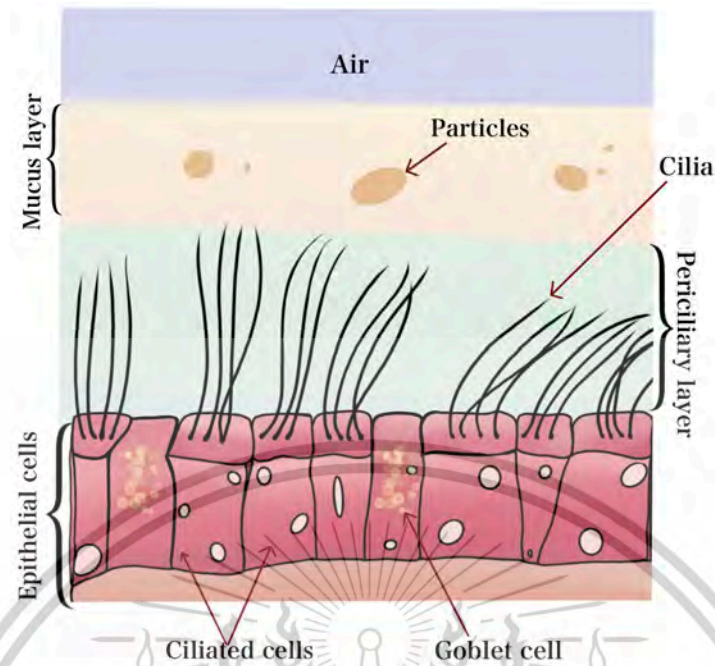


**Figure 1:** The clearance of mucus in the respiratory system

Several studies investigated MCC both numerically and experimentally (Battle et al., 2015; Ding et al., 2014; Houtmeyers et al., 1999; Lale et al., 1998; Rusznak et al., 1994; Satir & Christensen, 2007; Sedaghat et al., 2023; Vanaki et al., 2020; Xu & Jiang, 2015). For example, Xu & Jiang (2015) considered five rods (cilia) for both symmetric and asymmetric cilia motion by using a rod-propel-fluid model. They found that the cilium height difference was efficient in driven transport and the transport capacity of the MCC increased when cilia density and cilia beating frequency increased. Ding et al. (2014) studied the fluid flow in both the PCL and the ML by using three-dimensional microscale equations. Sedaghat et al. (2023) studied the effect of cilia abnormalities on mucociliary clearance (MCC) in bronchial airways by using three-dimensional incompressible modified Navier-Stokes equations. The finite difference projection method was used to solve these equations. Vanaki et al. (2020) investigated the cilia in both the healthy state and the disease state for mucociliary clearance in the human respiratory system. They found the numerical solutions depending on various parameters such as ciliary beat frequency (CBF), metachronal waves of cilia, surface tension at the PCL-mucus interface, ciliary length, ciliary density, and liquid depth in the airway. Poopra & Wuttanachamsri (2019, 2022) and SuanKasem et al. (2018) studied the velocity of the PCL fluid using one-dimensional Stokes-Brinkman equations by using asymptotic expansion method in different approaches. Phaenchat & Wuttanachamsri (2019), and Kasamwan & Wuttanachamsri (2020) calculated the velocities of PCL fluid by using a finite element method, a finite different method and classical linearization method. Chamsri (2014) used a mixed finite element method to discretize the n-dimensional macroscale Stokes-Brinkman equations which were used to find the velocity of the PCL fluid in Wuttanachamsri & Schreyer (2020). Free interfaces at the tips of cilia in the PCL was presented in Wuttanachamsri (2020). Verma & Rana (2015) used steady-state mathematical model to study mucus transport in the airway in the human lung. Modaresi & Shirani (2023) investigated the velocities of both the PCL and ML by using three-dimensional mathematical models. The velocities were influenced by variations in mucus viscosity and distinct velocities at the PCL/ML interface. Wuttanachamsri et al. (2024) provided the velocity of the PCL fluid in the porous medium when cilia beat forward by using the two-dimensional Brinkman equation.

Here, we examine the velocity profiles of both the PCL fluid and the mucus. Figure 2 depicts the computational domain used in our investigation, which consists of the ML and the

PCL. Within the PCL, the black straight lines represent cilia, which make the angle  $\theta$  with the horizontal plane. The variable  $y_{PCL}$  is the  $y$  value at the interface between the PCL and the ML and  $y_{in}$  is  $y$  value at the interface between the porous medium and the free-fluid region. For example, the symbols  $y_{in}(80^\circ)$  and  $y_{in}(70^\circ)$  are  $y$  values at the interface between the porous medium and the free-fluid region when cilia make the angle  $80^\circ$  and  $70^\circ$  with the horizontal plane, respectively. When cilia make an angle  $\theta < 90^\circ$ , the PCL can be divided into two layers: the porous medium, comprising both the PCL fluid and cilia, and the free-fluid region, containing only the PCL fluid. For  $\theta = 90^\circ$ , there exists only the porous medium in the PCL. In this work, we concentrate on two domains: the free-fluid region,  $\Omega_1$ , and the ML,  $\Omega_2$ . In domain  $\Omega_1$ , the free-fluid region occurs at the angle  $\theta < 90^\circ$ . As cilia bend downward to various angles, the height of the free-fluid region varies from  $y_{in}$  to  $y_{PCL}$ . For example, at the angle  $80^\circ$ , the height from  $y_{in}(80^\circ)$  to  $y_{PCL}$  is 0.0152, while at the angle  $70^\circ$ , the height from  $y_{in}(70^\circ)$  to  $y_{PCL}$  is 0.0603.

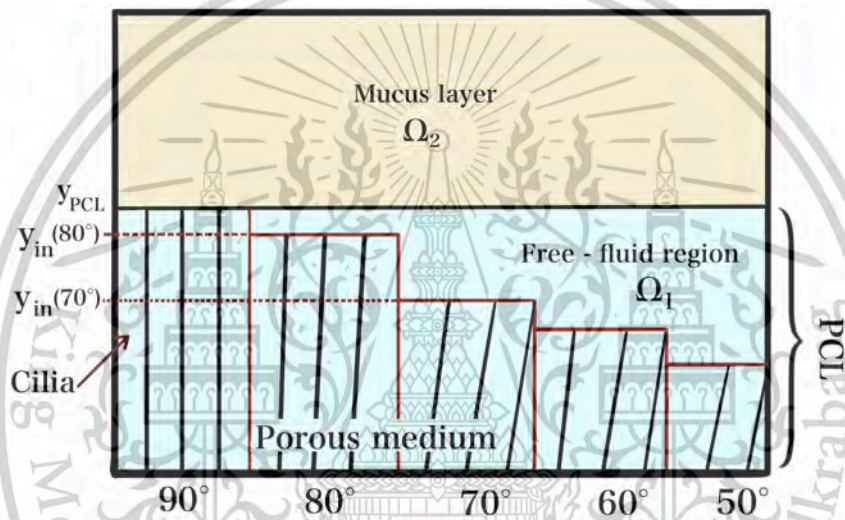


Figure 2: Cartoon picture of the PCL and the ML

To determine the velocities of the fluids in  $\Omega_1$  and  $\Omega_2$  influenced by cilia movement, we use the velocity of the PCL fluid within the porous medium obtained from Wuttanachamsri et al. (2024) as the lower boundary condition of domain  $\Omega_1$  to compute the velocity of the PCL fluid in  $\Omega_1$ . After that, we adopt the velocity of the PCL fluid within  $\Omega_1$  as the lower boundary condition of domain  $\Omega_2$  to determine the velocity of the mucus. By creating the numerical domain in which the self-movement of cilia affects the fluid flow in domains  $\Omega_1$  and  $\Omega_2$  when cilia make various angles to the horizontal plane within one numerical domain, and the fluid velocity in  $\Omega_1$  is used to calculate the mucus velocity, to the author's knowledge, this research has never been done before. In this work, the velocities of the fluids in  $\Omega_1$  and  $\Omega_2$  are found by using the two-dimensional Stokes equation. A mixed-finite element method is used to approximate the numerical solutions.

In Section 2, we present the governing equation. The discretization of the mathematical model using a mixed-finite element method is described in Section 3. The numerical results of the velocities of the fluid in  $\Omega_1$  and  $\Omega_2$  are presented in Section 5. The conclusion is drawn in Section 6.

## 2 Governing Equation

In this section, we provide the governing equation used in this work. We assume that the fluids in  $\Omega_1$  and  $\Omega_2$  moving past the layers are incompressible. Therefore, we use the Stokes equation

and the continuity equation in both domains,

$$\nabla p - \mu \Delta \mathbf{v} = \rho \mathbf{g}, \quad (1)$$

$$\nabla \cdot \mathbf{v} = 0, \quad (2)$$

where  $\mu$  is a dynamic viscosity,  $p$  is pressure,  $\rho$  is fluid density,  $\mathbf{v}$  is velocity of the fluid and  $\mathbf{g}$  is gravity. In the two-dimensional domain, let  $\mathbf{v} = (u, v)$  and  $\mathbf{g} = (g_x, g_y)$ . Then Eqs. (1) and (2) can be rewritten as

$$\frac{\partial p}{\partial x} - \mu \left( \frac{\partial^2 u}{\partial x^2} + \frac{\partial^2 u}{\partial y^2} \right) = \rho g_x, \quad (3)$$

$$\frac{\partial p}{\partial y} - \mu \left( \frac{\partial^2 v}{\partial x^2} + \frac{\partial^2 v}{\partial y^2} \right) = \rho g_y, \quad (4)$$

$$\frac{\partial u}{\partial x} + \frac{\partial v}{\partial y} = 0. \quad (5)$$

We now have three equations and three unknowns, which are  $u, v$  and  $p$ . The governing equations (3) - (5) will be discretized in the next section.

### 3 Model Discretization

The mathematical model in Section 2 is discretized in this section by using a mixed finite element method. Define  $w$  and  $Q$  be quadratic and linear weight functions. To find the weak formulation, we multiply Eqs. (3) - (4) by  $w$  and Eq. (5) by  $Q$  and integrate over the domain  $\Omega_i, i = 1, 2$ . Then Eqs. (3) - (5) becomes

$$\int_{\Omega_i} \left[ w \frac{\partial p}{\partial x} - \mu w \left( \frac{\partial^2 u}{\partial x^2} + \frac{\partial^2 u}{\partial y^2} \right) \right] d\Omega_i = \int_{\Omega_i} \rho g_x w d\Omega_i, \quad (6)$$

$$\int_{\Omega_i} \left[ w \frac{\partial p}{\partial y} - \mu w \left( \frac{\partial^2 v}{\partial x^2} + \frac{\partial^2 v}{\partial y^2} \right) \right] d\Omega_i = \int_{\Omega_i} \rho g_y w d\Omega_i, \quad (7)$$

$$\int_{\Omega_i} \left[ Q \left( \frac{\partial u}{\partial x} + \frac{\partial v}{\partial y} \right) \right] d\Omega_i = 0. \quad (8)$$

Applying Green's identity to the left-hand side of Eq. (6) and (7), we have

$$\begin{aligned} \int_{\Omega_i} \left[ \mu \left( \frac{\partial w}{\partial x} \frac{\partial u}{\partial x} + \frac{\partial w}{\partial y} \frac{\partial u}{\partial y} \right) - \frac{\partial w}{\partial x} p \right] d\Omega_i &= \int_{\Omega_i} \rho g_x w d\Omega_i \\ &+ \int_{\Gamma_i} \left[ \mu w \left( \frac{\partial u}{\partial x} n_x + \frac{\partial u}{\partial y} n_y \right) - w p n_x \right] d\Gamma_i, \end{aligned} \quad (9)$$

$$\begin{aligned} \int_{\Omega_i} \left[ \mu \left( \frac{\partial w}{\partial x} \frac{\partial v}{\partial x} + \frac{\partial w}{\partial y} \frac{\partial v}{\partial y} \right) - \frac{\partial w}{\partial y} p \right] d\Omega_i &= \int_{\Omega_i} \rho g_y w d\Omega_i \\ &+ \int_{\Gamma_i} \left[ \mu w \left( \frac{\partial v}{\partial x} n_x + \frac{\partial v}{\partial y} n_y \right) - w p n_y \right] d\Gamma_i, \end{aligned} \quad (10)$$

where  $n_x$  and  $n_y$  are outward unit normal vectors in  $x$ - and  $y$ -directions, respectively. Let  $V_h$  and  $P_h$  be finite-dimensional subspaces of  $H^1(\Omega)$  and  $L_0^2(\Omega)$ , respectively, where  $L_0^2(\Omega) = \{p \in$

$L^2(\Omega) : \int_{\Omega} p \, d\Omega = 0$ }. Let  $(u, v, p) \in V_h \times V_h \times P_h$  and the variables  $u, v$  and  $p$  be expressed as

$$u(\mathbf{x}) = \sum_{n=1}^N \psi_n(\mathbf{x}) u^n = \psi^T \mathbf{U}, \quad (11)$$

$$v(\mathbf{x}) = \sum_{n=1}^N \psi_n(\mathbf{x}) v^n = \psi^T \mathbf{V}, \quad (12)$$

$$p(\mathbf{x}) = \sum_{l=1}^L \phi_l(\mathbf{x}) p_l = \phi^T \mathbf{P}, \quad (13)$$

where  $\mathbf{U}$  and  $\mathbf{V}$  are the vectors of the velocities,  $\mathbf{P}$  is a vector of the pressure, the superscript  $T$  represents the transpose operation. The vectors  $\psi$  and  $\phi$  are quadratic and linear shape functions, respectively. Let the weight functions  $w$  and  $Q$  be approximated as

$$w \approx \psi_n, \quad Q \approx \phi_l. \quad (14)$$

Substituting Eqs. (11) - (14) into Eqs. (8) - (10), we have

$$\begin{aligned} & \mu \int_{\Omega_i} \left( \frac{\partial \psi}{\partial x} \frac{\partial \psi^T}{\partial x} + \frac{\partial \psi}{\partial y} \frac{\partial \psi^T}{\partial y} \right) d\Omega_i \mathbf{U} - \int_{\Omega_i} \frac{\partial \psi}{\partial x} \phi^T d\Omega_i \mathbf{P} = \int_{\Omega_i} \rho g_x \psi \, d\Omega_i \\ & + \mu \int_{\Gamma_i} \left( \psi \frac{\partial \psi^T}{\partial x} n_x + \psi \frac{\partial \psi^T}{\partial y} n_y \right) d\Gamma_i \mathbf{U} - \int_{\Gamma_i} \psi \phi^T n_x \, d\Gamma_i \mathbf{P}, \end{aligned} \quad (15)$$

$$\begin{aligned} & \mu \int_{\Omega_i} \left( \frac{\partial \psi}{\partial x} \frac{\partial \psi^T}{\partial x} + \frac{\partial \psi}{\partial y} \frac{\partial \psi^T}{\partial y} \right) d\Omega_i \mathbf{V} - \int_{\Omega_i} \frac{\partial \psi}{\partial y} \phi^T d\Omega_i \mathbf{P} = \int_{\Omega_i} \rho g_y \psi \, d\Omega_i \\ & + \mu \int_{\Gamma_i} \left( \psi \frac{\partial \psi^T}{\partial x} n_x + \psi \frac{\partial \psi^T}{\partial y} n_y \right) d\Gamma_i \mathbf{V} - \int_{\Gamma_i} \psi \phi^T n_y \, d\Gamma_i \mathbf{P}, \end{aligned} \quad (16)$$

$$\int_{\Omega_i} \phi \frac{\partial \psi^T}{\partial x} d\Omega_i \mathbf{U} + \int_{\Omega_i} \phi \frac{\partial \psi^T}{\partial y} d\Omega_i \mathbf{V} = \mathbf{0}. \quad (17)$$

Let  $\Omega_i = \bigcup_e \Omega_i^e$ ,  $i = 1, 2$ , where  $\Omega_i^e$  is the element domain. Then Eqs. (15) - (17) can be written in the element matrix form as follows

$$\begin{bmatrix} K & \mathbf{0} & -A_1 \\ \mathbf{0} & K & -A_2 \\ A_1^T & A_2^T & \mathbf{0} \end{bmatrix} \begin{Bmatrix} \mathbf{U} \\ \mathbf{V} \\ \mathbf{P} \end{Bmatrix} = \begin{Bmatrix} F_1 \\ F_2 \\ \mathbf{0} \end{Bmatrix}, \quad (18)$$

where the elements in the coefficient matrix are defined as

$$\begin{aligned} K &= \mu \int_{\Omega_i^e} \left( \frac{\partial \psi}{\partial x} \frac{\partial \psi^T}{\partial x} + \frac{\partial \psi}{\partial y} \frac{\partial \psi^T}{\partial y} \right) d\Omega_i^e, \\ A_1 &= \int_{\Omega_i^e} \frac{\partial \psi}{\partial x} \phi^T d\Omega_i^e, \\ A_2 &= \int_{\Omega_i^e} \frac{\partial \psi}{\partial y} \phi^T d\Omega_i^e, \\ F_1 &= \int_{\Omega_i^e} \rho g_x \psi \, d\Omega_i^e + \mu \int_{\Gamma_i^e} \left( \psi \frac{\partial \psi^T}{\partial x} n_x + \psi \frac{\partial \psi^T}{\partial y} n_y \right) d\Gamma_i^e \mathbf{U} - \int_{\Gamma_i^e} \psi \phi^T n_x \, d\Gamma_i^e \mathbf{P}, \\ F_2 &= \int_{\Omega_i^e} \rho g_y \psi \, d\Omega_i^e + \mu \int_{\Gamma_i^e} \left( \psi \frac{\partial \psi^T}{\partial x} n_x + \psi \frac{\partial \psi^T}{\partial y} n_y \right) d\Gamma_i^e \mathbf{V} - \int_{\Gamma_i^e} \psi \phi^T n_y \, d\Gamma_i^e \mathbf{P}, \quad i = 1, 2. \end{aligned} \quad (19)$$

We now obtain the element matrix form for the domains  $\Omega_1$  and  $\Omega_2$ . The boundary conditions used in this problem are provided in the next section.

## 4 Boundary Conditions

The boundary conditions used in this research are presented in this section. Figure 3 shows the domains and boundaries used in this study. The variable  $y_{ML}$  is the  $y$  value at the top of domain  $\Omega_2$ . Although  $y_{PCL}$  is the length of cilia when cilia are perpendicular to the horizontal plane, in this study, we use dimensionless  $y_{PCL}$  which is equal to 1. Similarly, we use dimensionless  $y_{ML}$ . So  $y_{ML}$  is equal to 2. Here, we suppose that cilia bend downward from  $\theta = 90^\circ$  to other angles, decreasing by  $10^\circ$  for every 0.2 change in the  $x$ -axis. That is, when cilia make the angles  $\theta = 90^\circ, 80^\circ, 70^\circ, 60^\circ$  and  $50^\circ$ , they correspond to the ranges of  $x = 0$  to  $x = 0.2$ ,  $x = 0.2$  to  $x = 0.4$ ,  $x = 0.4$  to  $x = 0.6$ ,  $x = 0.6$  to  $x = 0.8$ , and  $x = 0.8$  to  $x = 1$ , respectively. We assume cilia stop beating at the angle  $\theta = 40^\circ$  (Sears et al., 2013). The boundary  $\Gamma_1$  is at the tips of the cilia excluding the case that  $\theta = 90^\circ$ . The boundary  $\Gamma_2$  is at the interface between the free-fluid region,  $\Omega_1$ , and the ML,  $\Omega_2$ . The boundary  $\Gamma_3$  is the right boundary of  $\Omega_1$ . The boundaries  $\Gamma_4$ ,  $\Gamma_5$  and  $\Gamma_6$  are at the left, right and the top borders of  $\Omega_2$ , respectively. In this work, we assume that the velocity is continuous at the free-fluid region/the ML interface (at  $\Gamma_2$ ).

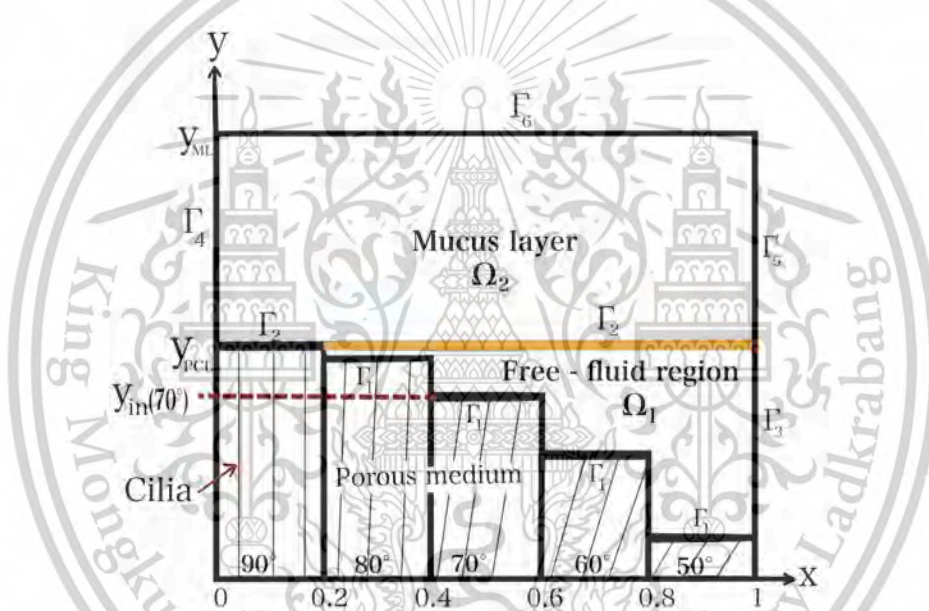


Figure 3: Domains and boundaries.

We first consider the free-fluid region,  $\Omega_1$ . The velocity of the PCL fluid at  $\Gamma_1$  is obtained from Wuttanachamsri et al. (2024). That is

$$\begin{aligned} u(x, y_{in}) &= u_{in} \text{ at } \Gamma_1, \\ v(x, y_{in}) &= v_{in} \text{ at } \Gamma_1, \end{aligned} \quad (20)$$

where  $u_{in}$  and  $v_{in}$  are the velocities of the PCL fluid in  $x$ - and  $y$ -directions at the boundary  $\Gamma_1$ .

For the ML,  $\Omega_2$ , we use the velocity of the PCL fluid obtained from  $\Omega_1$  to be the boundary condition at the bottom of  $\Omega_2$ . The velocity of the PCL fluid at  $y = y_{in}(90^\circ)$  is obtained from Wuttanachamsri et al. (2024). At the boundary  $\Gamma_6$ , we assume that

$$\begin{aligned} \frac{\partial u(x, y_{ML})}{\partial y} &= 0 \text{ at } \Gamma_6, \\ \frac{\partial v(x, y_{ML})}{\partial y} &= 0 \text{ at } \Gamma_6. \end{aligned} \quad (21)$$

The velocities at the boundaries  $\Gamma_3, \Gamma_4$  and  $\Gamma_5$  are unknown. The boundary conditions will be applied to Eq. (18) to find the velocities of the fluids in  $\Omega_1$  and  $\Omega_2$  in the next section.

## 5 Numerical Results

In this section, we present the numerical results of the two-dimensional Stokes equation by using a mixed finite element method. To find the velocities of the fluids in  $\Omega_1$  and  $\Omega_2$ , we first provide the velocity of the PCL fluid at the tips of cilia, obtained from Wuttanachamsri et al. (2024), when cilia make the angle  $\theta = 90^\circ$  to  $50^\circ$  to the horizontal plane. In Wuttanachamsri et al. (2024), the authors have found the velocity of the PCL fluid in the porous domain for the forward stroke of cilia. Figure 4 illustrates the velocity  $u$  of the PCL fluid at the tips of cilia at  $\theta = 90^\circ, 80^\circ, 70^\circ, 60^\circ$  and  $50^\circ$ . Note that the velocities decrease when  $\theta$  decreases. Figure 5 shows the velocity  $v$  of the PCL fluid at the tips of cilia. Remark that the velocity  $v$  is greater than zero at  $\theta = 90^\circ$  and drops to the negative values at other angles. This is because the cilia bend down during their forward stroke. The velocity of the PCL fluid at the tips of the cilia is used to be the bottom boundary condition of  $\Omega_1$  (at  $\Gamma_1$ ) except the velocity at  $\theta = 90^\circ$ . This is due to the absence of a free-fluid region in  $\Omega_1$  when the cilia are perpendicular to the horizontal plane. The outward unit normal vector  $\mathbf{n} = (n_x, n_y)$  used in this work is  $(0, -1)$  at  $\Gamma_1$ ,  $(1, 0)$  at  $\Gamma_3$  and  $\Gamma_5$ ,  $(-1, 0)$  at  $\Gamma_4$  and  $(0, 1)$  at  $\Gamma_6$ . At  $\Gamma_2$ , we assume that the velocity is continuous at the free-fluid region / the ML interface.

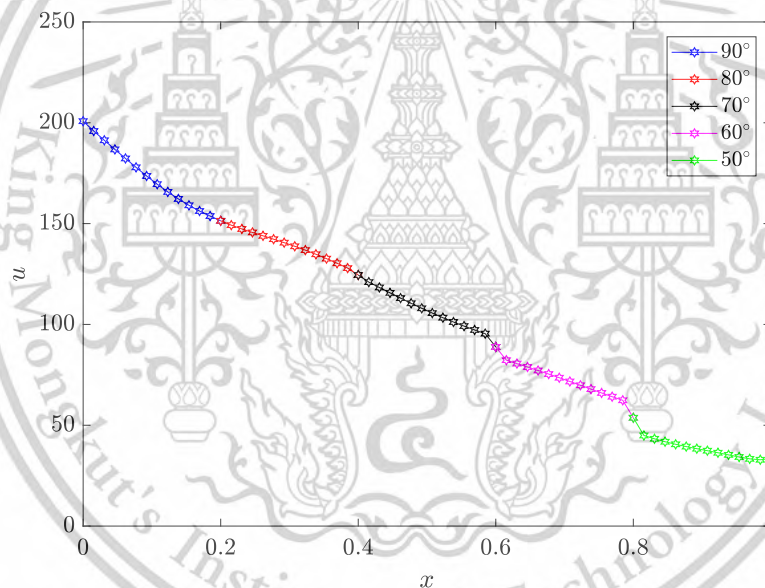


**Figure 4:** The velocity  $u$  of the PCL fluid at the tips of the cilia for each angle

The values of other variables used to calculate the numerical result in the domains  $\Omega_1$  and  $\Omega_2$  are as follows. The gravity  $\mathbf{g} = (0, 9.8 \times 10^{-6})(\mu\text{m}/\text{s}^2)$  and the fluid density  $\rho = 992.2 \times 10^{-15}(g/\mu\text{m}^3)$ , which is the density of the water at  $40^\circ\text{C}$  (The Engineering ToolBox, 2013). Since the viscosity of the PCL fluid and the mucus are different, the viscosities used in this paper are  $\mu = 3 \times 10^{-6}(g/(\mu\text{m} \cdot \text{s}))$  in  $\Omega_1$  (Wuttanachamsri & Schreyer, 2020) and  $\mu = 2 \times 10^{-5}(g/(\mu\text{m} \cdot \text{s}))$  in  $\Omega_2$  (Chatelin & Poncet, 2016).

The numerical solutions are verified by comparing them with an exact solution (Koplik et al., 1983). The domain of the problem consists of the porous medium below a free-fluid layer and an impermeable plate dragged in the  $x$ -direction at the top of the domain. In this work, we only compare our numerical solution with the velocity of free fluid above the porous medium. Since our numerical solution is calculated in the two-dimensional domain, we average the numerical solution over the  $x$ -direction and compare the average result with the exact solution. Figure 6 illustrates the average velocities calculated from different mesh refinements which are 5, 11 and 17 nodes in  $y$ -direction, and the exact solution. It presents that the average velocities converge

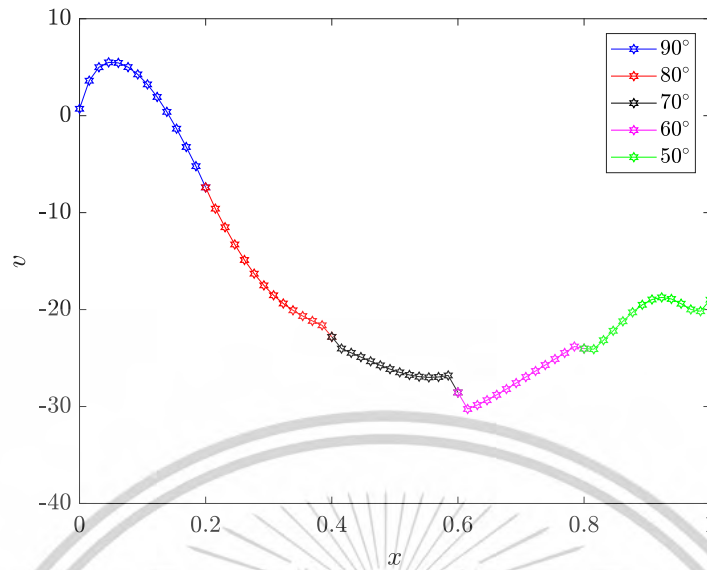


**Figure 5:** The velocity  $v$  of the PCL fluid at the tips of the cilia for each angle

to the exact solution when the number of nodes in  $y$ -direction increases. The  $l_2$ -norm errors of the average velocities are shown in Table 1. It shows that the error decreases as the number of nodes in  $y$ -direction increases.

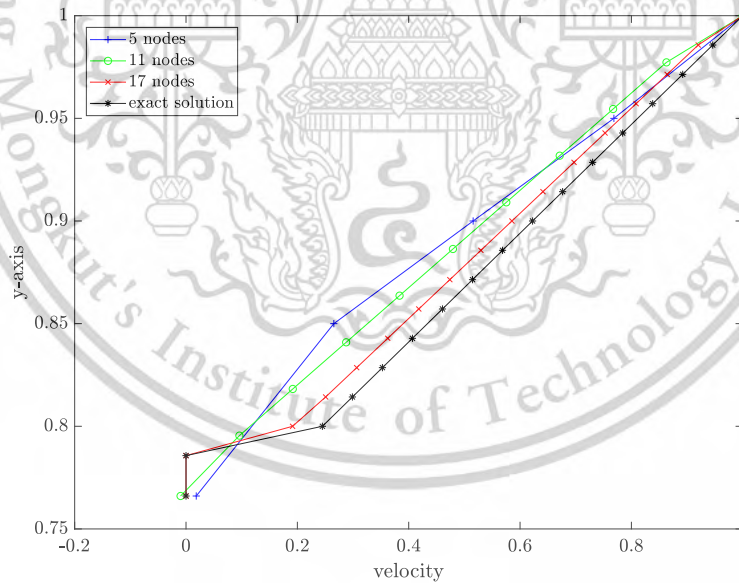


**Figure 6:** The average velocities for 5, 11 and 17 nodes in  $y$ -direction and the exact solution

#nodes in $y$ -direction	$l_2$ -norm errors
5 nodes	0.3047
11 nodes	0.2856
17 nodes	0.1461

**Table 1:** The  $l_2$ -norm errors of the nodes in  $y$ -direction

This material is reserved for educational use only, not allowed for commercial use.

Next, we find the velocities of fluids in  $\Omega_1$  and  $\Omega_2$  by applying a mixed finite element method

Forbidden to modify the content, and cite the document when use.

to the two-dimensional Stokes equation with the boundary conditions mentioned in the previous section. The number of grid points used in this work is 3051 grid points which is generated by the open software Netgen (Schöberl, 1997). The velocity of the fluid in  $\Omega_1$  is provided in Figures 7 and 8 at the angle  $\theta = 80^\circ - 50^\circ$ . So, the velocity of the fluid in  $\Omega_1$  starts at  $\theta = 80^\circ$  from  $x = 0.2$  to  $0.4$ . For the  $x$  ranges of the angle  $\theta = 70^\circ, 60^\circ$  and  $50^\circ$  are  $x = 0.4$  to  $0.6$ ,  $x = 0.6$  to  $0.8$  and  $x = 0.8$  to  $1$ , respectively. The heights of domain  $\Omega_1$  from  $y_{in}(\theta)$  to  $y_{PCL}$  for the angle  $\theta = 80^\circ, 70^\circ, 60^\circ$  and  $50^\circ$  are  $0.0152, 0.0603, 0.1339$  and  $0.2339$ , respectively. Figure 7 shows the velocity  $u$  of the fluid in  $\Omega_1$  which is highest at  $\theta = 80^\circ$  and it decreases when the angle decreases. Figure 8 demonstrates that the velocity  $v$  of the fluid in  $\Omega_1$  is the negative value when cilia are bending in a downward direction, which the least negative value occurs at  $\theta = 60^\circ$ . Then the velocity has less negative until  $\theta = 50^\circ$ .

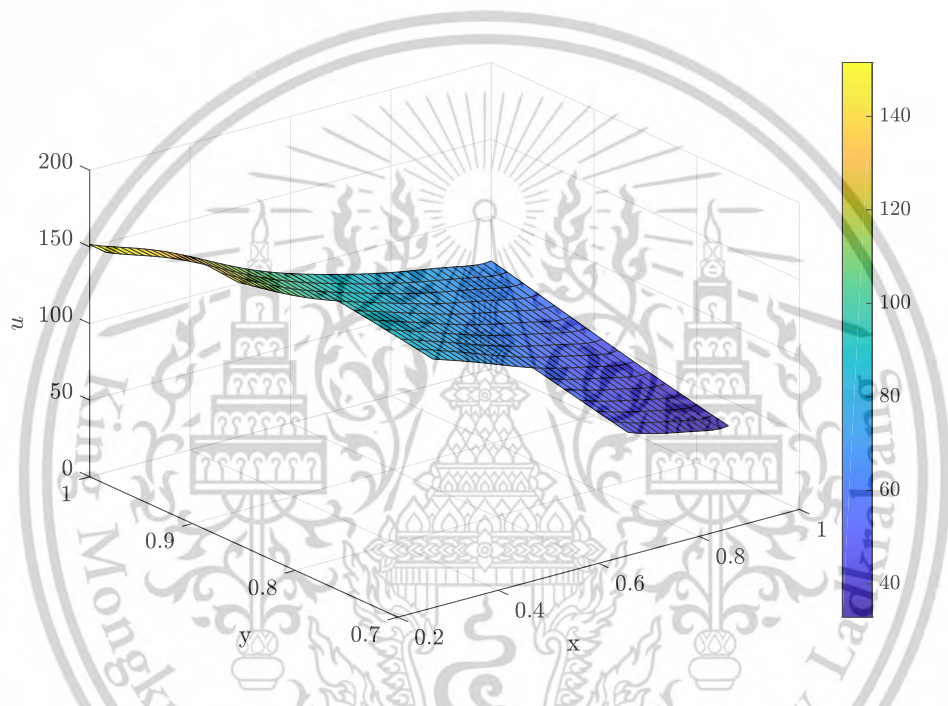


**Figure 7:** The velocity  $u$  of the fluid in  $\Omega_1$

To find the velocity of mucus in  $\Omega_2$ , we use the velocity at the top of the domain  $\Omega_1$  to be the velocity at the bottom of the domain  $\Omega_2$ . The domain  $\Omega_2$  is  $[0, 1] \times [1, 2]$ . Figure 9 shows that the mucus velocity  $u$  is maximum at  $(x, y) = (0, 1)$  and minimum at  $(x, y) = (0.98, 1)$  which is at the bottom boundary of  $\Omega_2$ . Although, from the left to the right, the velocity  $u$  of mucus declines when  $y \in [1, 1.4]$  for all  $x$ , the velocity  $u$  of mucus is almost the same when  $y \in [1.4, 2]$  for all  $x$ . Therefore most of the mucus moves at a constant velocity in the  $x$ -direction. Figure 10 illustrates the velocity  $v$  of mucus. Since the velocity  $v$  of the mucus is affected by the bottom boundary condition of the velocity  $v$  of the fluid in  $\Omega_1$ , the velocity  $v$  is negative and then the velocity  $v$  of mucus is significantly more negative when  $x \in [0.14, 1]$  for  $y \leq 1.4$ . The velocity  $v$  of mucus fluctuates like a wave but the value does not vary much when  $y \geq 1.4$  for all  $x$ .

The horizontal velocity of the fluid in  $\Omega_1$  (Figure 7) and the mucus velocity (Figure 9) are averaged over the  $x$ -axis and plotted together in Figure 11. Figure 11 shows the average velocity  $u$  of the fluid in  $\Omega_1$  and mucus, where the blue diamond and red square refer to the average velocity  $u$  of mucus and the fluid in  $\Omega_1$ , respectively. The average velocity  $u$  begins to fluctuate since  $y \geq y_{PCL}$  and alternates like a vertical wave. The mean value of the average velocity  $u$  is approximately  $119 \mu\text{m/s}$ . Similarly, the average vertical velocity is illustrated in Figure 12. It shows that the average velocity  $v$  is negative and it has less negative when  $y$  increases. The velocities  $u$  and  $v$  in Figures 11 and 12 are employed to find the speeds of the PCL fluid

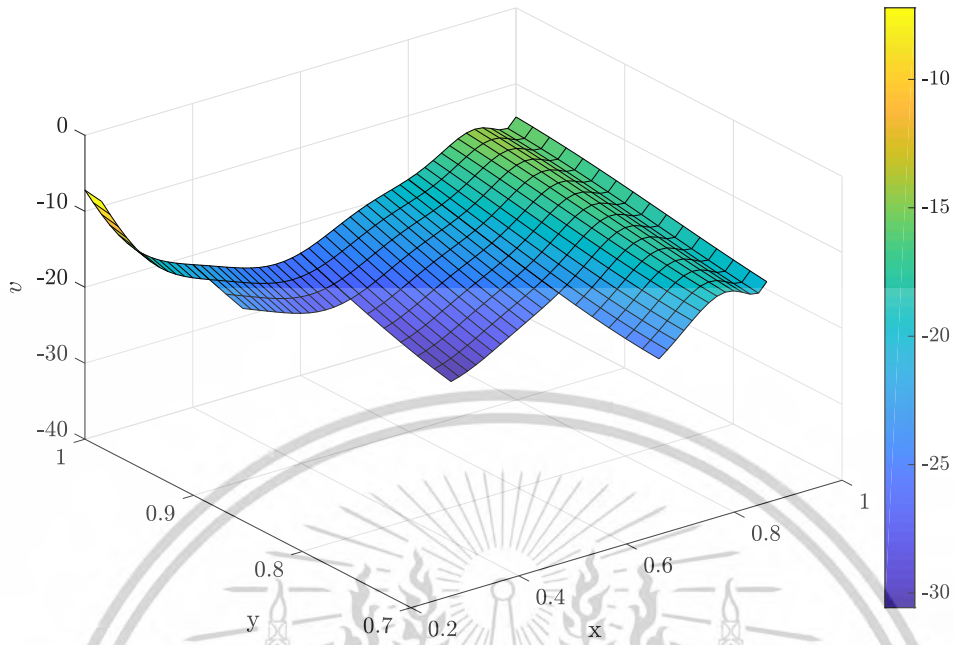


**Figure 8:** The velocity  $v$  of the fluid in  $\Omega_1$

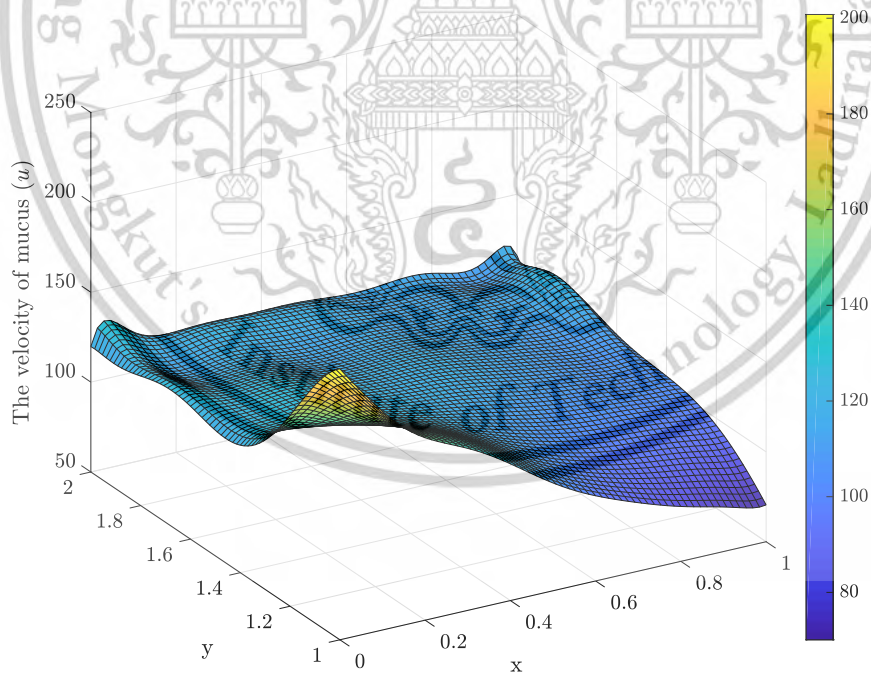


**Figure 9:** The velocity  $u$  of mucus

in  $\Omega_1$  and mucus, which are shown in Figure 13. The red asterisk and the blue circle are the speeds of the fluid in  $\Omega_1$  and mucus, respectively. The average speed of mucus is about  $118 \mu\text{m}/\text{s}$  (or about  $7.1 \text{ mm}/\text{min}$ ). The curve of the speeds is similar to the average horizontal velocity. It shows the movement of the fluid is possessed by the velocity in  $x$ -direction. Next,

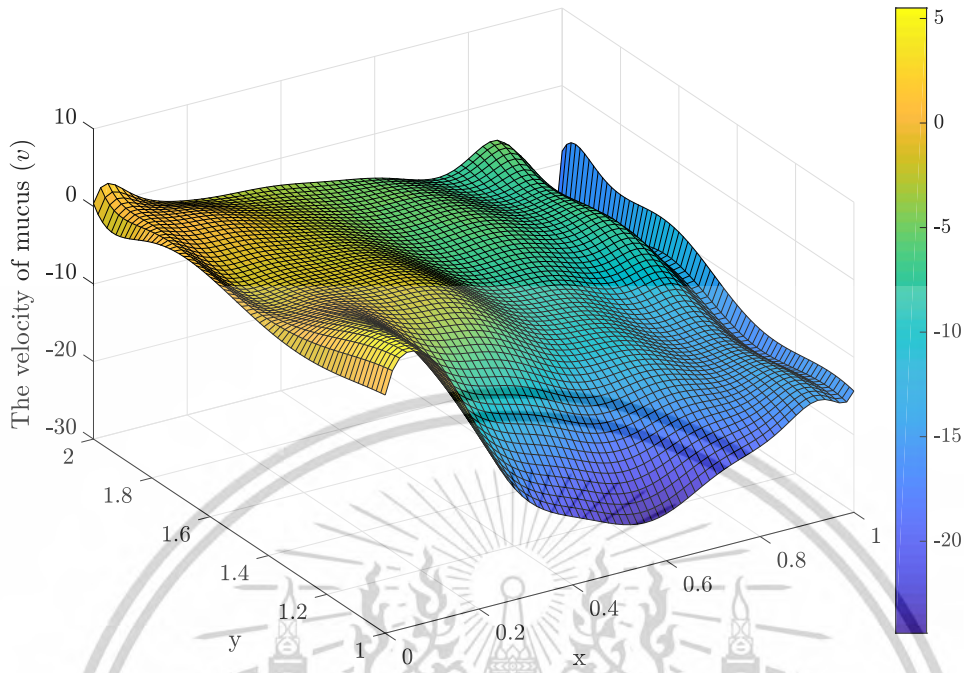


**Figure 10:** The velocity  $v$  of mucus

we compare the average speed of mucus with experimental data in Yeates et al. (1975) in which the mucociliary transport rate has been studied in 42 nonsmoker healthy adults between the ages of 20 to 43 years. The range of the transport rate is  $0.8 - 12.4 \text{ mm/min}$  while our result is about  $7.1 \text{ mm/min}$ . The result is close to the transport rate of men between the ages of 22 – 32 years and women between the ages of 22 – 30 years.

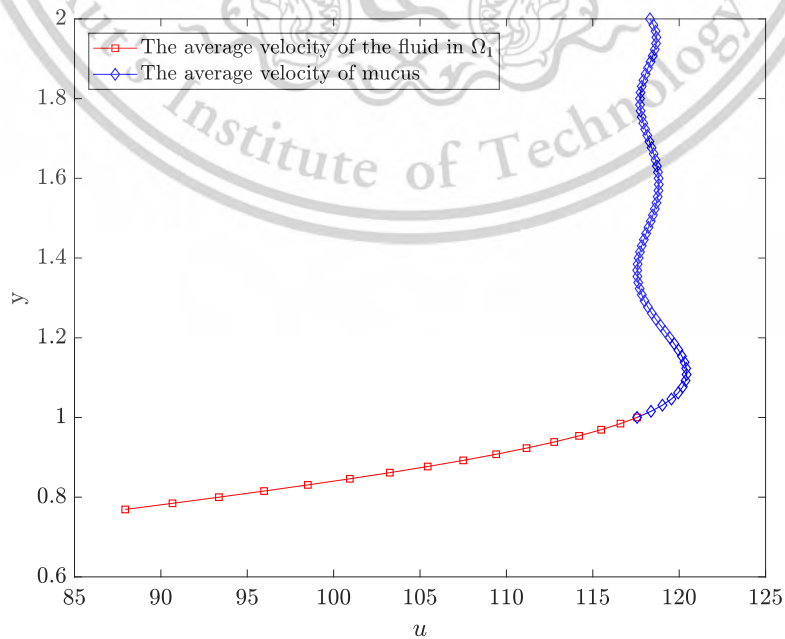


**Figure 11:** The average velocity  $u$  over the  $x$ -direction of the fluid in  $\Omega_1$  and mucus.

Forbidden to modify the content, and cite the document when use.

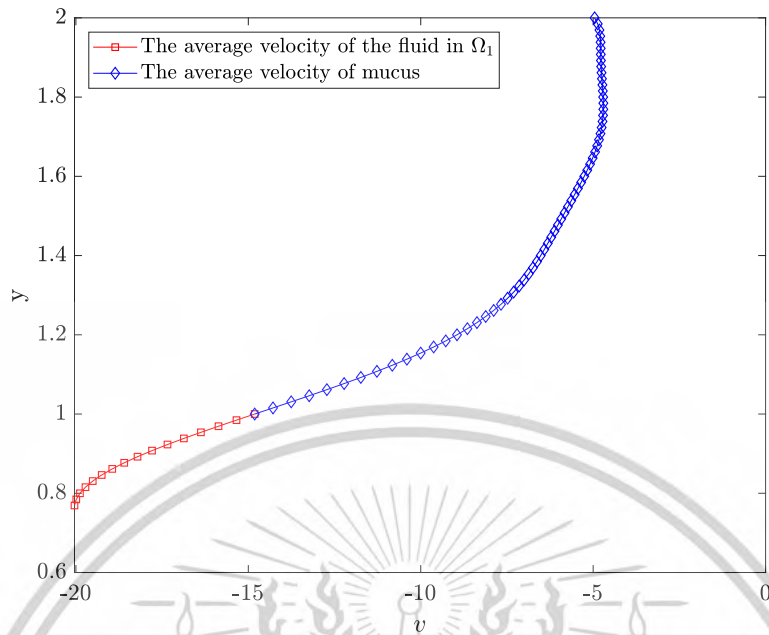


**Figure 12:** The average velocity  $v$  over the  $x$ -direction of the fluid in  $\Omega_1$  and mucus

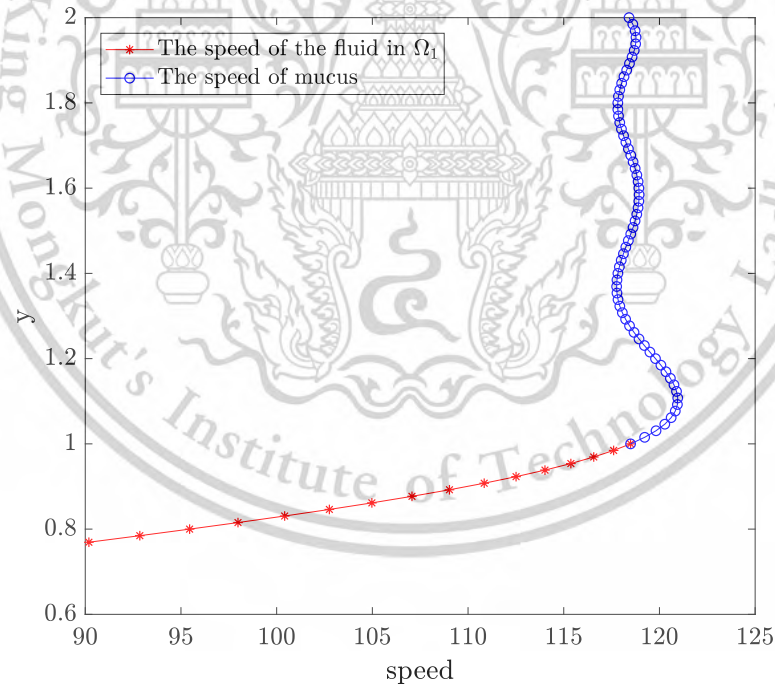


**Figure 13:** The speeds of the fluid in  $\Omega_1$  and mucus

We approximate the speeds of the fluid in  $\Omega_1$  and mucus by a polynomial approximation degree 9. The coefficients of the ninth-order polynomial approximation of the speed are shown in Table 2, where  $h$  is from  $y_{in}(50^\circ)$  to  $y_{ML}$ . That is  $h = 0.7660$  to  $h = 2$ . Figure 14 displays the polynomial approximation with the fluid speed in  $\Omega_1$  and  $\Omega_2$ , where the green square, the red asterisk and the blue circle refer to the polynomial approximation, the speed of the fluid in  $\Omega_1$  and the speed of mucus, respectively. It shows that the polynomial approximation estimates the speeds of the fluid in  $\Omega_1$  and mucus well with the  $l_2$ -norm error 0.0282.

**Table 2:** The ninth-order polynomial functions:  $p(h) = c_1h^9 + c_2h^8 + c_3h^7 + c_4h^6 + c_5h^5 + c_6h^4 + c_7h^3 + c_8h^2 + c_9h + c_{10}$  for the speeds of the fluid in  $\Omega_1$  and mucus.

Coefficient	$10^6 \times$
$c_1$	0.002271511545374
$c_2$	-0.029497677298672
$c_3$	0.166716780614724
$c_4$	-0.537680842522555
$c_5$	1.089315989130731
$c_6$	-1.436339487060982
$c_7$	1.232011089245644
$c_8$	-0.663157249265035
$c_9$	0.203717832820274
$c_{10}$	-0.027239428286010

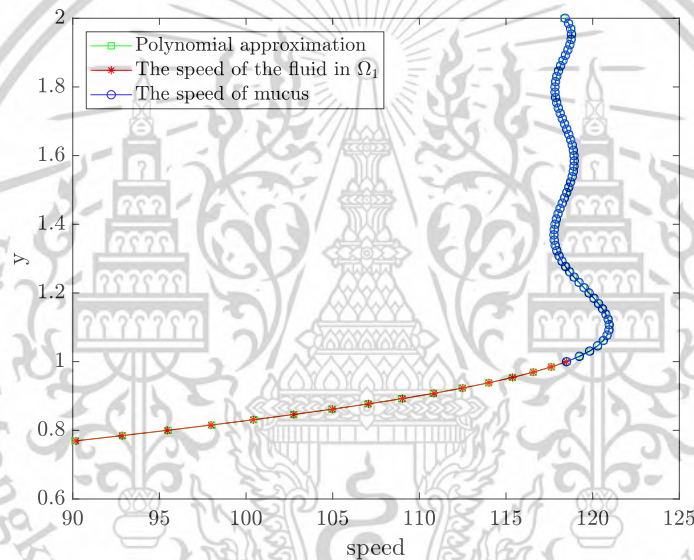


**Figure 14:** The polynomial approximation and the speeds of the fluid in  $\Omega_1$  and mucus

## 6 Conclusion

In this study, we find the velocity of the fluid in the free-fluid region,  $\Omega_1$ , and then calculate the mucus velocity in  $\Omega_2$ . The fluid flows in both domains are affected by cilia movement. We employ the two-dimensional Stokes equation and then apply the mixed finite element method to the equation to calculate the velocities of the fluids in  $\Omega_1$  and  $\Omega_2$ . We first verify the numerical result by averaging our two-dimensional numerical solution over  $x$ -axis and compare it with the exact solution in the one-dimensional domain in the case of static solid phases. The numerical result converges to the exact solution with the small  $l_2$ -norm error.

For the two-dimensional solution, we present the velocity of the PCL fluid in  $\Omega_1$  for the angle  $\theta = 80^\circ - 50^\circ$  and the mucus velocity. We provide the velocities  $u$  and  $v$  of the fluid in  $\Omega_1$  and then we use them to find the velocity of mucus. The velocities  $u$  and  $v$  of the fluid in  $\Omega_1$  and mucus are averaged over  $x$ -axis and plotted together in one graph. Next, we find the speed of the average velocities of the fluid in both domains. The shape of the speed is similar to the average velocity  $u$ . This indicates that the velocity  $u$  has more impact on fluid motion than the velocity  $v$ . The speed of the mucus is averaged and compared with the experimental data. Our mucus velocity is about  $118 \mu\text{m/s}$  (or about  $7.1 \text{ mm/min}$ ). This result is close to

the experimental data of 22- to 32-year-old men and 22- to 30-year-old women (Yeates et al., 1975). The speeds of the fluid in  $\Omega_1$  and mucus are approximated by a ninth-order polynomial approximation, provided in Table 2. This work can be effectively applied to problems involving fluid dynamics influenced by the self-movement of solid phases.

### Acknowledgement

This paper is supported by the School of Science, King Mongkut's Institute of Technology Ladkrabang, Bangkok, Thailand.

### References

- Battle, C., Ott, C.M., Burnette, D.T., Lippincott-Schwartz, J. & Schmidt, C.F. (2015). Intracellular and extracellular forces drive primary cilia movement. *Proceedings of the National Academy of Sciences*, 112(5), 1410–1415.
- Boucher, R.C. (1999). Molecular insights into the physiology of the ‘thin film’ of airway surface liquid. *The Journal of Physiology*, 516(3), 631–638.
- Chamsri, K. (2014). N-dimensional Stokes-Brinkman equations using a mixed finite element method. *Australian Journal of Basic and Applied Sciences*, 8, 30–36.
- Chatelin, R., Poncet, P. (2016). A parametric study of mucociliary transport by numerical simulations of 3D non-homogeneous mucus. *Journal of biomechanics*, 49(9), 1772–1780.
- Derichs, N., Jin, B., Song, Y., Finkbeiner, W.E. & Verkman, A.S. (2011). Hyperviscous airway periciliary and mucous liquid layers in cystic fibrosis measured by confocal fluorescence photobleaching. *The FASEB Journal*, 25(7), 2325.
- Ding, Y., Nawroth, J.C., McFall-Ngai, M.J. & Kanso, E. (2014). Mixing and transport by ciliary carpets: A numerical study. *Journal of Fluid Mechanics*, 743, 124–140.
- Houtmeyers, E., Gosselink, R., Gayan-Ramirez, G. & Decramer, M. (1999). Regulation of mucociliary clearance in health and disease. *European Respiratory Journal*, 13(5), 1177–1188.
- Kasamwan, T., Wuttanachamsri, K. (2020). Unsteady one-dimensional flow in PCL with Stokes-Brinkman equations. *Phayao Research Conference*, 1949–1964.
- Knowles, M.R., Boucher, R.C. (2002). Mucus clearance as a primary innate defense mechanism for mammalian airways. *The Journal of clinical investigation*, 109(5), 571–577.
- Koplik, J., Levine, H. & Zee, A. (1983). Viscosity renormalization in the Brinkman equation. *Physics of Fluids*, 26, 1958–1988.
- Lale, A.M., Mason, J.D.T., & Jones, N.S. (1998). Mucociliary transport and its assessment: A review. *Clinical Otolaryngology & Allied Sciences*, 23(5), 388–396.
- Matthews, L.W., Spector, S., Lemm, J. & Potter, J.L. (1963). Studies on pulmonary secretions: I. The over-all chemical composition of pulmonary secretions from patients with cystic fibrosis, bronchiectasis, and laryngectomy. *American Review of Respiratory Disease*, 88(2), 199–204.
- Modaresi, M.A. & Shirani, E. (2023). Mucociliary clearance affected by mucus-periciliary interface stimulations using analytical solution during cough and sneeze. *The European Physical Journal Plus*, 138(3), 1–18.
- Phaenchat, S., Wuttanachamsri, K. (2019). On the nonlinear Stokes-Brinkman equations for modeling flow in PCL. *The 24th Annual Meeting in Mathematics*, 167–175.

- Poopra, S., Wuttanachamsri, K. (2019). The velocity of PCL fluid in human lungs with Beaver and Joseph boundary condition by using asymptotic expansion method. *Mathematics*, 7(6), 567.
- Poopra, S., Wuttanachamsri, K. (2022). On the asymptotic boundary condition at the free-fluid/porous-medium interface in periciliary layer due to the ciliary movement. *Mathematical Problems in Engineering*, 2022.
- Potter, J.L., Matthews, L.W., Spector, S. & Lemm, J. (1967). Studies on pulmonary secretions: II. Osmolality and the ionic environment of pulmonary secretions from patients with cystic fibrosis, bronchiectasis, and laryngectomy. *American Review of Respiratory Disease*, 96(1), 83-87.
- Rusznak, C., Devalia, J.L., Lozewicz, S. & Davies, R.J. (1994). The assessment of nasal mucociliary clearance and the effect of drugs. *Respiratory medicine*, 88(2), 89-101.
- Satir, P., Christensen, S.T. (2007). Overview of structure and function of mammalian cilia. *Annu. Rev. Physiol.*, 69, 377-400.
- Schöberl, J. (1997). NETGEN An advancing front 2D/3D-mesh generator based on abstract rules. *Computing and visualization in science*, 1(1), 41-52.
- Sears, P.R., Thompson, K., Knowles, M.R. & Davis, C.W. (2013). Human airway ciliary dynamics. *American Journal of Physiology-Lung Cellular and Molecular Physiology*, 304(3), L170-L183.
- Sedaghat, M.H., Sadrizadeh, S. & Abouali, O. (2023). Three-dimensional simulation of mucociliary clearance under the ciliary abnormalities. *Journal of Non-Newtonian Fluid Mechanics*, 316, 105029.
- Suankasem, S., Pimkote, A., Thammathon, I. & Wuttanachamsri, K. (2018). Matched asymptotic expansion for PCL fluid due to the movement of lung cilia: part 1. *10th National Science Research Conference*.
- The Engineering ToolBox (2003). Water-Density, Specific Weight and Thermal Expansion Coefficients. Retrieved from [https://www.engineeringtoolbox.com/water-density-specific-weight-d\\_595.html](https://www.engineeringtoolbox.com/water-density-specific-weight-d_595.html).
- Vanaki, S.M., Holmes, D., Saha, S.C., Chen, J., Brown, R.J. & Jayathilake, P.G. (2020). Mucociliary clearance: A review of modeling techniques. *Journal of Biomechanics*, 99, 109578.
- Verma, V.S. & Rana, V. (2015). Mucus transport in the human lung airways: Effect of porosity parameter and air velocity. *IJSR*, 920-925.
- Wanner, A., Salathé, M. & O’Riordan, T.G. (1996). Mucociliary clearance in the airways. *American journal of respiratory and critical care medicine*, 154(6), 1868-1902.
- Wuttanachamsri, K. (2020). Free interfaces at the tips of the cilia in the one-dimensional periciliary layer. *Mathematics*, 8(11), 1961.
- Wuttanachamsri, K., Oangwacharaparkan, N. & Phaenchat, S. (2024). Wave of Cilia Affecting the Velocity of Fluid in Periciliary Layer. Numerical Algorithms, submitted.
- Wuttanachamsri, K. & Schreyer, E. (2020). Effects of cilia movement on fluid velocity: II numerical solutions over a fixed domain. *Transport in Porous Media*, 134(2), 471-489.

- Xu, L., Jiang, Y. (2015). Cilium height difference between Stokes is more effective in driving fluid transport in mucociliary clearance: A numerical study. *Mathematics Biosciences and Engineering*, 12(5), 1107-1126.
- Yeates, D.B., Aspin, N., Levison, H., Jones, M.T. & Bryan, A.C. (1975). Mucociliary tracheal transport rates in man. *Journal of applied physiology*, 39(3), 487-495.



This material is reserved for educational use only, not allowed for commercial use.

Forbidden to modify the content, and cite the document when use.

# Author Biography

Name	Mr.Surachai Phaenchat
Date of Birth	01 July 1995
Address	38/2 Moo 6, Chattrakan Subdistrict, Chattrakan District, Phitsanulok, 65170
Education	2016 Bachelor of Science and Technology in Mathematics GPA 3.61 Rajamangala University of Technology Thanyaburi 2018 Master of Science in Applied Mathematics GPA 3.76 King Mongkut's Institute of Technology Ladkrabang 2024 Doctor of Philosophy in Applied Mathematics GPA 4.00 King Mongkut's Institute of Technology Ladkrabang
Scholarship	2019 School of Science, King Mongkut's Institute of Technology Ladkrabang, Graduate Scholarship
Academic Publication(s)	<ol style="list-style-type: none"><li>1. Surachai Phaenchat and Kanognudge Wuttanachamsri, "On the Nonlinear Stokes-Brinkman Equations for Modeling Flow in PCL.", <i>Proceedings of Annual Meeting in Mathematics 2019 (AMM2019)</i>, May, 15-17, 2019, Burapha University, Chonburi, Thailand.</li><li>2. Surachai Phaenchat and Kanognudge Wuttanachamsri, "Two-dimensional nonlinear Brinkman and steady-state Navier–Stokes equations for fluid flow in PCL.", <i>Partial Differential Equations in Applied Mathematics</i>, 12:100961, 2024.</li><li>3. Surachai Phaenchat and Kanognudge Wuttanachamsri, "Effect of porous medium to fluid flow in mucus layer.", <i>Advanced Mathematical Models &amp; Applications</i>, 10(1):144-159, 2025.</li></ol>